The role of magnetic topology in the edge plasma performance on W7-X

Inaugural-Dissertation

zur Erlangung des Doktorgrades
der Mathematisch-Naturwissenschaftlichen Fakultät
der Heinrich-Heine-Universität Düsseldorf

vorgelegt von

Philipp Drews
aus Bonn

Jülich, Dezember 2018

aus dem Institut für Theoretische Physik
der Heinrich-Heine-Universität Düsseldorf

Gedruckt mit der Genehmigung der
Mathematisch-Naturwissenschaftlichen Fakultät der
Heinrich-Heine-Universität Düsseldorf

Berichterstatter

1. Prof. Dr. Yunfeng Liang
2. Prof. Dr. Georg Pretzler

Tag der mündlichen Prüfung: 30.04.2019

Zusammenfassung

Das Fusions Experiment Wendelstein 7-X ist der größte optimierte Stellarator der Welt. Sein Ziel ist es zu demonstrieren, dass Stellaratoren in optimierter Konfiguration in der Lage sind auch schnelle Teilchen durch ein optimiertes magnetisches Feld einzuschließen. Ein Erfolg dieses Experiments würde möglicherweise einen Wechsel vom Tokamak zum Stellarator für einen möglichen Testreaktor bedeuten. Das Stellarator Konzept verwendet eine geschickte Anordnung der Feldspulen um sowohl ein toroidales als auch ein poloidales Feld zu erzeugen. Somit vermeidet es Probleme die beim Tokamak durch das Treiben eines toroidalen Stromes zur Erzeugung des torodialen Feldes verursacht werden. Dies erlaubt auch einen Dauerbetrieb, da kein Strom getrieben werden muss.

Ein umfassendes Verständnis über das Zusammenspiel der Topologie oder Konfigurationseffekte und der Qualität des magnetischen Einschlusses und Plasma Parameter ist sehr wichtig für die Stellarator Physik. Zur Messung von Randschicht Parametern und speziell Profilen wurde der sogenannte Multi-Purpose-Manipulator installiert. Er erlaubt die flexible Verwendung von Sonden und Materialproben in W7-X. Eine Entwicklung für Messungen der Randschicht sind die zwei Iterationen der kombinierten Sonde. Diese Arbeit beschreibt die Messungen mit Sonden am Stellarator W7-X, sowie ein Vergleich mit ausgewählten Randdiagnostiken und Modellierung.

Die kombinierte Sonde wurde genutzt, um während der schnellen Fahrt des Manipulators die radialen Profile des magnetischen Feldes mit Pick-up Spulen, die Elektronentemperatur und Dichte mit Langmuir Sonden, die Ionentemperatur mit einer ionensensitiven Sonde und die relative Flußgeschwindigkeit mit einer Machsonde zu messen. Messung der Reflektometrie und der Infrarotkameras, welche den Limiter beziehungweise den Divertor beobachten, und EMC3-EIRENE Modellierung werden für einen Vergleich verwendet. Die Messungen wurden sowohl in Limiterplasmen als auch in der Divertorkonfiguration durchgeführt. In den Limiterplasmen wurde erfolgreich die Veränderung des Plasma-Iotas durch eine Modifikation der planaren Spulenströme mit der kombinierten Sonde gemessen.

Die höheren Dichten und Heizleistungen in den Divertorplasmen erlaubten eine Untersuchung des Einflusses des Plasmabetas und der Ströme im Plasma auf die gemessenen Randparameter und auch auf die magnetische Topologie. Die Verwendung von Daten aus der kombinierten Sonde, den Limiter/Divertor Langmuir-Sonden und der abgestrahlten Leistung für die Modellierung mit EMC3-EIRENE erlaubte eine Überprüfung der gemessenen Werte, zusätzlich lieferte das Modell auch ein Profil für die Ionentemperatur. Die Berechnung des Elektronenbeitrags zum Wärmefluss in der Mittelebene des Plasmas im Vergleich zum Gesamtwärmefluss auf dem Limiter/Divertor machte eine experimentelle Abschätzung der Ionentemperatur zusätzlich möglich. Unter Verwendung der Ionentemperatur aus der Modellierung war es außerdem möglich, den Effekt der Iotaänderung auf die in der Standardkonfiguration bestehende Wärmelastassymmetrie zu belegen.

Ein großer Teil dieser Arbeit befasste sich mit Messungen am Plasmarand. Während die Modellierung eine gewisse Aussage über die Position der letzten geschlossenen Flussfläche machen konnte, gab es dennoch ausreichend Fälle, zum Beispiel beim Einsatz der Korrekturspulen oder später bei einer Erhöhung des Plasmas-Betas, bei denen Änderungen des Plasmas nur sehr schlecht vorhergesagt werden konnten. Mit einer Abfalllänge von etwa einem Zentimeter musste immer ein Kompromiss zwischen den besten Resultaten bei der Messung and der Gefahr, den Sondenkopf zu verbrennen, gefunden werden.

Abstract

The fusion experiment Wendelstein 7-X (W7-X) is the largest optimized stellarator of the world. The aim of the experiment is to demonstrate the capability of stellarators, with an optimized configuration, to confine fast particles due to the optimization of the magnetic field. A success of the experiment will eventually result in a change of future test reactors from the tokamak to the stellarator concept.

The stellarator concept utilizes a complicated configuration of coils to generate a poloidal and toroidal magnetic field. In this way the problems that plague tokamaks at driving the toroidal current for the generation of the poloidal magnetic field and the accompanying instabilities are avoided. In addition, this allows for a steady state operation without a need for a current drive. A comprehensive understanding of the interplay between the magnetic topology or the configuration effects and the quality of the magnetic confinement and the plasma parameters is very important for stellarator physics. For the measurement of the plasma edge parameters and especially with fast probes the Multi-Purpose-Manipulator (MPM) was installed. The manipulator allows a flexible mounting of probe heads and material samples. A development for the measurement of these edge parameters are the to date two iterations of the combined probe head. This work is describing the measurement with probes on the stellarator W7-X, including a comparison with a choice of other edge diagnostics and modelling.

The combined probe was used to measure the radial profiles, during the fast plunge of the manipulator, of the magnetic field with pick up coils, the electron temperature and density with Langmuir probes, the ion temperature with an ion sensitive probe and the relative flow velocities with a Mach probe. The measurements of the poloidal correlation reflectometer and the infrared camera, which observed the limters and divertors and the EMC3-EIRENE modelling were prominently used for the comparison. The measurements were conducted in both limiter and divertor configurations. In the limiter phase the modification of the iota and of the edge islands was successfully measured with the combined probe by tuning the planar coil currents.

The higher densities and heating powers in the divertor phase allowed a study of the influence of the plasma beta and the plasma currents on the measured edge parameters and the magnetic topology. The data from the combined probe, the limiter/divertor Langmuir probes and the radiated power can be used for the EMC3-EIRENE modelling, which in turn allowed for cross-checking the diagnostic results. In addition, the ion temperature profiles were supplied as an output from the modelling. The calculation of the electron contribution to the heat flux in the mid-plane, where the manipulator is located, in comparison to the total heat flux on the divertor made an experimental estimation of the ion temperature possible. By using the ion temperature from the modelling, it was also possible to observe the effect of the iota scan on the heat load asymmetry, that was observed in the standard limiter configuration.

A major part of the thesis was devoted to the measurements in the plasma edge. While the modelling can give a certain estimate for the position of the last closed flux surface, a multitude of effects and experimental conditions like the use of the correction or trim coils and later the beta effects could cause the plasma to deviate wildly. Since the decay length was in the order of about a centimeter, a compromise between the best results close to the last closed flux surface and a possible fatal burning of the probe had to be found.

Contents

Acknowledgments

I would like to first express my gratitude to my supervisor Prof. Dr. Yunfeng Liang, who allowed me to pursue my studies and experiments in the field of plasma physics with considerable freedom and encouragement. I want to thank Prof. Dr. Georg Pretzler, my second supervisor at the Heinrich-Heine Universität, who supported me all along my thesis work with suggestions and encouragment.
In this vein I would like to also thank Dr. Michael Rack, Dr. Peter Denner, Dr Shaocheng Liu, and Dr. Andreas Krämer-Flecken, who have given a lot of useful criticism on and suggestions for my work, since I started with my master thesis. I also want to thank Dr. Olaf Neubauer as my second internal mentor for his support and suggestions during my PhD thesis and the experiments in Greifswald.
Furthermore, I want to thank my colleagues Dr. Nengchao Wang, Jianquing Cai, Marion Henkel and Dr. Carsten Killer who have colloraborated with me on various probes. A special mention deserves Holger Niemann for his analysis and provision of the heat flux data on the limiters and the divertor modules.
I would like to thank just as much Jörg Cosfeld who supplied data from the modelling for the comparison of the up downstream heat fluxes. For their help and support regarding all administrative matters I want to thank Marlene Hoffmann and Judith Schönbrenner.
For his great help concerning all configuration and plasma equilibrium issues at W7-X I want to thank Dr. Joachim Geiger, his help in understanding the machine was invaluable.
I want to thank Dr. Michael Endler, Dr. Kenneth Hammond and Lukas Rudischhauser for their help and support with the Limiter and Divertor Langmuir probe data.
For the preparation and setup of the Multi-Purpose-Manipulator and all electronics associated with it I want to thank Dirk Nicolai, Guruparan Satheeswaran, Klaus Peter Hollfeld, Thomas Krings and Robert Günter.
For the support in developing the probe heads and the assembly Daniel Höschen, Tim Rüttgers and Norbert Sandri deserve my appraisal. I would also like to thank Marcin Jakubowski and Sebastijan Brezinsek for their support and suggestions as the task force leaders for the divertor physics.
I would also like to thank my colleague Alexander Knieps for our continued work since we started at university and I very much appreciate our discussions and his help cleaning up my codes.

Finally I want to thank my parents who supported me all the way from school until now to pursue my education.

Chapter 1

Introduction

Nuclear fusion has the potential to replace fossil fuels as the main energy source. As opposed to fossil fuels, fusion energy is not limited by resources, but rather by our current understanding and technology. Research in fusion towards realizing a fusion reactor has been going on for more than sixty years. As climate change and a growing world population continue to pressure the world for a solution regarding sustainable and environmentally friendly energy production, the quest to make nuclear fusion on Earth a reality is more important than ever. It cannot be stressed enough that fusion energy has the potential to be a step for a technological revolution like the steam engine, the electrification (which made its predecessor obsolete) and nuclear fission. More so nuclear fusion has the potential to harness the nuclear forces in peaceful manner more than the nuclear fission ever could. The energy consumption is predicted to increase by 18% by 2030 and 39% by 2050 [2], which should underline the need for new means of energy production. All along Germany and other countries plan to reduce the release of carbon-dioxide considerably until the middle of the century. The community of fusion research, intentionally for purposes of promoting peace, has always been very international and is still growing. Apart from Europe and North America, also Australia, China, India, Japan, Korea and Brazil have joined the effort. The research started in the fifties the with stellarator by Lyman Spitzer [3] and Andrei Sacharow and Igor Tamm with the tokamak.

To date, the most advanced concepts for confined fusion are the tokamak and the stellarator. The latter is exemplified by the Wendelstein 7-X (W7-X) stellarator in Greifswald, Germany, which has recently completed its operational phases 1.1 and 1.2a. The tokamak scheme is currently the leading variant for plasma confinement and is therefore being used for the next-generation device ITER and is planned for the DEMO reactor. There has been considerable progress in the research, as machines like JET in the United Kingdom have, at least for short time, produced more energy, with a Deuterium-Tritium reaction, than invested for heating the plasma, but for the operation of a stable plasma and an efficient reactor, a better understanding of the processes involved with the magnetic confinement and instabilities is needed.

1.1 What is plasma?

At this point in the beginning the question "What is plasma?" should be asked. All of fusion research is revolving around plasma, thus one should know what it is. There are three states of matter, solid, liquid and gaseous. Depending on pressure and temperature matter can transition from any of the three to the others. At very high temperatures the molecular bond is broken, going even higher will see the ionization of atoms and thereby the separation of atoms and electrons. A neutral gas is turned into a plasma with free charge carriers (though the plasma is overall still neutral). In this "gas" the electron plasma frequency is much higher than the electron-neutral collision frequency, which causes electrostatic interactions to dominate over gas kinetics. These free charge carriers create electro-magnetic fields, that cause the atoms and electrons to interact with each other and also externally applied fields.

The plasma state of matter is peculiar, as it has to be described both as gas, due to the free movement of the species, but also as a liquid since instead of just interacting locally also collective effects play a role between the particles. The plasma state of matter is actually the most common in the universe as every star is essentially a huge fusion reaction. It was first described by the chemist Irving Langmuir in 1920, who is also the inventor of the Langmuir probe, that was the first diagnostic designed to study plasma properties. One speaks of a plasma if a sufficient amount of charge carriers is present, that can screen from outside electrostatic forces. This potential is the solution to the so called Debye-Hückel equation [1],the decay length of that electrostatic potential is the Debye lenght. The Debye length must be much smaller than the overall spatial extent of the plasma. Lightnings and sparks also serve as examples for a plasma present on earth, they are also good examples for the phenomenon of plasma being rather short lived, due to an abundance of neutral particles arround, that cause a rapid cooling and recombination. Also gas discharge lamps are an application of plasma for our day to day needs. Most plasmas in nature and in home-use tend to have higher densities but lower temperatures than fusion plasmas.

Finally, the solid state of matter cannot be fully disregarded as the wall in our plasma experiments is always present and indeed a huge part of the study for making fusion energy as commercially viable is devoted to the interaction between plasma and solid matter. The probes that are used to measure the plasma parameters also experience considerable exposure and while their interaction with the plasma is unavoidable the operator should attempt to limit its influence on the main plamsa.

The temperature of a plasma, one commonly speaks of a hundred million degrees Celsius in a future reactor, is normally measured in electron volts, which is also due to its beginnings from Irving Langmuir and the electrical Langmuir probes. It is also practical to measure in electron volt, because the binding energy of electron is measured in electron volts. For the most part in this thesis only plasmas in a thermal equilibrium are considered, meaning that both electrons and ions have the same temperature. In the vicinity of the divertor, where a considerable amount of neutral particles is found, this is naturally not the case.

1.2 The principle of nuclear fusion

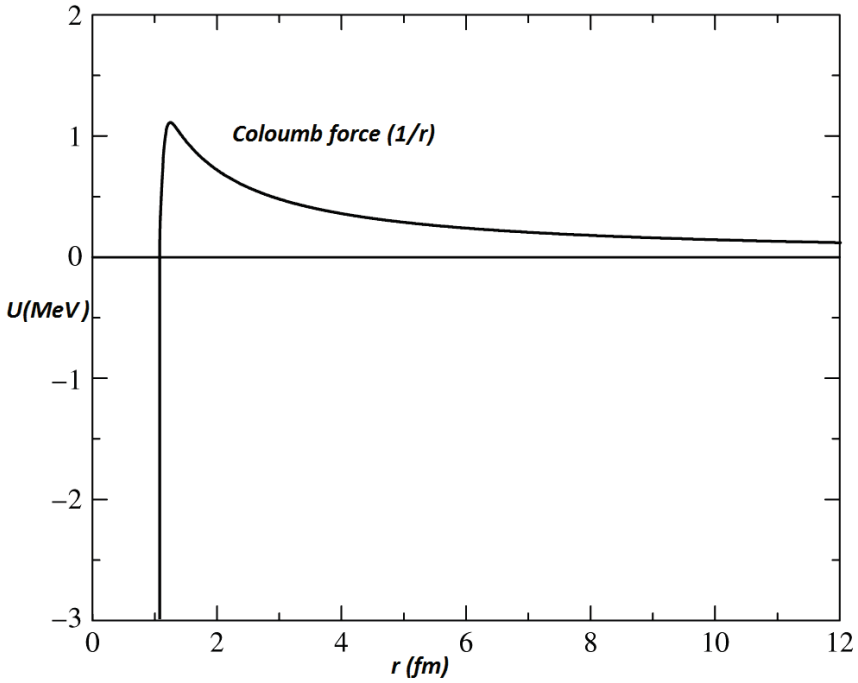

Figure 1.1: Repelling Coloumb force and attracting strong force, taken from [5].

The fusion of two nuclei via the strong force is possible due to quantum tunneling that allows overcoming the repelling Coulomb force (see figure 1.1), which would otherwise keep two positively charged bodies apart. A fusion reaction as observed in the stars and the composition of elements in the universe from nucleosynthesis is energetically favorable only for light elements, with a nucleon number of less than sixty (see figure 1.2). While stars can use elements way beyond carbon to sustain a fusion reaction [4], on earth the Deuterium Tritium reaction remains the most feasible, due to its large cross section at plasma densities and temperatures possible in fusion a reactor (see figure 1.3). Deuterium and Tritium fuse and the result is a Helium atom, a neutron and 17.6MeV energy (distributed as kinetic among the fusion products):

$$D + T \rightarrow {}^4\mathrm{He} + n + 17.6\mathrm{MeV} \tag{1.1}$$

Energies in the of the order of keV are necessary to sustain the fusion reaction. The helium atom has about 20% and the neutron 80% of the resulting kinetic energy. This makes confinement of these fast particles very important for a sustainable fusion reaction. The neutron still has about 14.1MeV and cannot be confined in any way, it represents a considerable problem for wall elements due to neutron damage. It also serves a necessary function as it can be used to breed tritium. A proposed element for this breeding is Lithium:

$${}^7\mathrm{Li} + n \rightarrow {}^4\mathrm{He} + T + 4.78\mathrm{MeV} \tag{1.2}$$

Currently only the JET experiment has performed Deuterium-Tritium discharges.

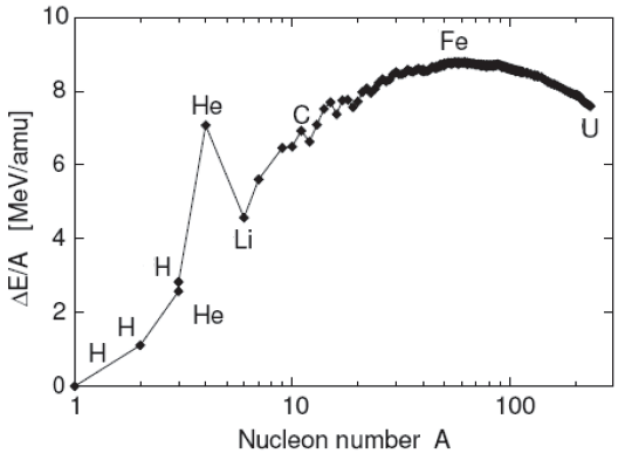

Figure 1.2: Binding energy of atoms per nuclei [6]

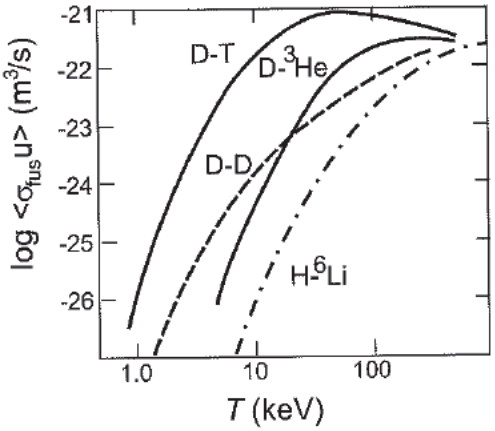

Figure 1.3: Cross section for fusion relevant isotopes and elements [6].

1.3 Magnetically confined fusion

The cross section of the fusion reaction is a limiting factor, since the necessary temperatures and densities, for most elements and isotopes, are only achievable by the virtue of the gravitational force of a star. For our purposes on earth, where gravitational confinement is not a possibility, magnetic confinement is the answer. The intended fusion reactors on earth will eventually have lower densities than the sun, but considerably higher temperatures. The main idea is that charged particles such as plasma tends to move along magnetic field lines and not perpendicular. Charged particles gyrate along the field with the distinctive Larmor radius:

$$r_{\mathrm{L}} = \frac{mv_{\perp}}{q|B|} \tag{1.3}$$

With m as the mass of the charge particle, $v_{\perp}$ the perpendicular velocity of the charged particle, q the charge and $|B|$ the absolute value of the magnetic field. It is impossible to describe the

movement of every individual particle, therefore the one fluid model can be used:

$$\vec{J} \times \vec{B} = \nabla p \tag{1.4}$$

$$\nabla \times \vec{B} = \mu_0 \vec{J} \tag{1.5}$$

$$\nabla \cdot \vec{B} = 0 \tag{1.6}$$

With $\vec{J}$ as the current density and p the plasma pressure. Following these equations one can deduce that both the current and the magnetic field are situated on surfaces of constant plasma pressure. They are called nested surfaces.

At the interface between the wall and the plasma an electric field will be present in the experiment, since electrons are far faster than the ions and reach the machine chamber walls faster. The electric field is associated with the outward $\vec{E} \times \vec{B}$ drift and the twisting of the magnetic field lines by imposing an additional poloidal magnetic field is necessary to cancel out its effects (tokamaks use the driven toroidal current for this while stellarators use their native coil setup). This twisting of magnetic field lines is described by the safety factor $q = \frac{m}{n}$ or more commonly used for stellarator the rational transform $\iota = \frac{2\Pi}{q}$, m being the number of toroidal and n the poloidal turns that a field lines traces through the machine.

1.3.1 Neoclassical transport and toroidal currents

The plasma becomes nearly collisionless at high temperatures which allows particles to travel for a long time before a collision displaces them. These particles are the majority, but some are trapped in a magnetic well formed by poloidal variations of the magnetic field. For an easier understanding the example of the simple magnetic mirror can be used [42]. The magnetic mirror is created by two solenoidal coils between $s = \pm s_{\max}$. The field would be the weakest in the middle at $s = 0$.
The first assumption for the simple mirror is that the kinetic energy W is conserved:

$$\frac{1}{2}\left[v_{\parallel}^2(s) + v_{\perp}^2(s)\right] = W = \text{const} \tag{1.7}$$

The conservation of angular momentum gives the following constraint:

$$p_\theta = m r_{\mathrm{L}} v_\perp = \frac{m v_\perp^2(s)}{B(s)} = \text{const} \tag{1.8}$$

This is rewritten for convenience to:

$$\mu = \frac{\frac{1}{2} m v_\perp^2(s)}{B(s)} = \text{const} \tag{1.9}$$

These two equations can be combined to:

$$\frac{1}{2} m v_{\parallel}^2(s) = W - \mu B(s) \tag{1.10}$$

In the case of $W/\mu = B(s)$ for $B_{\min} \leq B(s) \leq B_{\max}$ the parallel velocity $v_{\parallel}$ is zero and particles will be trapped. The relation of trapped to untrapped particles depends on the relation of $v_{\perp}(s_0)/v_{\parallel}(s_0)$ and $B(s)/B_{\min}$. This means that the loss of particles is big if the field inhomogenity is small.

Coming to the case of a tokamak with a toroidal symmetry but a poloidally varying field one can use similar arguments. The total energy is constant, while neglecting poloidal variations of the electrostatic potential one can assume the kinetic energy W to be constant. With that the parallel velocity is:

$$v_{\parallel} = \left[\frac{2}{m}\left(W - \frac{\bar{\mu}B^0}{h(\theta)} - e\Phi\right)\right] \tag{1.11}$$

With Φ as the electrostatic potential, B^0 is the magnitude of the total field and a function of theta representing the poloidal variation of the magnetic field. The particle is reflected if the parallel velocity $v_{\parallel}$ is zero:

$$\frac{\bar{\mu}B^0}{W - e\Phi} \geq h(\theta = \pi) = 1 - \frac{r}{R_0} \tag{1.12}$$

With R_0 as the major radius and r the radial position in the torus.

This trapping of particles combined with a pressure gradient is a source for the bootstrap current [7]. Consider two trapped ions with the same energy and magnetic moment, that start on the same magnetic surface with a different sign of the parallel velocity. The ion with the negative parallel velocity drifts inwards while the ion with the positive parallel velocity will drift outwards. The average orbit of the former is smaller while the latter is larger. A radial density gradient will cause a increase and decrease of the population of ions. The electrons behave similarly with an opposite sign due to their negative charge. This asymmetry will cause a net current along the magnetic field. Passing particles in a similar manner contribute to the bootstrap current through collisional coupling of trapped and passing particles. The currents later referred to as toroidal current, in the description of the measurements of the OP 1.2a measurements, are most probably bootstrap currents, but their current distribution is not measured or known. The only information obtained from the diagnostics is the magnitude and direction of the total toroidal current.

1.3.2 Scrape-off layer physics

Describing each individual charged particle in a plasma is highly impractical, therefore collective effects are used to describe the electrons and ions. For a positively charged ion electrons will be attracted and ions repelled, this process is fluid in the way that both species are not tied to each other but the Coloumb force excerting on the particles will cause a slight shift in the particle trajectories. This effect will lead to an effective local shielding and limit the effects of the Coloumb force to small sphere arround the charge carriers. While the plasma is assumed to be neutral $n_\mathrm{e} = n_\mathrm{i}$, local variations do exist. Considering the Maxwell or Mawell-Boltzmann distribution for electrons:

$$n_\mathrm{e} = n_0 \exp\left(\frac{e\Phi}{T_\mathrm{e}}\right) \approx n_0 \left(1 + \frac{e\Phi}{T_\mathrm{e}}\right) \tag{1.13}$$

The first order approximation was done by assuming $e\Phi << T_\mathrm{e}$.
The electrostatic potential Φ is formed due local nonuniformities of the electron distribution, which can be expressed as the difference between the unperturbed and perturbed electron density $e\,(n_0 - n_\mathrm{e})$. The local electrostatic potential satisfies the Poisson equation:

$$\nabla^2\Phi = \frac{e\,(n_0 - n_\mathrm{e})}{\epsilon_0} \tag{1.14}$$

The Debye sheath that measures how effectively a potential is shielded is then:

$$\lambda_\mathrm{Debye} = \sqrt{\epsilon_0 T_e / e^2 n_\mathrm{e}} \tag{1.15}$$

Higher densities cause a shorter Debye length, which means that a local potential is more effectively shielded. This quantity is well suited to ascertain if the probe pins on the front face of the combined probe interfere with each other.

The plasma can be broadly categorized into two regions, the confined region inside the last closed flux surface, which is marked by very long connection lengths to the divertor and the scrape off layer (SOL) with short connection length outside of the last closed flux surface.
The simplest concept to define the plasma edge and to manage the interaction between the plasma and the wall is the so called limiter, normally placed poloidally or toroidally along the inner wall of the device. Limiter enjoy typically a large plasma wetted area and lower power loads, but experience trouble with the pumping and recycling of impurities. This was employed in the first operational campaign of W7-X

The second option is the use of various divertor configurations. The magnetic field lines are diverted onto the divertor plates. This is normally done with coils, that carry current in the same direction as the plasma current. They create a X-point in the net toroidal field as depicted in figure 1.4. Field lines that pass through this X-point define the last closed flux surface, this is called the separatrix. Particles that cross past this point into the "private" region are led to the divertor plates. They will recycle here, but are hindered from reentering the main plasma again, due to the closed field lines at the last closed flux surface. The temperature and density profiles

decay far more rapidly in divertor plasmas and normally have a considerably smaller SOL region. The second operational campaign at W7-X saw the use of various island divertor configurations. The cross field transport in the scrape off layer can be described with a simple model with no particle sources and sinks (for example ionization and recombination), the particle flow across the magnetic surfaces should be balanced by parallel transport:

$$L_c \frac{\mathrm{d}}{\mathrm{d}r}\Gamma_\perp - D_\perp \frac{\mathrm{d}n}{\mathrm{d}r} = \Gamma_\parallel = n v_\parallel \tag{1.16}$$

This relation can be used to approximate the scrape off layer profile to be exponentially decaying. The density decay length λ_{n_e} was obtained from:

$$n_\mathrm{e}(r) = n_0 \exp\left(-\frac{r - R_0}{\lambda_{n_\mathrm{e}}}\right) \tag{1.17}$$

The temperature decay can be calculated analogously to this:

$$T_\mathrm{e}(r) = T_0 \exp\left(-\frac{r - R_0}{\lambda_{T_\mathrm{e}}}\right) \tag{1.18}$$

The electron pressure is calculated using the temperature and density profiles by multiplying n_e and T_e. From this electron pressure profile the power decay length λ is deduced by fitting the function below to the data:

$$p_\mathrm{e}(r) = p_0 \exp\left(-\frac{r - R_0}{\lambda_{p_\mathrm{e}}}\right) \tag{1.19}$$

For R_0 the values of the position of the last closed flux surface calculated by the field line tracing tool were used. These decay lengths are directly proportional to the perpendicular diffusion coefficients via the relation:

$$\lambda_{\mathrm{n_e}} = \sqrt{D_\perp L_c / v_\parallel} \tag{1.20}$$

The decay lengths help to understand and compare the handling of the power loads in different machines, since for small decay lengths it is expected that the heat will be spread over a smaller area and thus also more difficult to cool. The flux can be used together with the electron and ion temperature to calculate the parallel heat flux:

$$q_\parallel = \Gamma_\parallel T = n v_\parallel T \tag{1.21}$$

The ion sound speed c_s can be used for the lower boundary of the parallel velocity $v_\parallel$. The parallel heat flux can be calculated using the data from probe measurements, but as long as only Langmuir probes are used, assumptions must be made on the magnitude of the ion temperature. It is also necessary to take the field angle on the limiter and divertor modules into account to get an effective heat flux:

$$q_\mathrm{wall} = \Gamma_\parallel T \sin(\alpha) \tag{1.22}$$

There are different causes for cross-field transport, that is related to the fluctuation of different quantities that can measured with the Langmuir probes used on the combined probe head. One possible candidate is the electrostatic transport $\Gamma_\mathrm{r}^\mathrm{ES}$, originating from fluctuation of the poloidal

electric field $\tilde{E}_\theta$. It will cause an $\tilde{E}_\theta \times B_\phi$ drift and together with a density fluctuation a radial current:

$$\Gamma_{\mathrm{r}}^{\mathrm{ES}} = \frac{1}{B_\phi}\langle \tilde{n}\tilde{E}_\theta \rangle \tag{1.23}$$

Both the density and the poloidal electric field are mostly functions of the potentials measured with the Langmuir probes and the ion saturation current. This behavior is closely linked to so-called filaments. Electro magnetic fluctuation can cause a radial flux $\Gamma_{\mathrm{r}}^{\mathrm{EM}}$, in the case that magnetic flucations in the radial direction $\tilde{B}_{\mathrm{r}}$ and density fluctuations are correlated, this can be measured and studied again with the Langmuir probes and the 3D coils that are held within the probe.

Another important feature of both limiter and divertor configurations is the formation and growth of magnetic islands at the sites of rational values of the safety factor q. Islands short circuit the transport by allowing heat and particles to move radially outwards instead of diffusing. The field lines are wound helically around the island and connected regions closer to the core plasma with those located further outwards.
This is normally observed by locally longer connection lengths. The radial transport in the island

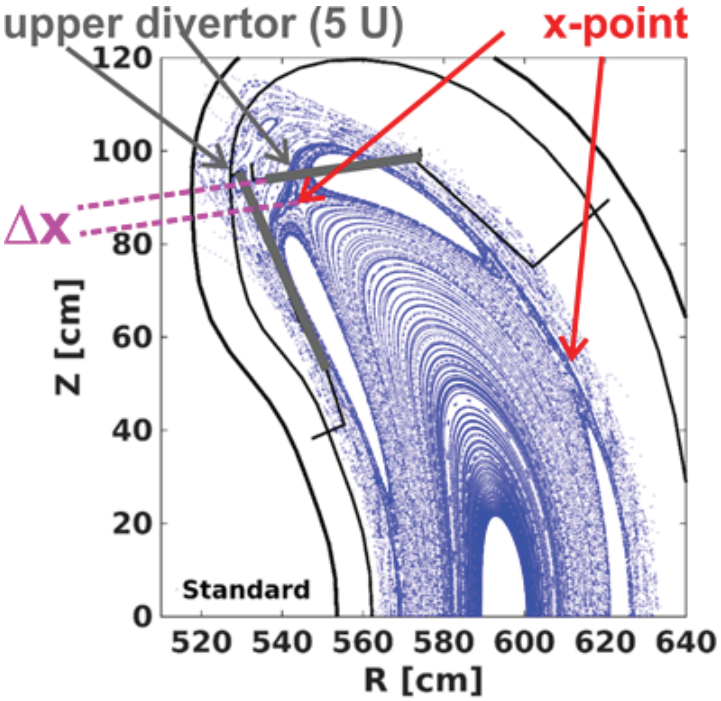

Figure 1.4: Poincaré cross section of W7-X, indication of the x-point (red) and divertors (grey) (taken from [8]).

is therefore strongly enhanced since, effectively the radial transport in an island is dominated by parallel transport that can be several orders of magnitude bigger than the perpendicular one. In the case of an island divertor the field lines are in addition open towards the divertor, which

slightly complicates the picture when interpreting Poincaré plots. The rapid transport is possibly visible in the electron temperature profiles and to a certain extent also in the radial electric field. The stellarator Wendelstein 7-X (W7-X) posses natural islands produced by their vacuum magnetic field.
In the case of W7-X the coil configuration and currents have a much stronger effect on the presence of islands. But at high plasma betas it is possible that the flattening of the pressure inside the magnetic island, due to enhanced transport, causes an instability that leads to an island growth. The bootstrap current is proportional to the pressure gradient and so called neoclassical tearing modes (NTM) [9] can arise at higher betas.
They require the presence of a seed island, thus this effect can only increase already present islands. It should be mentioned here that currents in the plasma can also shrink the magnetic island. An overlapping structure of magnetic islands becomes a stochastic region, the magnetic field lines become chaotic, with a strongly enhanced radial transport.

The heating powers and densities have been gradually increased from the first start up of the machine to the end of the first phase of the second operational campaign and will continue to do so. This has a profound effect on the magnetic field topology and the islands, since the plasma beta is highly affected by this and in turn also the bootstrap currents, that scale with the pressure gradient. The plasma beta is the ratio of magnetic and plasma pressure:

$$\beta = \frac{p_{\text{plasma}}}{p_{\text{magnetic}}} \tag{1.24}$$

It is a good figure of merit for a fusion reactor design as it describes how effective the plasma is confined. For the estimation of the beta effects it is necessary to know the actual plasma beta of a discharge. One way to roughly calculate the plasma beta is by using the diamagnetic energy W_{dia} and the machine parameters such as the major R and minor r radius and the magnetic field strength B, under the assumption that the thermal energy and the diamagnetic energy are equal $W_{\text{therm}} = W_{\text{dia}}$:

$$W_{\text{therm}} = \frac{3}{2}\int \frac{\mathrm{d}V}{\mathrm{d}r} p(r)\mathrm{d}r \tag{1.25}$$

The energy of the plasma is proportional to the pressure and the plasma volume:

$$W \approx p \cdot V \tag{1.26}$$

The ratio of the magnetic pressure and the plasma pressure can therefore be approximated with:

$$\beta \approx \frac{p_{\text{plasma}}}{p_{\text{mag}}} \approx \frac{W_{\text{dia}} 2\mu_0}{VB^2} \tag{1.27}$$

The diamagnetic energy can be measured with the Rogowski-coils, the plasma volume and the mangetic field strength are known quantities.
The plasma beta is furthermore also used to quantify the effect of the plasma unto the magnetic field itself, as higher densities and higher heating powers will lead to stronger plasma currents. It is predicted for W7-X that the higher beta will cause a stochastization of the edge islands (in standard configuration)[10].

1.3.3 EMC3-EIRENE

Results from the EMC3-EIRENE code were used in this thesis for comparisons with the measured data. Indeed, the electron temperatrue and density profiles measured with the combined probe were part of the input for the modelling with EMC3-EIRENE itself. EMC3-EIRENE consists of two codes that are coupled, EMC3 is a Monte Carlo approach to solve the Braginskii fluid equations of mass, momentum and energy [11] for both electrons and ions, while EIRENE simulates the kinetic transport. Cross-field (anomalous) and a classical parallel diffusion-advection process describe the impurity particle balance. EIRENE is linked to several atomic databases with internal states, elastic and inelastic collision processes. Details can be found in [12][13]. It is the only 3D transport code that is in use for the modelling of the edge transport in W7-X.

The code depends on good input data. Several diagnostics like the manipulator mounted probes, the divertor Langmuir probes and the Helium diagnostic can supply temperature profiles. The radiated power is another important input, which is more difficult to evaluate, since most diagnostics only measure the total radiated power and not the losses in the plasma edge. A recent add-on for the code is the possibility to model plasma with main species of $Z > 1$, meaning that now not only hydrogen plasmas can be considered.

A publication directly using the manipulator data is [14], which also supplied the modelled profiles for comparison with the measurements. EMC3-EIRENE is able to produce 3D profiles from 2D sets of data, it is therefore an interesting venue for better understanding the transport processes at W7-X and matching results from different diagnostics onto each other. In addition, the code also provides profiles for the effective charge state of the ions and therefore supplies a quantity, which cannot be measured directly with a high spatial resolution in the edge.

1.4 Wendelstein 7-X

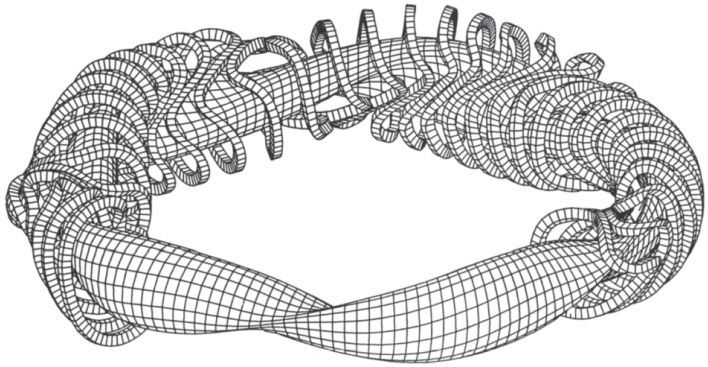

Figure 1.5: Coils setup and magnetic field of W7-X (taken from [15]).

The construction of Wendelstein 7-X was finished in 2014, the commissioning was completed in late 2015. The first operational campaign with a limiter configuration started in December 2015 and ended in March 2016. The first part of the second operational campaign began in August 2017 and ended in December of the same year. An uncooled divertor configuration was employed. Both the limiter and the divertor were made from carbon. Wendelstein 7-X is an optimized stellarator, meaning that it was attempted to improve the confinement of particle orbits. Previous stellarators suffered from this lack of good neoclassical confinement, due to the field line curvature and inhomogeneities inherent to the magnetic topology.

A tokamak does not suffer from this problem as toroidal symmetry allows particles drift to average out. Improved theory and calculation [17][16] make configurations possible that strongly reduce the drift losses to an extent that stellarators are an economical alternative to tokamaks for a future fusion power plant. Previous machines showed good promise in the application of this theory [18], but these devices were too small to reach sufficient ion temperatures to really test the optimization.
The averaged beta that was aimed for is about $\beta \approx 5\%$, with good equilibrium properties to achieve a stiff configuration. W7-X features a superconductive coil system that will with the water cooled divertors prove steady state capability. The confinement volume is about $30\,\mathrm{m}^2$, W7-X and Large Helical Device LHD are therefore the largest stellarators currently operated.
A good collection of reasons and requirements for the stellarator W7-X can be found in G. Grieger's paper on the concept of modular stellarators [15]:

> Modular stellarator reactors of the Advanced stellarator type appear to have the potential to offer desirable reactor properties:
> i) a single NbTi coil system is sufficient;
> ii) steady-state operation is inherent and rests upon refuelling and exhaust only (no current drive system is needed);
> iii) there is no possibility for a major current disruption because there is no net

toroidal current;
iv) reactor volume, mass and magnetic field energy are comparable to those of tokamak reactors.
The Wendelstein 7-X experiment will provide an integrated concept test which is needed for producing convincing predictions on the properties of this reactor approach.

He also further elaborates that the achievement of the steady state scenario, the optimization of the neoclassical transport and good equilibrium properties to achieve a stiff configuration define the design, that simultaneously fulfills those criterias. For the first operational campaign OP. 1.1 and the first phase of the second OP. 1.2a only electron cyclotron resonance heating was available.

The core electron and ion temperatures are planned to be in the range of keV and the core electron density of the order of $10^{20}\,\mathrm{m}^{-3}$. As shown in figure 1.6 W7-X is intended to have a five-fold symmetry. There are 70 NbTi magnets, four planar coils and 10 non planar coils in each module. The coil system is designed for an operation with $B_0 = 3\,\mathrm{T}$ (a value of $B_0 = 5\,\mathrm{T}$ was aimed for originally in [15] to accomodate current NbTi magnet technology). The machine has a major radius of $R_0 = 6.5\,\mathrm{m}$ and a minor radius $r = 0.53\,\mathrm{m}$.

The electron cyclotron resonance heating system is intended to supply a heating power of up to 20 MW, but typically operated at a maximum of about 5 MW. For the second campaign in the second phase OP. 1.2b in addition Neutral Beam Injection (NBI) and Ion Cyclotron Resonance Heating (ICRH) are added. As working gases for the plasma hydrogen and helium are used. Both the limiter and the divertor are non actively cooled carbon assemblies placed on copper tiles. The system has a fivefold symmetry that in theory should allow a comparison between

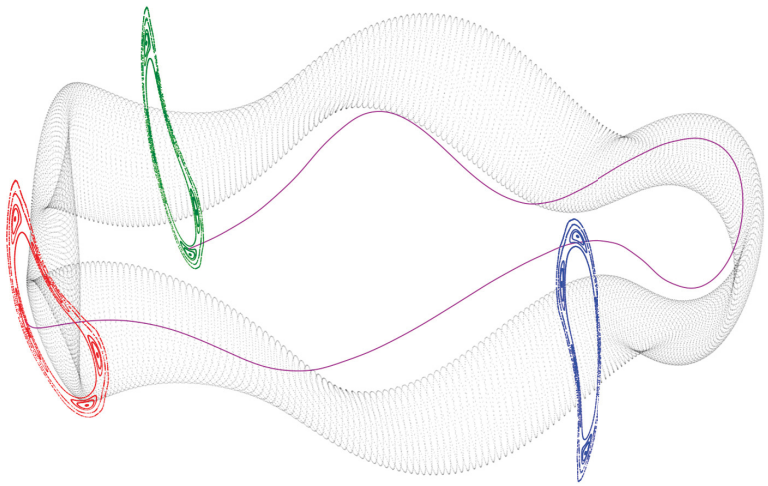

Figure 1.6: Magnetic field structure of W-7 X with a single field line traced through the fivefold symmetry.

diagnostics that are situated in a similar effective radius but not in the same flux tube or island. In the limiter and also in the divertor configuration deviations from that assumed symmetry are

observable, due to error fields and misalignment of machine components. This asymmetry is the cause of unequal distribution of loads on the plasma facing components.
These asymmetries can also be studied with the manipulator mounted probes, since the field lines normally connect the measurements to at least two different limiter or divertor modules. The influence of the magnetic configuration is studied in subsection 3.1.2 for the limiter configuration by tuning the planar coils and for the divertor configuration in subsection 3.2.2 by the modification of the plasma beta.

Apart from the probes on the Multi-Purpose-Manipulator, the correlation reflectometry and the infrared cameras are used prominently for the analysis of this thesis. Additional information such as the effective charge measurements from the spectroscopy are important too, but they normally will not supply data with the sufficient resolution in the edge, therefore results from the EMC3-EIRENE transport simulation should be used whenever accurate values are necessary.

Chapter 2

Development of the Multi-purpose Manipulatorfor edge profile measurements

For the measurement of the edge plasma profiles such as the electron temperature and density, the ion temperature, the local magnetic field and the radial electric field the multi-purpose manipulator was employed as a carrier system to plunge diagnostic probes into the plasma edge [19][20]. The manipulator itself is a complex tool which is still being upgraded to accommodate all planned functions. The preparation of the manipulator and the necessary backend electronic for the measurements are described.

The combined probe and the upgraded combined probe used prominently are detailed in this chapter. The situation with the combined probes and other probe heads as well is similar to the manipulator, the functionality is achieved but improvements are still possible. The probe measurements present a vivid topic of discussion concerning the interpretation and also the deployment of them into the plasma.

2.1 The Multi-purpose Manipulator

The multi-purpose manipulator shown in figure 2.1 is one of the contributions of the Forschungszentrum Jülich to the stellarator experiment W7-X. The key objectives of the device is to provide a safe and stable platform for experiments to be mounted on. It will be used to insert electric and magnetic probes into the plasma edge, to obtain the radial plasma profiles of T_e, n_e, V_p, B and the parallel flow and the exposition of test samples in the plasma for plasma-wall-interaction studies. The position of the measurements relative to the magnetic island strongly depends on the coil configuration and plasma parameters, while the manipulator is only able to vary the plunge depth, but not its toroidal or poloidal position.

A similar manipulator was already used at TEXTOR for the measurement of the edge plasma profiles [21], but concerning design both devices differ considerably. The main difference is that the new one lacks the ability to rotate the probe head [22]. The aforementioned lack of the rotation feature is actually a way to address the issue of the unreliable sliding contacts and the

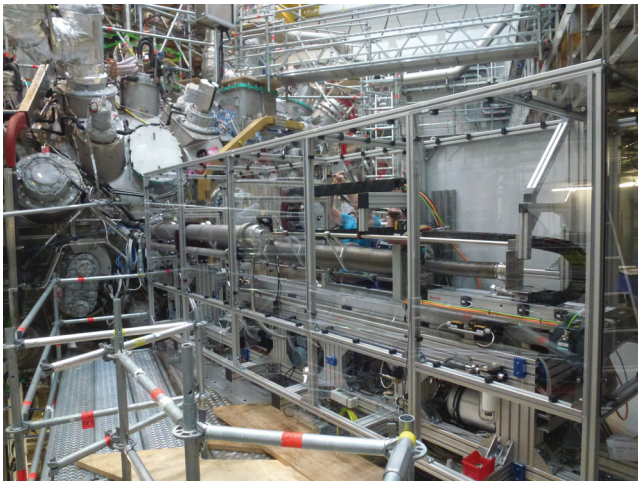

Figure 2.1: Installed Multi-purpose manipulator at W7-X.

prohibition of the use of rubber seals, which otherwise had to be used. The second big difference is the need for a slow axis to move the probes through the rather extensive cryostat.
In the first campaign a combined probe head was used, in the second campaign a more complex Mach probe, a retarding field analyzer (RFA)[23] for the measurement of the ion temperature, a dedicated fluctuation probe and a material sample holder were used. The manipulator is still being upgraded todate to further improve the capabilities and the ease of operation. The probe heads might overshadow the manipulator, but the back-end systems play a crucial role in obtaining good quality measurements.

2.1.1 Components

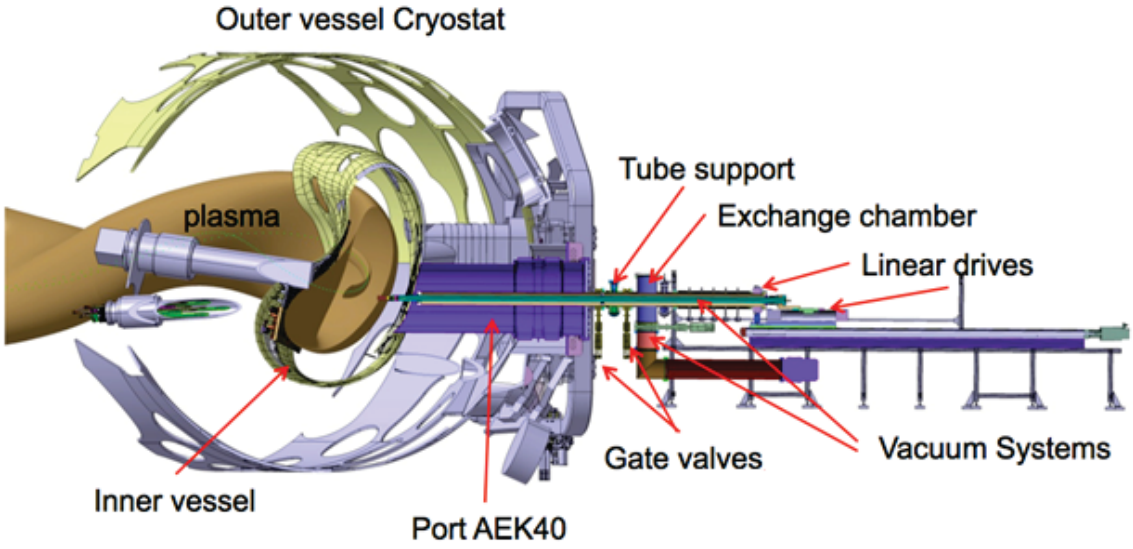

Figure 2.2: Setup of the manipulator, with the support system and the private vacuum chamber for the probe exchange.

The components of the manipulator are shown in figure 2.2, to sum up the main components and functions of the manipulator:

- slow axis, enables the positioning of the probe for measurement and maintenance, like the changing of the probe heads
- fast axis, used for the plunge into the plasma edge
- an intermediate vacuum for operational safety
- distinct chamber for changing the probe head
- probe conditioning with up to 300 °C

The manipulator consists of two linear drives, whereas the fast one is mounted on the slow. The support pipe is mounted on the rail of the slow drive, of 2.5 m length. The carrier pipe is inserted into the vacuum of the support pipe, which is housing the cooling and cabling for the probe head. At the two ends of the slow axis are pistons that hold the sledge in place, to provide operational safety when changing the probe and for absorbing the shocks due to the fast motion.
The axis for the fast drive is only activated in the position at the AEK-40 flange and in the parking position for the mechanical testing of the probe head. The maximum acceleration predicted was 3 g and velocities of up to $4\,\frac{\mathrm{m}}{\mathrm{s}}$. The planned acceleration is about 2.5 g, this was done to ensure the mechanical and dynamical stability of the manipulator. The maximum length of the fast axis is 350 mm, for the upcoming campaign 300 mm are choosen. Apart from the internal system measuring the position, via the rotation of the drives, a laser positioning system is used to

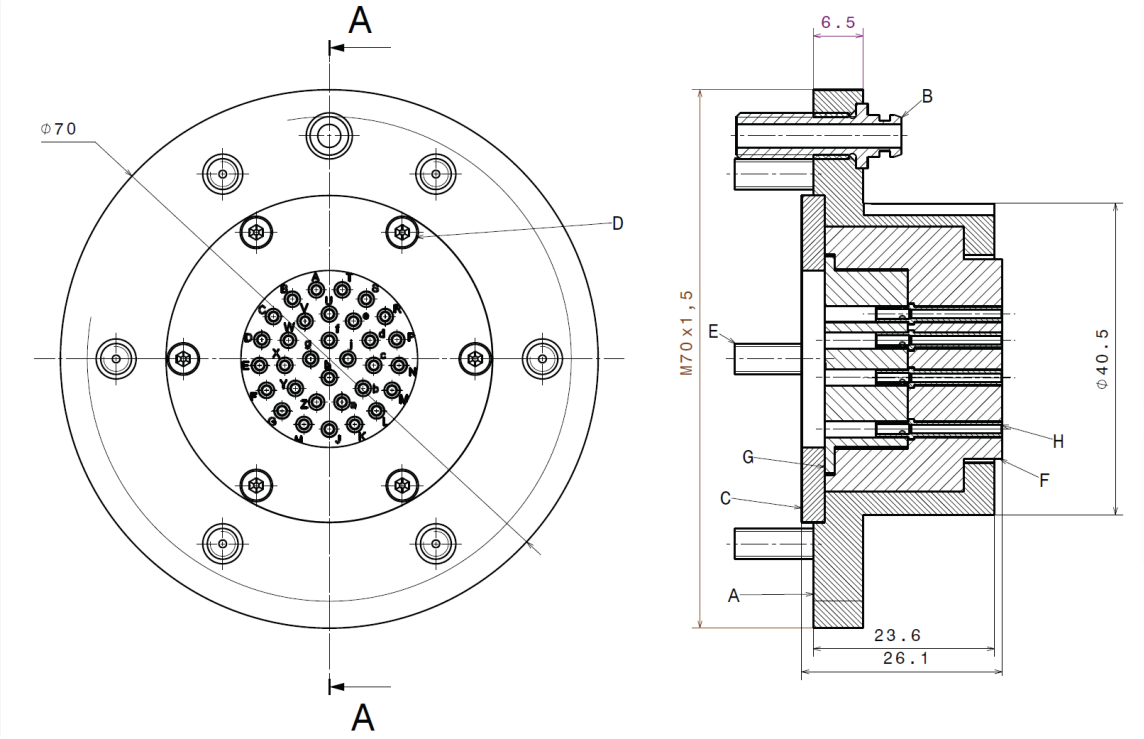

Figure 2.3: Interface for probes on the Multi-purpose manipulator.

measure the distance. The interface for mounting probes on the multi-purpose manipulator is shown in figure 2.3. It has 32 pins to connect diagnostics. It is possible to supply voltages of up to ±200 V and currents of 2 A.

2.1.2 Commissioning of the manipulator

The testing of the manipulator was done to ensure the compatibility of the two linear drives concerning nonlinear behavior. The fast movement of the manipulator brings considerable forces to bear on the device. One of the effects of this is vibration, that will invariably lead to unwanted displacement at the probe head. This vibration could prove to be critical since the manipulator pipe housing the cabling and water cooling has a potential compared to the overall device for biasing experiments with an externally controlled electric field [24]. This is a planned feature for which preparations in the device are done, but it is not yet operational.

In the case of displacements of the pipe at the far end of the manipulator, in respect to the vacuum chamber, a short cut with the diaphragm bellow could happen. The diaphragm bellow was chosen to be as small as possible to reduce the amount of necessary pumping and to reduce the mass, that would exacerbate the problem of inertial effects during the plunge. Therefore in test runs a fast camera was used to monitor the displacement of the probe head, which in turn showed, that due to the ramping of the speed, displacements are minimal and a shortcut unlikely.

The manipulator contains two Endevco 7290 single axis accelerometers in the manipulator pipe close to the interface and one in radial direction on the fast drive, which will measure the displacement of the probe during operation. The sensors have a range of 10 g and a sensitivity of 200 $\frac{\mathrm{mV}}{\mathrm{g}}$ [25]. The two sensors in the tube of the manipulator are 549.3 mm behind the probe-manipulator interface, since the space within the probe head is quite constricted and would limit the use to only a single probe head. Therefore this feature will be available for all measurements done with the manipulator.
Figure 2.4 shows the two acceleration sensors attached to the cable support discs in the inside of the manipulator pipes. Due to the already existing constraints of the cabling, the gas puffing system and water cooling, a slight angle at the r-axis of 4.331 ° is present. Therefore the measured data vector of the acceleration has to be transformed, to eliminate eventual pick up. The radial

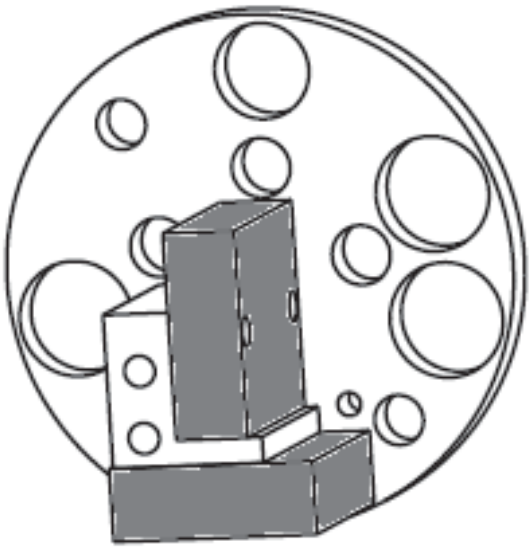

Figure 2.4: Setup of the two acceleration sensor on the inner cable support.

positioning was tested using a laser distance measuring system, while the radial acceleration was measured with the accelerometer shown in figure 2.5. There is an obvious time delay due to the averaging of 0.0681 s due to the averaging filter of the positioning system. The main feature of the controls clearly visible here is, that the displacements are minimized since the speed is slowly ramped up and down when approaching the two most extreme positions.

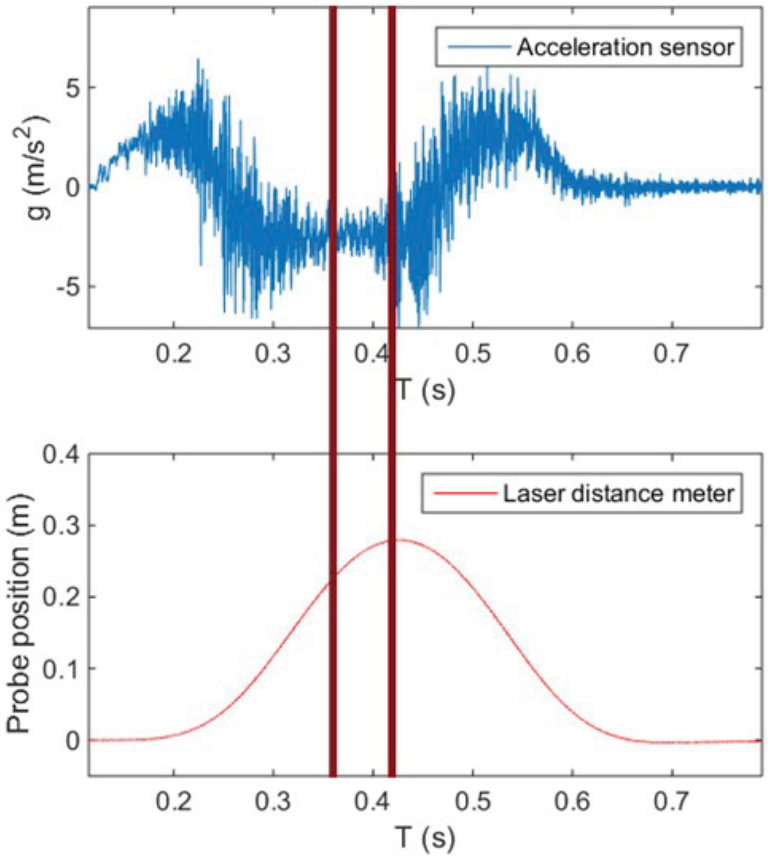

Figure 2.5: Test of the radial acceleration of the manipulator; Top figure: Acceleration measured with the Endevco 7290; Bottom figure: Probe position measured with the laser distance measurement system, the red lines mark the delay between the acceleration and the positioning.

2.2 Development of the combined probe

The combined probe head will be used to measure the radial distribution of the magnetic field with magnetic pick-up coils [26], as well as the plasma temperature, density profiles and the radial electric field with Langmuir pins [27] and the plasma flow with a Mach setup[28]. The merit of this setup is the possibility of combining several measurement techniques, but this also means that the space within the device is severely limited. The size is very important since a probe inserted into the plasma is disturbing its own measurement. The modelling in [29] suggests that there is a strong dependency of the modification of the floating potential and also the reduction of turbulences, in proximity of the probe, on its size. This means that within certain safety precautions, like sufficient wall thickness, one should try to keep the probe as compact as possible.

The interior of the probe head is shown in figure 2.6. The ceramic parts used for the place

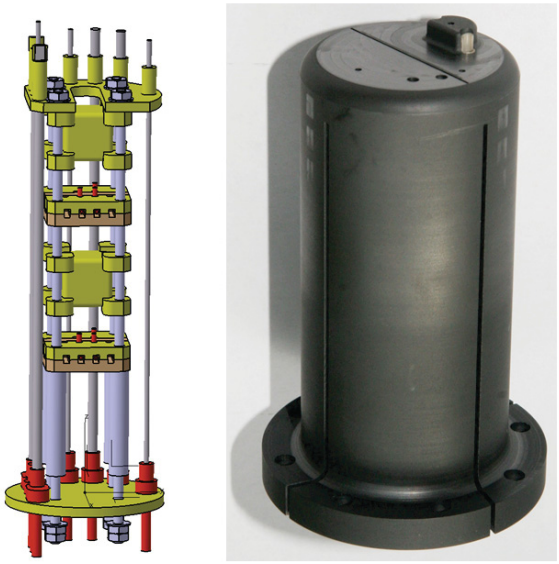

Figure 2.6: Right: Interior setup of the combined probe. Left: Shielding for the combined probe head.

holder at the bottom, below the two pick-up coils, the pick-up coils themselves and the isolator at the top are marked yellow. The support rods made of stainless steel are shown in blue-grey and the tungsten pins for the Langmuir and Mach probes in grey.
Not only for this specific probe head, but for all future probes, that will be used in conjunction with the multi-purpose manipulator, a linear drive is under construction. It will test the mechanical strain placed upon the devices mounted on the multi purpose manipulator during a plunge.

2.2.1 Magnetic measurements

The pick up coils were used to measure the magnetic field profiles. The direct comparison of the calculation from the field line tracing web service and the measurement is difficult due to the pick up coils detecting the temporal change:

$$\dot{B} = -\frac{U_{\text{induced}}}{AN} \tag{2.1}$$

with A as the pick-up coil area, N the number of coil windings and U_{induced} the induced voltage. After integrating the resulting $\dot{B}$ it is possible to calculate the gradient in radial direction which is independent of any integration constants. The pick-up coils used for the measurement of the magnetic fields, are 3D coils wound around each other, their number of windings is $N = 300$. The frequency limit of the coils is not beyond the expected measurable fluctuation due to the graphite cover. The wiring of the coil uses 0.1 mm copper wire with Polyimide or so called Capton coating. This insulation is resistant to temperatures of up to about 400 °C. This represents the limiting factor of our probe setup concerning the duration of the plasma exposure and also the depth of the plunge. The actual tolerable heat loads will be tested, by increasing the plunge depth and the duration in the plasma. In order to measure the temperature and monitor this hazard, two temperature probes are also installed within the shielding. Measurement with a network analyzer were also done on site to ensure, that there is no resonance present in the pick up coils in conjunction with the supply cabling.

For the cover, shown in figure 2.6, of the combined probe 5 mm of ISO-63 Graphite was used. The shielding of the probe head enables the most important function necessary for any measurement, it protects the diagnostics from unwanted direct plasma contact and possible damage from the Electron Cyclotron Resonance Heating (ECRH) [30]. Graphite was mainly chosen for its high heat resistance, good behavior under mechanical stress and compatibility with the ECRH heating system as opposed to boron nitride used previously at TEXTOR. Boron nitride shieldings experience a very high degree of heating due to a resonance with the ECRH heating system [31]. This ECRH forced the use of the full shielding instead of the slided cover, since the microwaves were still able to penetrate into the small inlets nonetheless. Such a shielding has repercussions also on the magnetic measurements and the installation of the probe pins. A time changing magnetic field will induce eddy currents in the cover, which increase with the frequency. Figure 2.7 shows that the measured magnetic field with the full shielding is greatly attenuated in the range beyond 40 kHz for a graphite cover, later used boron-nitride covers do not have this issue. Opposed to that, the pick-up coils are capable of measuring magnetic fields in the high kHz range, but this is stymied by the aforementioned shielding of the graphite cover. For measurements beyond 40 kHz efforts must be undertaken to recover the original amplitude of higher frequencies by using the data from the shielding measurement. This will necessarily result in problems of the signal to noise ratio. The graphite also makes it necessary to check thoroughly that the electric components, namely the pins for Langmuir and Mach probes do not touch the graphite.

Figure 2.8 shows the profile of the magnetic field gradients for the two pick up coils and the calculated values from the field line tracing code, the expected magnetic field values match those

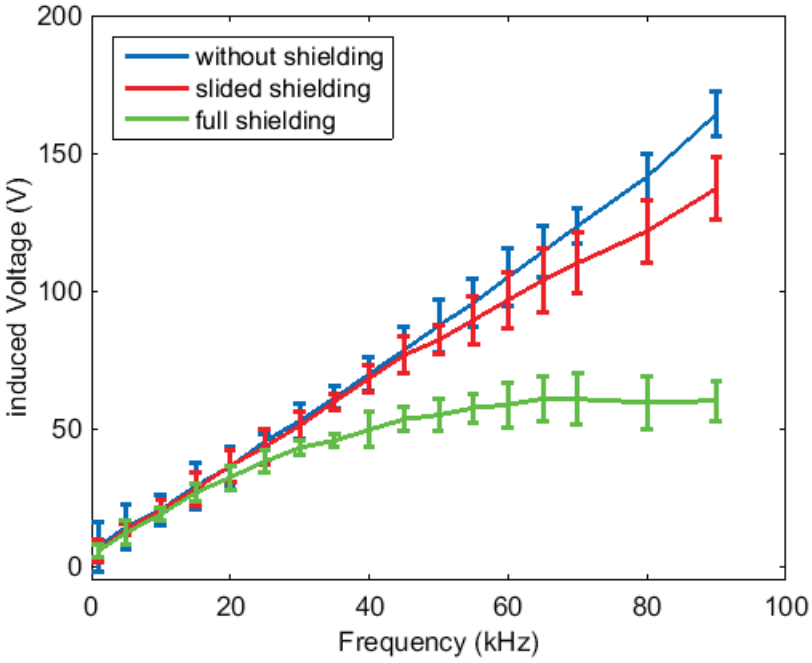

Figure 2.7: Test of the attenuation of the measured magnetic field with slided shielding, full shielding and without shielding in dependence of the frequency (taken from [32]).

of the measurements. The densities and the heating were not yet high enough to sufficiently impact the magnetic configuration and therefore the field is very close to the vacuum case. Thus is was not possible in the first campaign to study beta effects, as the plasma was not able to affect the magnetic configuration in a measurable way. Still, the changes due to configuration can be studied. For the OP. 1.2b a signal integrator to correct the drift more reliably instead of a simple after correction with the measured data will be installed [33].

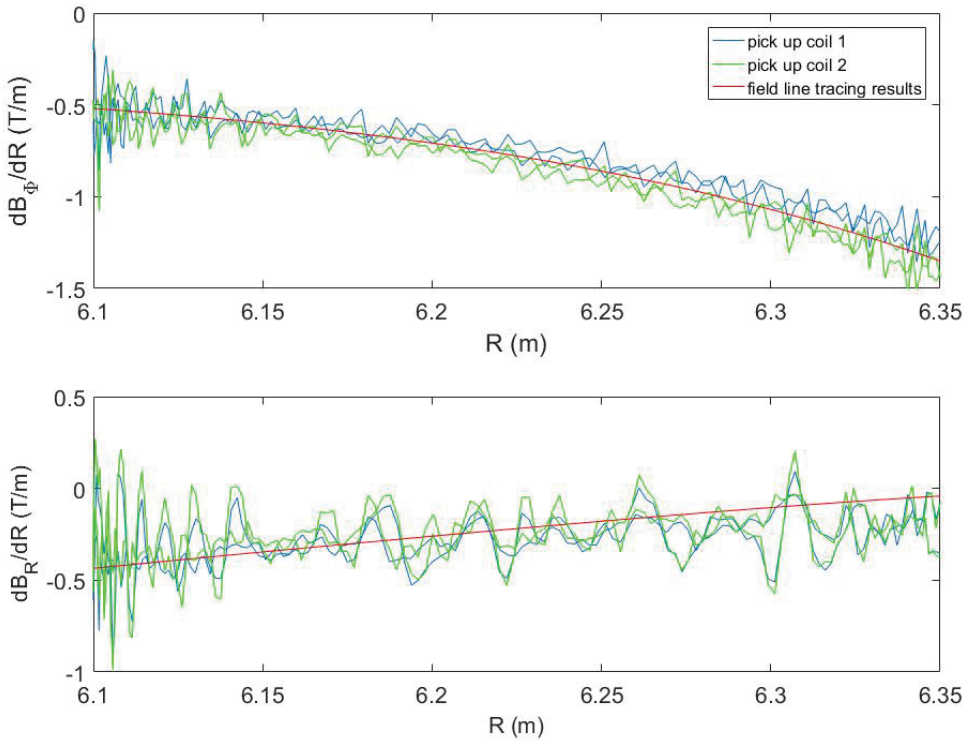

Figure 2.8: Magnetic field gradients in radial direction measured with the two pick up coil arrays in comparison to the calculation from the field line tracing webservice.

2.2.2 Commisioning of the Langmuir and Mach probes

The Langmuir probe is arguably one of the oldest plasma diagnostics [27] and used for the measurement of the electron temperature and density. Langmuir probes are easily employed in a plasma vessel on both limiters and divertors and as a reciprocating probe. The combined probe originally only included a triple Langmuir [34][35] probe and several floating potential pins. This choice was made instead of a swept single or double Langmuir probe, due to ease of calculating the electron temperatures and densities. This is very important for a manipulator measurement, since the decision to plunge deeper into the plasma, to obtain better results, should be made based on the results of the measured profiles and the input of other diagnostics. The manipulator houses a sensor for measuring the temperature to ensure the protection of the overall machine from over heating, the currently used combined probe features such a sensor as well.

Temperature measurements done within the carrier pipe of the manipulator prevent a plunge in case of dangerous temperature levels. This on the contrary is not presently available for the probe head itself, therefore too high temperatures for the manipulator can be detected, but they do not automatically stop the fast movement, in case of the probe overheating.

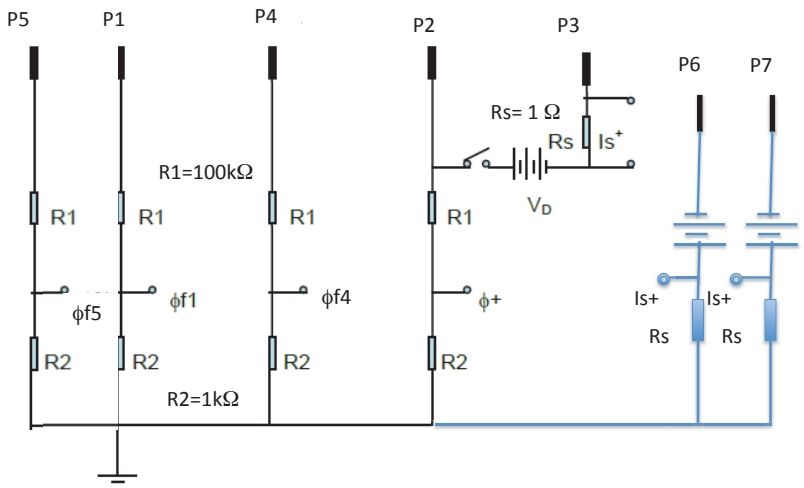

Figure 2.9: Pin setup of the combined probe head.

The system allows recording with a resolution of up to 4 MHz. The electronic system for biasing is based on a template from Greifswald. The centerpiece of the necessary biasing of the probe pins (shown in figure 2.9) is achieved with a supercapacitor module supplied by Maxwell. Four supercapacitors will be installed, for the Langmuir and Mach probes. Three of them are needed, one to supply the biasing voltage for the positive and negatively biased Langmuir pins and one for the up and one for the down stream oriented Mach probe pins. Normally batteries are used for this purpose, but safety requirements precluded this. The capacitor based biasing also has the added merit that the biasing voltage can be varied to up to the nominal voltage. It is also possible to fully discharge the device for safe maintenance and transportation. The only limitation of this setup is the comparably smaller capacity, which necessitates accurate control of the charging between measurements. The aforementioned supercapacitor from Maxwell has a capacity of 6 F, the maximum voltage, which may never be exceeded, is 160 V. To achieve higher biasing voltages multiple capacitors can be used together. The capacitor at an ambient temperature of 25 °C will heat up to 50 °C during a full discharge. The temperature is monitored by a thermo switch.

This capacitor feeds the Langmuir and Mach probe pins with the necessary biasing voltages, as shown in figure 2.9. Figure 2.10 shows the location of Langmuir and mach pins on the top of the combined probe. The pins P1, P4 and P5 are used to measure the floating potential, P2 and P3 the electron and ion current and P6 and P7 the ion currents for the Mach probe. All pins have a length of $l = 2\,\mathrm{mm}$, the pins P1, P4 and P5 have a diameter of $d = 1\,\mathrm{mm}$ and the pins P2 and P3 $d = 2\,\mathrm{mm}$. The pins P6 and P7 used for the Mach probe have the same dimensions

as P1, P4 and P5, but one half is cut extending from the level of the graphite shielding to present a plane and defined surface. The limiter and later the divertor due to its size causes a

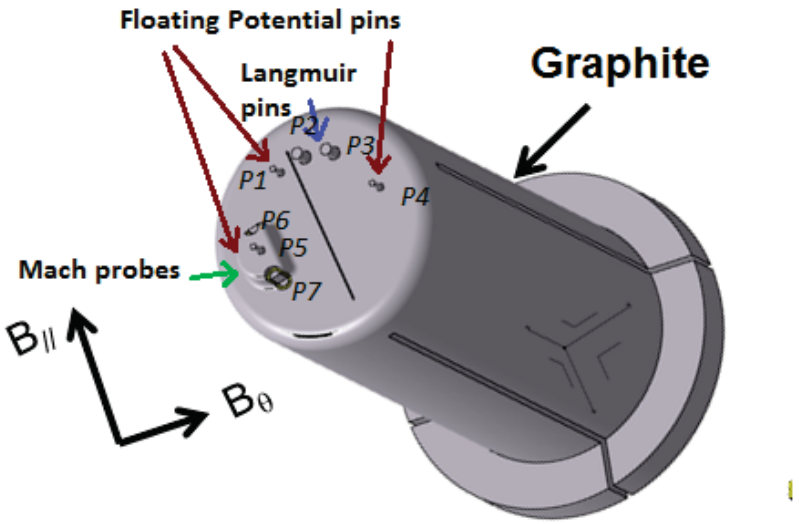

Figure 2.10: Position of the Langmuir and Mach pins on the combined probe.

considerable potential drop and therefore the machine is used as a reference for the measurement with Lanmguir probes. The biasing cards also double for measuring the currents via a shunt resistor as well the potentials. The current measurements have the following transform from current to voltage by using shunt resistors:

$$U_{\mathrm{I}} = I_{\mathrm{probe}} R_{\mathrm{shunt}} V \tag{2.2}$$

With U_{I} as the output voltage, I_{probe} the current from the probe tip, R_{shunt} the shunt resistors of $0.1, 1, 10, 100\,\Omega$ and $V = 10$ as a constant amplification. The potential measurements follow:

$$U_{\mathrm{out}} = U_{\mathrm{probe}} \frac{R}{R_{\mathrm{total}}} V \tag{2.3}$$

With U_{out} as the measured voltage, U_{probe} the voltage at the probe tip, $\frac{R}{R_{\mathrm{total}}} = 100$ and V a selectable amplification. The cards offer for the potential measurement amplification of $10:1, 20:1, 50:1, 100:1$, for the currents selectable resistors for $1:1000, 1:100, 1:10, 1:1, 1:0.1$. This is necessary since the maximum output voltage should not exceed $10\,\mathrm{V}$. The biasing electronics have a frequency limit of up to $300\,\mathrm{kHz}$, which is mostly defined by the measurement amplifiers used. Figure 2.11 shows the measured attenuation and the phase shift during a frequency sweep for the voltage measurement in the settings for the expected $140\,\mathrm{V}$ potential. As expected the phase shift increases linearly with frequency, such that the time delay is constant.

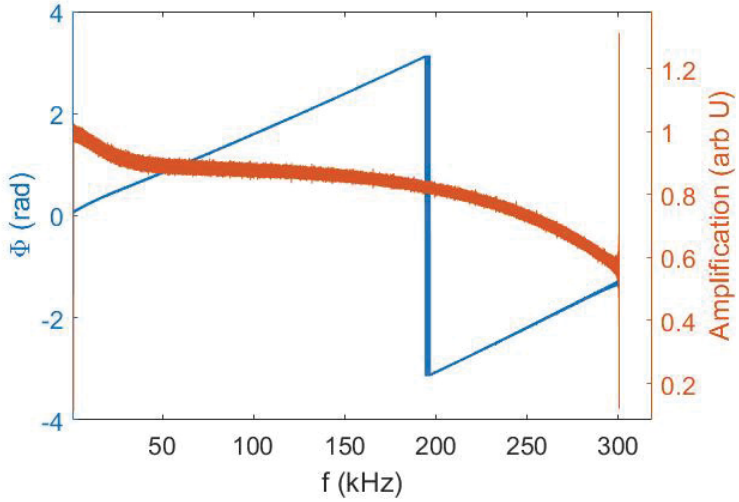

Figure 2.11: Measurement of the phase shift and attenuation during a frequency sweep in the probe electronics.

The amplifiers mostly contribute to the time delay in the measurement of about 20 µs, which indeed is worthwhile to mention since it is one order of magnitude bigger than the measured resolution. The test of the acceleration revealed that the positioning signal also has a delay (see figure 2.5), which comes from the inbuilt filter of the Keyence software. The filter has an averaging function that uses a certain sample length N and with the sampling rate of R, the time delay therefore is:

$$t_{\text{delay}} = N \cdot R \tag{2.4}$$

With $R = 500\,\mu\text{s}$ and $N = 256$ a time delay of 0.128 s is present. In table 2.1 the collected time delays, frequency limits and sampling rates are shown. Moreover the modification of the amplitude is of interest since the amplification can be used to correct measurements in the higher frequency ranges.

Device	Time delay	frequency limit	sampling rate
Langmuir probes	5 µs	300 kHz	1000 MHz
Magnetic coils	5 µs	200 kHz	1000 MHz
Position sensor	0.0681 s		

Table 2.1: Time delay, frequency limit and sampling rate for the diagnostic parts

The Langmuir probe theory of the collection of ions and electrons is based on the assumption that the plasma is in local thermal equilibrium (has a maxwellian distribution). A single Langmuir probe will collect a current based on a sweeping biasing voltage as shown in figure 2.12. The collected current or saturation current for ion is expressed as [34]:

$$I_{\text{sat}} = A_{\text{col}}\, e\, n_{\text{e}}\, c_{\text{s}} \tag{2.5}$$

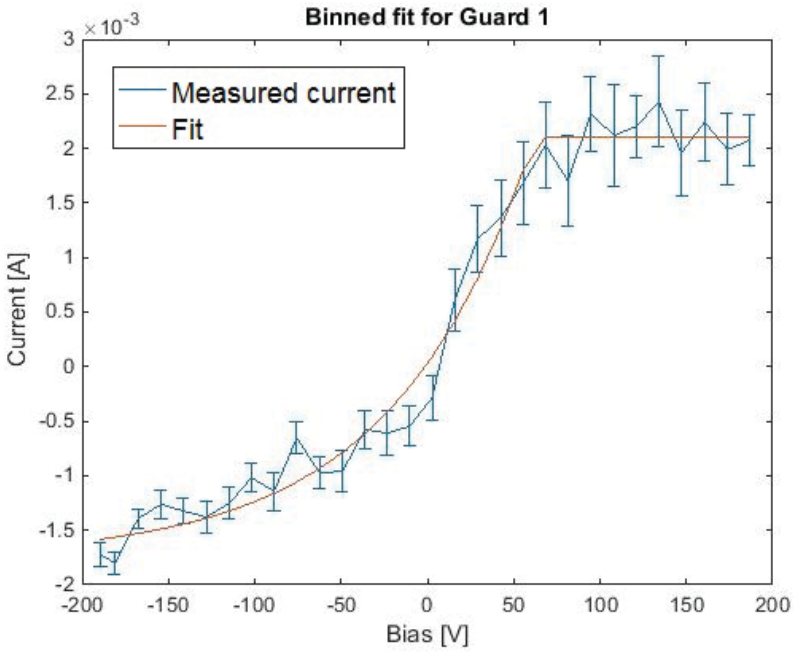

Figure 2.12: $I - U$ curve from the guard ring of the upgraded combined probe head used as a single Langmuir probe.

With A_{col} the effective collection area modified by the plasma environment and c_{s} the ion sound-speed. The current that flows through the respective Langmuir probe pins shown in figure 2.13 is:

$$I_{\text{Langmuir } P2} = I_{+} = I_{0i} + I_{0e} \exp\left(-\frac{eV_{+}}{k_{\mathrm{B}} T_e}\right) \tag{2.6}$$

$$I_{\text{Langmuir } P3} = I_{-} = I_{0i} + I_{0e} \exp\left(-\frac{eV_{-}}{k_{\mathrm{B}} T_e}\right) \tag{2.7}$$

$$I_{\text{Langmuir } P1,P4,P5} = 0 = I_{0i} + I_{0e} \exp\left(-\frac{eV_{\mathrm{f}}}{k_{\mathrm{B}} T_e}\right) \tag{2.8}$$

With I_{0i} the ion saturation current and I_{0e} the electron saturation current. If equation 2.6 is divided by equation 2.7, assuming that $-I_{0i} = I_{0e}$ one gets:

$$-1 = \frac{1 + \exp\left(\frac{-eV_{+}}{k_{\mathrm{B}} T_e}\right)}{1 + \exp\left(-\frac{eV_{-}}{k_{\mathrm{B}} T_e}\right)} \tag{2.9}$$

$$\exp\left(\frac{eV_{+}}{k_{\mathrm{B}} T_e}\right) - 1 = \exp\left(-\frac{e(V_{-} - V_{+})}{k_{\mathrm{B}} T_e}\right) - \exp\left(\frac{eV_{+}}{k_{\mathrm{B}} T_e}\right) \tag{2.10}$$

$$\exp\left(-\frac{e\left(V_{\mathrm{f}} - V_{+}\right)}{k_{\mathrm{B}} T_e}\right) - 1 = \exp\left(-\frac{e(V_{-} - V_{+})}{k_{\mathrm{B}} T_e}\right) - \exp\left(-\frac{e\left(V_{\mathrm{f}} - V_{+}\right)}{k_{\mathrm{B}} T_e}\right) \tag{2.11}$$

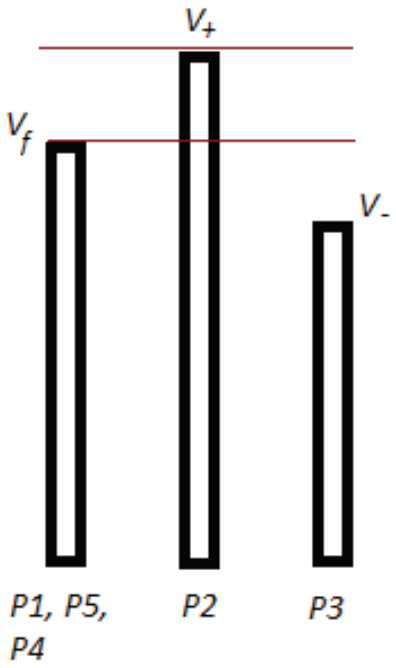

Figure 2.13: Sketch of the potentials of the triple probe pins.

with:

$$\exp\left(\frac{-eV_\mathrm{f}}{k_{k_\mathrm{B}}T_e}\right) = 1 \tag{2.12}$$

$$2\,\exp\left(-\frac{e(V_\mathrm{f}-V_+)}{k_\mathrm{B}T_e}\right) = \exp\left(-\frac{e(V_- - V_+)}{k_\mathrm{B}T_e}\right) + 1 \tag{2.13}$$

The term $\exp\left(-\frac{e(V_- - V_+)}{k_\mathrm{B}T_e}\right)$ is normaly negligible since $e(V_- - V_+) \gg k_\mathrm{BT}T_e$. We arrive now at the relation for the electron temperature:

$$k_\mathrm{B}T_e = \frac{e(V_+ - V_f)}{\ln 2} \tag{2.14}$$

The calculation of the electron density also depends on sufficient knowledge of the ion species and their charge state:

$$n_\mathrm{e} = \frac{I_-}{0.49\,A_\mathrm{eff}\sqrt{\frac{T_\mathrm{i}+Z\,T_\mathrm{e}}{m_\mathrm{i}}}} \tag{2.15}$$

With A_eff as the effective collection area and I as the ion saturation current from pin $I_{\mathrm{Langmuir}\,P3}$. Reference [38] suggests that an overestimation of the collected currents can cause an error in the electron temperature calculation.

An issue, that should be mentioned for the interpretation of the measurements, is a voltage rise, found on the positively biased pin. One could assume, that even with grounding issues, the

difference between the plasma potential (pin 4) and floating potential (average between pin 1 and pin 4) are reasonably correct. In figure 2.14 one can see that in the parking position a ramping of the voltage with the plasma start up is present on the floating and plasma potential pins. This phenomenon is connected to the density and the biasing voltage. The floating potential pins experience much lower amplitudes but they are still visible. In figure 2.15 one can see, during

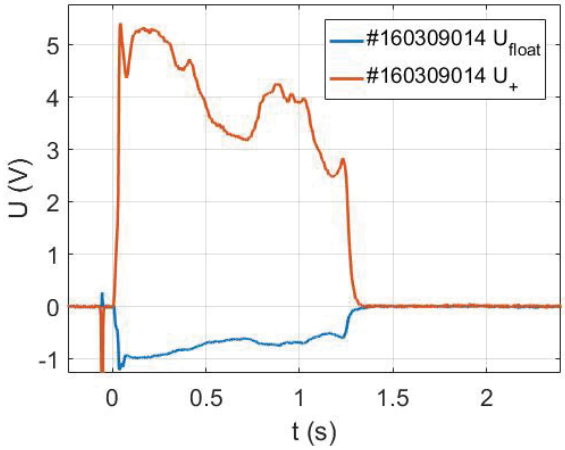

Figure 2.14: Time trace of the floating potential U_{float} and and the electron collection pin voltage U_+ in parking position.

a plunge, that in an intermediate position of 8 cm the problem of the ramping voltage is still present. In this case no biasing was applied which results in a lower but still visible amplitude. When pulling back the manipulator one can see hat the voltage first drops and then again unnaturally increases, only to drop again with the termination of the discharge. For a plunge it is

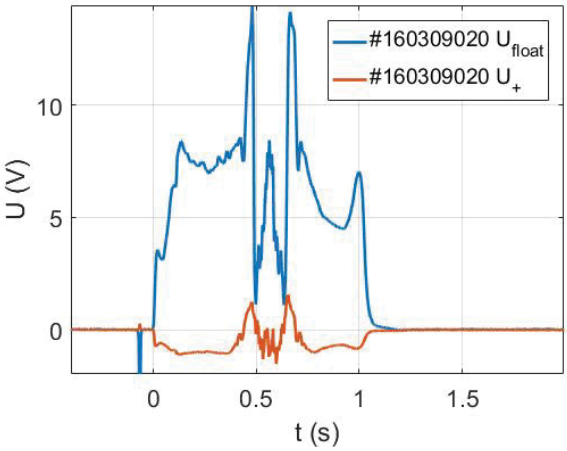

Figure 2.15: Time trace of the floating potential U_{float} and and the electron collection pin voltage U_+ during a plunge.

easily visible that before the plunge the ramping is present (see figure 2.15). With the plasma

startup the voltage increases, the small step also is present in the line integrated density signals at 0.1 ms. With the plunge at 0.4 ms the measured voltage shortly after drops to zero, to further yield a reasonable profile. It turns out that the circuit for the measurements can only measure

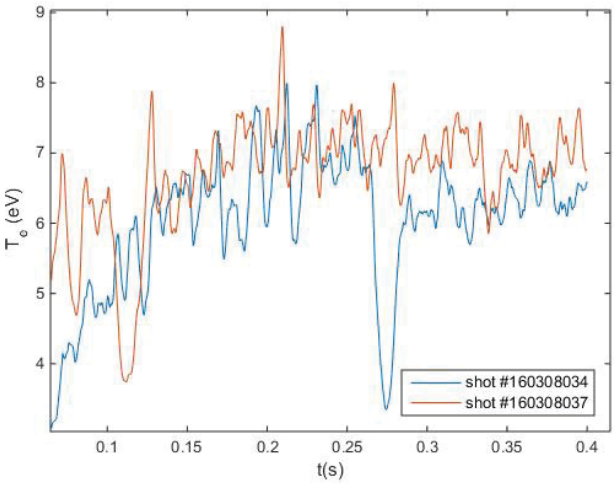

Figure 2.16: Temperature time trace with nitrogen puffing at $t = 0.1\,\mathrm{s}$ and $t = 0.25\,\mathrm{s}$.

reliably in the presence of plasma as a conductor. Without it, the biasing is always measured instead. One way to remedy this, is to measure directly the difference of the positive and the floating pin. This would avoid trouble during the analysis, but also reduce the number of floating potential pins for the turbulence measurement.

The manipulator also allows stationary measurements at a fixed position. Time traces of such an experiment are shown in figure 2.16. Discharge program 20160308.034 and 20160308.037 were conducted as part of a nitrogen puffing experiment with the position of the probe at $R = 6.09\,\mathrm{m}$. At $t = 0.1\,\mathrm{s}$ and $t = 0.25\,\mathrm{s}$ the puffing of nitrogen is visible as a significant drop in the temperature for the two respective time traces. The combined probe was used as an auxiliary diagnostic to confirm the cooling effects in the edge by puffing nitrogen (see [36] and [37]).

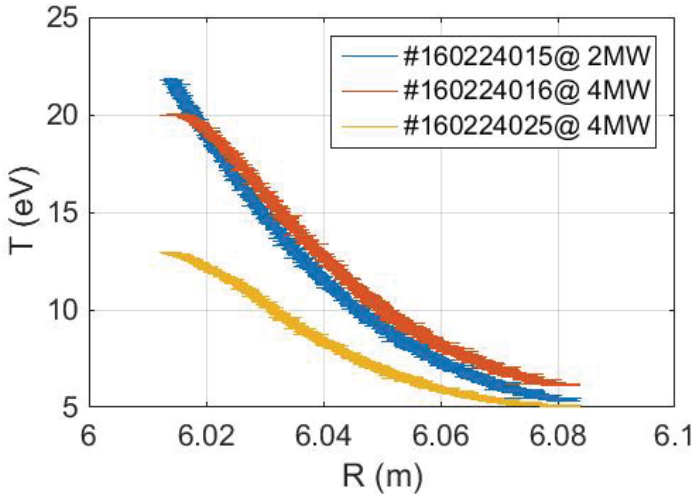

Figure 2.17: T_e profiles in standard configuration before proper wallconditioning was established.

Part of the first week of manipulator operation was a trim coil experiment, that was supposed to ergodize the plasma edge and modify the heat loads on the limiter in module four. One would expect that, in turn the electron temperature T_e profiles would flatten. In figure 2.17 the electron temperature profiles are shown from the trim coil scan. The analysis of these discharges is difficult since for similar heating schemes one can see that the temperatures decrease not with increasing perturbation but with increasing discharge number.
This is due to a deterioration of the machine condition from outgassing of the wall components. The first J-configuration discharge with much lower heating power can sustain similar or even higher edge temperature profiles.

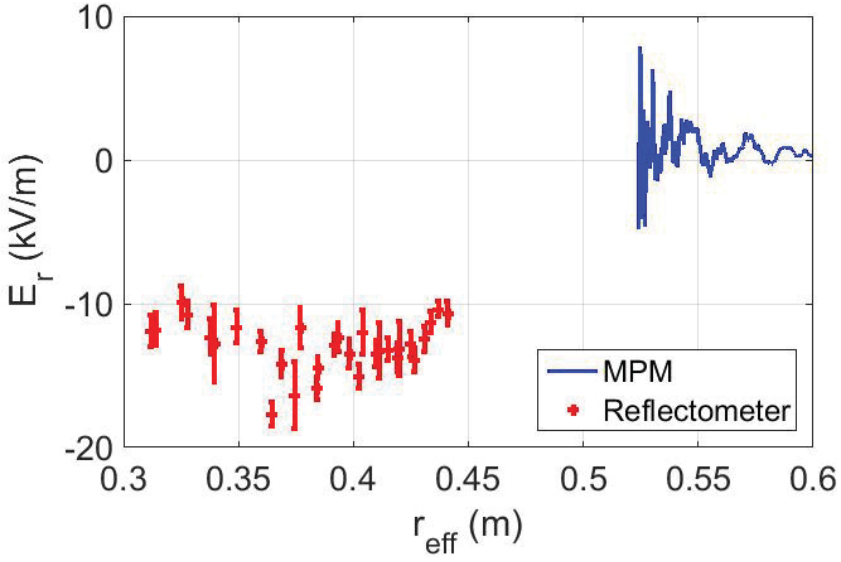

Figure 2.18: Electric field measured with the combined probe and the correlation reflectometry for the J and high iota configuration.

2.2.3 Measurement of the electric field E_r

The electric field can be caculated from the measured floating potential and the electron temperature. The electric field is calculated using:

$$E_\mathrm{r} = -\frac{\partial(U_\mathrm{float} + 2.8 \cdot T_\mathrm{e})}{\partial r} = -\left(\frac{U_\mathrm{float-up} - U_\mathrm{float-down}}{\Delta R} + 2.8\frac{T_\mathrm{e}(r+\Delta r) - T_\mathrm{e}(r)}{\Delta r}\right). \tag{2.16}$$

It is necessary here, to take the electron temperature $T_\mathrm{e}(r)$ from the profile, due to the lack of two independent temperature measurements in different radial positions. The filtering of the data is done using a low pass filter with a cut-off frequency of 50 Hz. The values of the electric field from the combined probe close to its final position are susceptible to errors from the position measurement in the $1/\Delta r$ term, since the probe is close to a standstill.

The measurements of the electric field, in the mid-plane, can be compared to the results from the reflectometry [39], shown in figure 2.18. The sign of the electric field is expected to change from positive to negative while crossing the last closed flux surface at $r_\mathrm{eff}/a = 1$. The data from the Langmuir probes yield mostly positive values close to the last closed flux surface. This is a further hint, that the last closed flux surface is located further inwards relative to the probe position. The aforementioned relatively low values from the density and temperature measurements, further support this assumption. The second operational phase will see plunges reaching to densities of at least $0.6 \times 10^{19}\,\mathrm{m}^{-3}$ which are necessary to obtain a matching range of both reflectometry and combined probe. This issue is revisited for the second campaign in 3.2.3 with a better matching range, since the previously mentioned requirements of plunge depth and plasma

density are fulfilled.

Note should be taken, that the effective radius was calculated using the machine coordinates from the probe position and mapped onto flux surfaces. This procedure is difficult in the edge region close to the island, the calculations using VMEC [40] had to be extended to cover the whole island region.

2.2.4 Flow measurements with the Mach probe

The Mach probe is used to measure the flow velocity and it operates like a Langmuir probe in fixed ion saturation mode. The Mach number as a measure of the flow velocity can be extracted using the fraction of the up and downstream ion saturation currents on a probe:

$$M = \ln\left(\frac{J_{\mathrm{up}}}{J_{\mathrm{down}}}\right)/K \tag{2.17}$$

With K being a calibration factor, which value depends on the choice of the model depending on magnetic field, the collisions of charged particles and neutrals, the viscosity, the ion temperature etc [28]. In the case of W7-X it is expected that the strong magnetic fields present in the machine will dominate the effects for the collection of ions with the Langmuir pins and therefore $K = 2.3 - 2.5$ is chosen. Only the measurements of the second operational phase yielded good measurements of the Mach number, due to possible leak currents caused by the ceramic insulator used in the first combined probe. It is possible to correct the Mach probe measurements with the use of the electron densitiy profile, since plasma blobs are able to distort the flow profiles [41].

2.3 Upgrading the combined probe

The upgraded combined probe (see figure 2.19 and 4.2) is an evolution of the previous, it still contains several floating potential pins for turbulence measurements, a Mach probe, a triple Langmuir probe and pick-up coils. In addition, it houses an ion sensitive probe, a material sample, a compensation coil array and a gas-puffing outlet.

One big issue is the lack of a robust method to compare and validate the density and temperature profile with the triple probe measurements. Most of the other diagnostics present at W7-X do not possess the same spatial resolution at the plasma edge and therefore make it difficult to compare and to ascertain the validity of the triple probe. This might also solve the question of the voltage rise during the plasma operation. One way to achieve this, is to use one of the floating potential pins as a swept single probe, to obtain density and temperature profiles at a lower temporal resolution. The effort is minimal as only a current measurement from one of the modules and a sine voltage source is necessary. Apart from that the pin could be used in normal operation for most of the time. Another big change was the use of a boron nitride cover, it helped

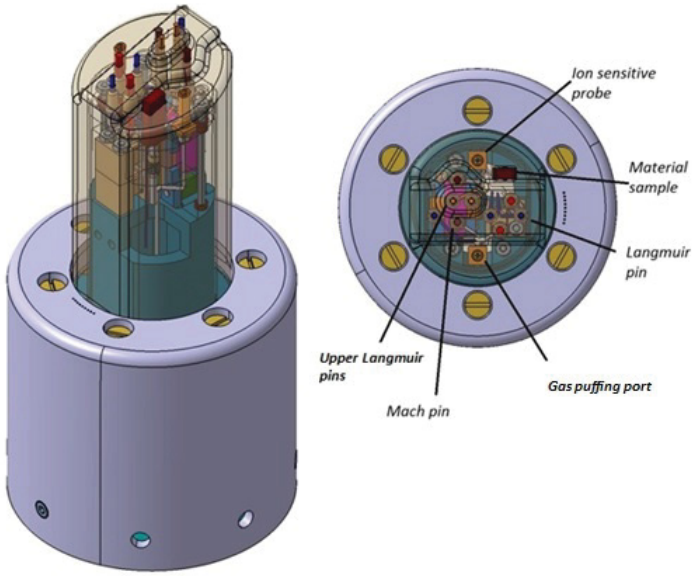

Figure 2.19: Sketch of the upgraded combined probe,with material sample holder, Langmuir pins, Mach probe, Ion sensitive probe, gaspuffing port and magnetic coils.

to prevent the previously suspected arcing between the conducting cover and the probe tips. A warning should be placed here concerning the issue of arcing. It is possible that outgassing is even more severe with boron nitride, which can exacerbate the problem of arcing within the probe heads and damage internal cabling, that is comparably unprotected. As outgassing is after few plunges almost nonexistent, biasing should only be applied after a few "conditioning" plunges.

The upgraded combined probe had a sample holder on the front facing, that allowed exposi-

tion of material sample in the plasmas of W7-X. This by itself is nothing new or special, the real feature of this setup is the exposure under well defined conditions, since the electron temperature, density and ion temperature are well defined, even the sample temperature is recorded with a thermo-couple. In total four Tungsten samples were exposed, they were changed after each week of measurement when repairs were undertaken on the diagnostic. Two quantities are of interest for material researchers that can easily be obtained from the probe data. One is the "history" so to say of the sample, which is the time trace of the heat flux. This allows to check if any spikes or events for that matter could have damaged the Tungsten surface. The other is the integrated heat flux on the sample.

One complication of the analysis of the probe samples and the probe cover is the handling during the changing of the probes. The manipulator requires that the exchanges chamber is under atmospheric conditions for an exchange of the probe head, while the chamber can be flooded with nitrogen, it is still unavoidable that the probe and the material of interest are exposed to non ultra high vacuum conditions. This makes for the currents samples at least an analysis for the hydrogen deposition impossible. The first inspection showed that the expected coloration appears, if carbon is implanted onto surface. Also cracks and small craters are visible on the sample. Further analysis will be carried out using laser-induced breakdown spectroscopy (LIBS) and Time-of-flight elastic recoil detection analysis (ToF-ERDA) [44].

2.3.1 The Ion sensitive probe

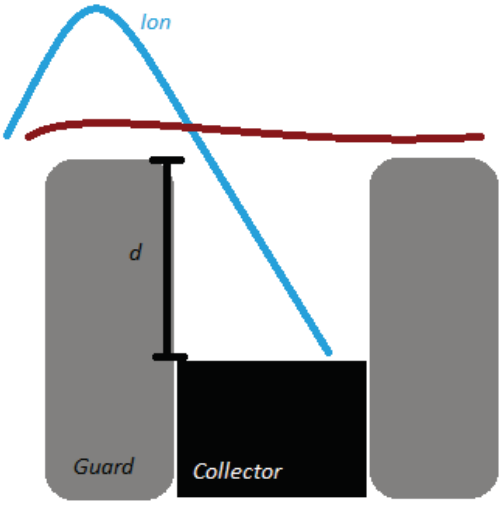

Figure 2.20: Sketch of the ion sensitve probe(taken from [45]).

The ion sensitive probe is envisioned as a diagnostic tool to measure the ion temperature in the plasma edge much like the Langmuir probe measures the electron temperature. The most simle assumption here is that both species have the same temperatures, but modelling and experimental evidence suggests, that for certain conditions in the ECRH (Electron Cyclotron Resonance Heating) heated plasmas, the ion temperature tends to be much lower in the plasma core and considerably higher in the plasma edge. If mostly electrons are directly heated, like in the plasma of OP. 1.1 and 1.2a at W7-X, the Coulomb energy transfer from electrons to ions is the most important mechanism to note. For the experiments at W7-X the dependency of the energy transfer on the electron density is the defining quantity for the electron to ion temperature ratio [42]. The ion sensitive probe was first presented by I. Katsumata in 1966 [43]. It uses the huge difference of the Lamor radii of electrons and ions to preferentially collect the latter in a Langmuir like setup. As shown in figure 2.20 the probe consists of of hollow cylinder used as a guard ring and an inner pin slightly recessed inside. Assuming a Maxwellian distribution one can infer the ion temperature from the $I-U$ curve of the inner pin:

$$I(V) = \begin{cases} I_0 & V < V_p \\ I_0 \exp\left(\frac{(V-V_p)Z}{k_b T_i}\right) & V > V_p \end{cases} \tag{2.18}$$

It was noted, that this diagnostic while having an admirably simple setup, is not without flaws [45]. Too large incidence angles or a space charge limited regime can make the analysis of the ion sensitive probe impossible. At W7-X the incidence angle can change depending on the configuration along the movement of the manipulator, the bigger obstacle though are capacity effects due to the long cables connecting the probe head with the biasing. The guard of the ion sensitive probe can be used as a single Langmuir probe which allows a comparison with the temperatures measured with the triple Langmuir probe, but due to the difficult geometry a

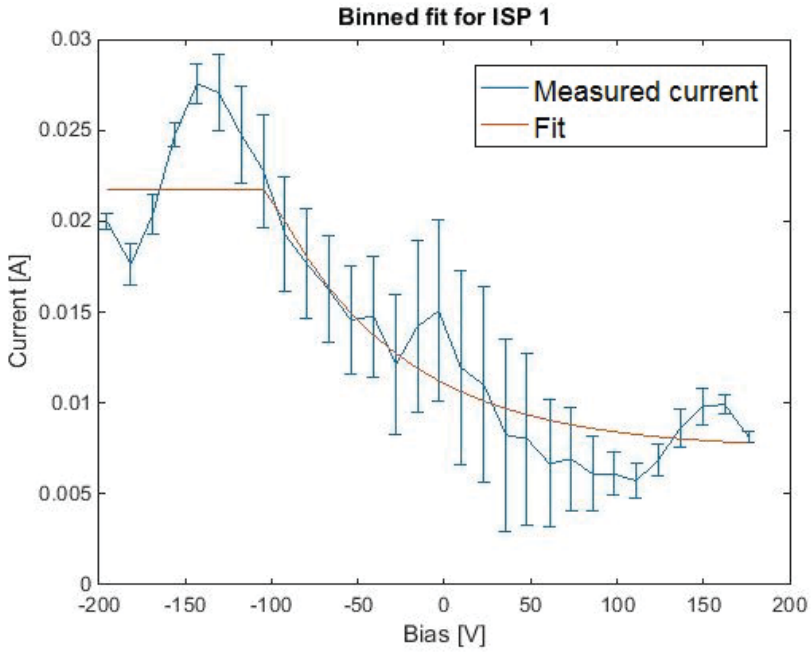

Figure 2.21: $I - U$ curve from the ion collection pin of the upgraded combined probe head recessed in the guard ring.

calculation of the electron density is considerably more difficult. In figure 2.21 an $I-U$ curve from the ion sensitive probe of the upgraded combined probe is shown. The setup of the ion sensitive is still in need of improvement concerning the recess distance and its placement in relation to the probe cover to optimize the ion flux and thus also the collection current. Furthermore it was observed that swept signal at frequencies in the low kHz range incur considerable capacity effects that plague precise measurements.

2.4 Calibration of the manipulator position

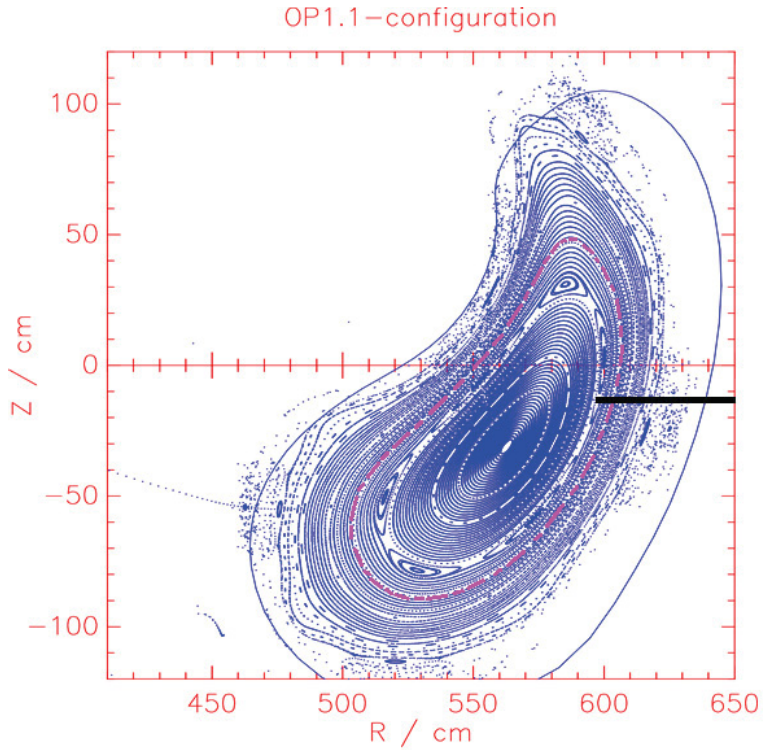

Figure 2.22: Poincaré plot of the W7-X at the toroidal position of the manipulator.

The fieldline tracing code was used to identify the plasma position and to view the island configuration [46]. It can display both limiter an divertor configuration, in figure 2.22 the limiter configuration is shown. In machine coordinates the starting position of the manipulator is:

$$x_0 = -5877.7962\,\mathrm{mm}$$

$$y_0 = -2225.7320\,\mathrm{mm}$$

$$z_0 = -159.1841\,\mathrm{mm}$$

for a plunge of 350 mm the final position is:

$$x_f = -5552.5411\,\mathrm{mm}$$

$$y_f = -2096.4882\,\mathrm{mm}$$

$$z_f = -159.1841\,\mathrm{mm}$$

The x and y coordinates can be used to calculate the radial position using $r = \sqrt{x^2 + y^2}$:

$$r_0 = 6.2841\,\mathrm{m}$$

$$r_f = 5.9345\,\mathrm{m}$$

The current setup is set for a plunge of 300 mm, the final radial position is then:

$$r_f = 5.9845\,\mathrm{m}$$

The reference point for this is the floating potential pin $P5$ which marks the furthest point of the combined probe. With the plasma edge at about $r_{plasmaedge} = 6.19\,\mathrm{m}$, the plunge in the plasma is about 20 cm (2.22). One has to add here that the last closed flux surface is located further inwards as the limiter cuts off the outermost islands in OP. 1.1. The heat flux calculation to test the possible heat loads on the combined probe were carried out to prevent catastrophic damage to the probe[47]. Judging by the calculations in figure 2.23 the probe should be safe, since for a

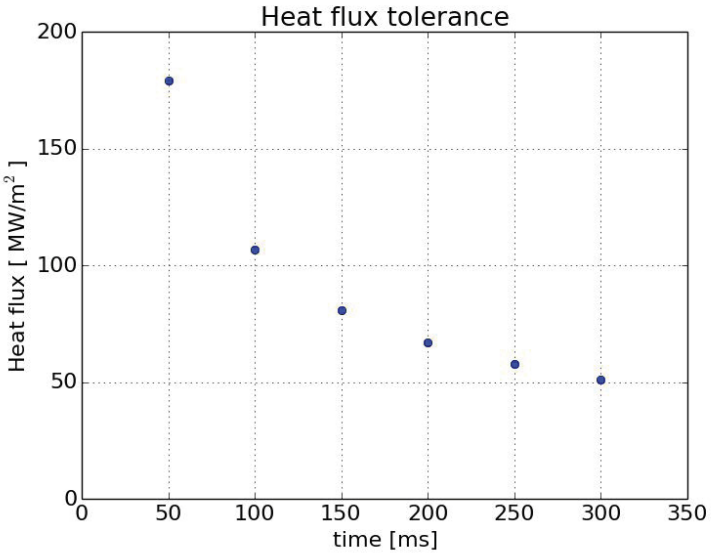

Figure 2.23: Calculated tolerable heat flux allowed for a different duration of the plunge.

heat flux of about 120 $\frac{\mathrm{MW}}{\mathrm{m}^2}$, about 90 ms are considered save. In total the probe head will remain not for much longer than that totally in the plasma. Some data sets show, that while 29 cm are set as a plunge depth within the manipulator controls, only about 27 cm are actualy achieved. This has to do with the Simatic system trying to reach a given position with a set velocity and acceleration and trying to accommodate all these three parameters on the fly. For each set of velocities and accelerations a correct compensation for the plunge depth has to be found.

It is very interesting to know the position of the last closed flux surface from the modelling point of view, as the physics greatly change from the scrape off layer to beyond the last closed flux surface. This is especially important concerning the protection of the probes against heat loads that might damage the probe if plunged too deep. The connection lengths for the J-configuration (standard limiter), iota 5 and iota 13 limiter configuration indicate that the last closed surface is in the plane of the manipulator to be at $R = 6.03, 6.01\,\mathrm{m}$ and $R = 6\,\mathrm{m}$ (see figure 3.3). A complication encountered during the first campaign was that the position of the manipulator was suspected to be incorrect. The measurements yielded rather low temperatures and densities.

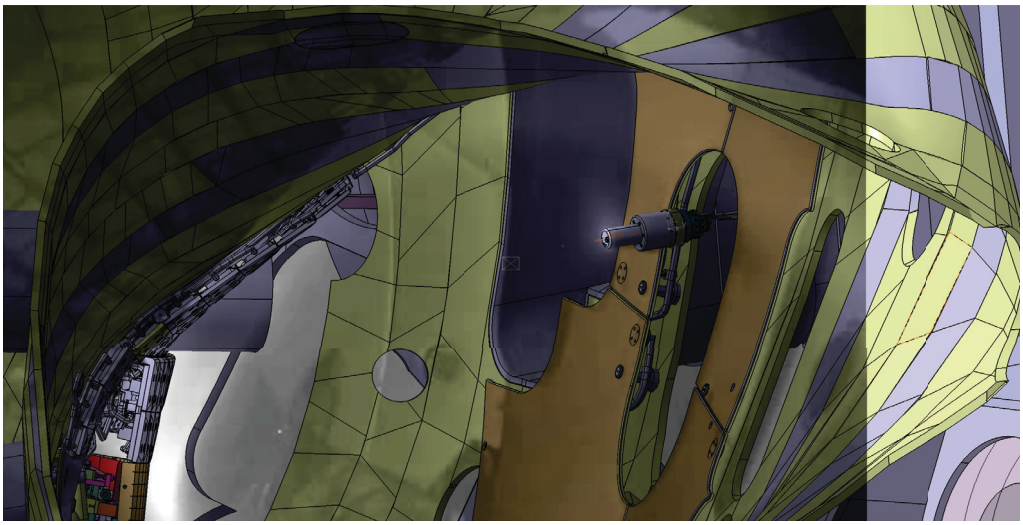

Figure 2.24: Overlay of the CAD drawing and the image from the fast camera with the 6 cm shift in the final position.

Also the radial electric field did not display a change of the sign. This apparent mismatch of the measured plasma conditions and the position recorded lead to the conclusion that position might have an offset. The fast camera measurements were used to compare the actual with the assumed position. In figure 2.24 one can see that there is actually an outward shift of 6 cm. Also the magnetic measurement, using a comparison of the calculated and measured gradients, shown in figure 2.8 supports this finding (here the position was shifted by the offset already). It is therefore clear that the position of the manipulator had an offset and the last closed flux surface was not reached in any discharge in the first campaign.

In the second operational campaign, the position was confirmed again using the measurements of the pick up coils in the probe. Figure 2.25 shows the comparison of the calculated vertical magnetic field B_z and measurements done in vacuum and plasma. Here no off-set was necessary.

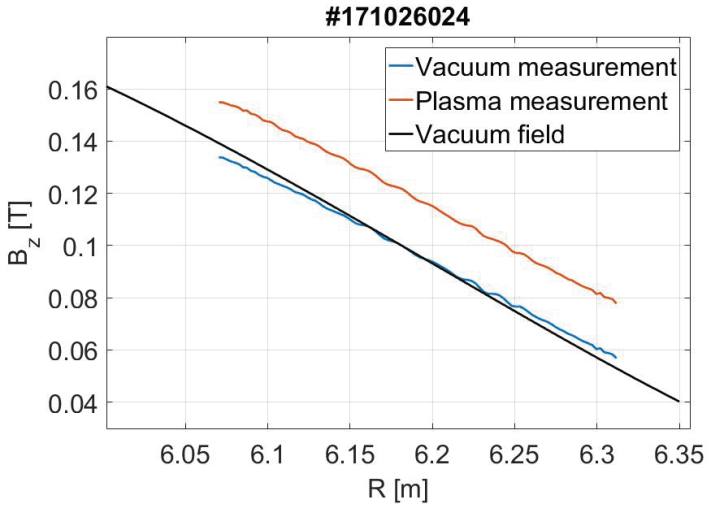

Figure 2.25: Comparison of the caculated vertical magnetic field and the measurements done in vacuum and with plasma, for the second operational campaign.

Chapter 3

Topology effects on the edge plasma

This chapter describes the measurements in the first operational campaign Op 1.1 [48][49] in the limiter configuration and for the first part of the second operational campaign Op 1.2 with a divertor configuration. For the Op 1.1 the first iteration of the combined probe was used and in the Op 1.2a an upgraded version was utilized. The measurements in the limiter plasmas showed only for a very specific configuration an edge island remnant, which was visible in the temperature profiles. Also a comparison with the infrared cameras observing the limiters was possible. This comparison was made assuming a partial toroidal symmetry and a rather simple edge topology in the standard limiter configuration.

The second operational campaign featured a divertor configuration which allowed for considerably improved plasma performances in regard to densities and discharge durations. These longer discharges and higher densities gave rise to beta effects and also evolving toroidal currents. The more complex topology also caused a considerable change between the up-stream profiles measured with the manipulator probes and the down-stream measurements with the infrared cameras and the divertor Langmuir probes.

3.1 Topology effects in limiter plasmas

The first campaign of measurements with the manipulator started after the commissioning in February 2016. The results of this campaign have been published in [50][51] and used in this chapter. The conversion for the position measurement was:

$$R(\,\mathrm{m}) = -U_{\mathrm{position}} \cdot 0.05463\,\frac{\mathrm{m}}{\mathrm{V}} + 6.2851\,\mathrm{m} + 0.06\,\mathrm{m} \tag{3.1}$$

For the second week the conversion was set to:

$$R(\,\mathrm{m}) = -U_{\mathrm{position}} \cdot 0.05\,\frac{\mathrm{m}}{\mathrm{V}} + 6.2851\,\mathrm{m} + 0.06\,\mathrm{m} \tag{3.2}$$

This conversion already takes the $+0.06\,\frac{\mathrm{m}}{\mathrm{V}}$ shift, due to the positioning error, into account. In addition, the moving average filter, that led to a time delay of 0.0681 s, was turned off. The first day of measurements for the combined probe was Tuesday the 24.02. The probe was inserted into

the plasma, while slowly moving the probe head further into the plasma with each discharge. It was found that a maximum plunge position was 29 cm, at 30 cm a huge arc appeared and the fuse of the up stream Mach probe broke. The damage in figure 3.1 shows that the arcing on pin 7 left a visible but inconsequential damage. It was suspected the ceramic isolator was coated with either tungsten or carbon and thus leading to a low but for the purposes of the experiment considerable conductivity. But even though coating is visible, it has no direct effect on the conductivity in atmospheric or vacuum conditions. But even though coating is visible, it

Figure 3.1: Superficial damage on pin 7 after the arcing.

has no direct effect on the conductivity in atmospheric or vacuum conditions.

An ongoing discussion for users of reciprocating probes is the sticking reputation to disturb the plasma, which is true to the point that any body introduced into a hot plasma will have an effect. Indeed for some discharges it was quite evident that the plasma was disturbed, this was visible using the fast cameras and also shown in the filter scope measurements [52]. The cause of the plasma perturbation though is caused by a too deep plunge, in this case the problem can be avoided easily.

The density calculation from ion saturation current of the Langmuir probe depends on the calculation of the ion sound speed $C_\mathrm{s} = \sqrt{\frac{Z_\mathrm{eff}T_\mathrm{e}+T_\mathrm{i}}{M}}$ with M as the total mass of the ion species present. For a correct calculation of the density it is useful to know the ion temperature T_i, which was not possible to measure with the OP. 1.1 probe setup, it is therefore practical and necessary to assume that ion and electron temperatures are the same. In addition, information on the impurities is useful, since these ion species will introduce great changes to the overall

mass and effective charge. Carbon will be one of the main impurities and its content in the edge can be measured with visible spectrometry [52]. Other impurities are also present, but harder to detect since most of the diagnostics like HEXOS are focused on the core plasma, which would make an assumption on the impurity migration necessary.

The effective charge can be estimated to be at most between $Z = 2 - 4$ since the measured temperatures sufficient to reach the ionization energies for carbon. This indicates, that the plasma considered here is not a pure hydrogen plasma. The main impurity source, in this case carbon, ist originating from the limiters. Given the above effective charge a maximum of about 10 % carbon content is a good estimate. No precise measurements on the impurity concentration and effective charge are available for the edge and the above mentioned conditions serve as another possible source of error in the density measurements. The errors presented here were calculated by using the weighted standard deviation of the data. The density has a comparably large error due to the small currents measured via a shunt resistor.

There is a huge difference in gradient scale length $L \approx 2\,\mathrm{m}$ of the magnetic field and the Larmor radius of both electrons $r_{\mathrm{Le}} \approx 0.44 \cdot 10^{-5}\,\mathrm{m}$ and ions $r_{\mathrm{Li}} \approx 0.19 \cdot 10^{-3}\,\mathrm{m}$, therefore the sheath expansion coefficient 0.49 for plasmas with strong magnetic fields [53] is recommended. The measurements of the electron temperature were compared to the limiter Langmuir probes [36] and other diagnostics like the helium, beam. The manipulator mounted combined probe is measuring up-stream values of up to a maximum of 25 eV. The limiter Langmuir probes are reported to yield downstream values of between 15 eV and 50 eV [54], the Helium beam results from the OP. 1.1 did not have sufficient quality that allowed a comparison. Reference [54] also shows that the array of limiter Langmuir probes, that are more close to the last closed flux surface and thereby yield higher temperatures, had a very similar exponential decay compared to the profiles measured with the combined probe in the mid-plane.

3.1.1 Iota dependence of the edge equilibrium profiles

The iota configuration was changed by tuning the planar coil currents according to table 3.1. The measurements of all presented discharges for the iota scan were performed at the same ECRH heating of 2 MW. The higher iota configurations experience an inwards shift of the 5/6 island chain located inside the last closed flux surface, while the 5/5 island moves closer towards the last closed flux surface from the scrape off layer, the manipulator plunge depth was adjusted accordingly.

The 5/6 island chain can not be measured directly with the probe. The accessible 5/5 island chain is supposed to be cut off by the limiter. The machine performance had considerably improved with the conditioning, as opposed to the previously shown trim coils experiment, such that the line averaged densities were consistent throughout the day.

Table 3.1: Coil configurations considered for the iota scan, with the position of the last closed flux surface (LCFS) in the path of the manipulator, obtained from the field line tracing and central iota value (taken from [50]).

Scenario#	**Index**	**Position of LCFS (m)**	**iota**
20160309.013	1	6.03	0.789
20160309.017	5	6.025	0.793
20160309.020	7	6.016	0.797
20160309.025	9	6.01	0.805
20160309.028	11	6.004	0.81
20160309.032	13	6.001	0.814

The OP. 1.1 limiter configurations listed in table 3.1 were considered. A web service is offered by the Max-Planck-Institut für Plasmaphysik in Greifswald based on a field line tracing tool [46], this tool traces the field lines for given input currents and machine configurations by integrating the equation:

$$\frac{\mathrm{d}\vec{r}(s)}{\mathrm{d}s} = \frac{\vec{B}}{|\vec{B}|} \tag{3.3}$$

The field line tracing tool was used to identify the confined region, by assuming that this region is marked by consistently exceeding a connection length of 300 m as shown in figure 3.3.

It is visible in the density and temperature profiles (see figure 3.2), that the magnetic axis and therefore also the last closed flux surface (LCFS) was shifted. Since the machine conditions had improved and the gradual change was visible with the tuning of the coils currents, the change of the plasma profiles should not be an effect of steady accumulation of impurities in the edge, which would cool the plasma, as observed before in the trim coil scan. The lack of a distinct electron density rise, from discharge to discharge, supports this assumption. It can be therefore assumed, that the change of the profiles (the inwards shift) is caused by a change of the magnetic

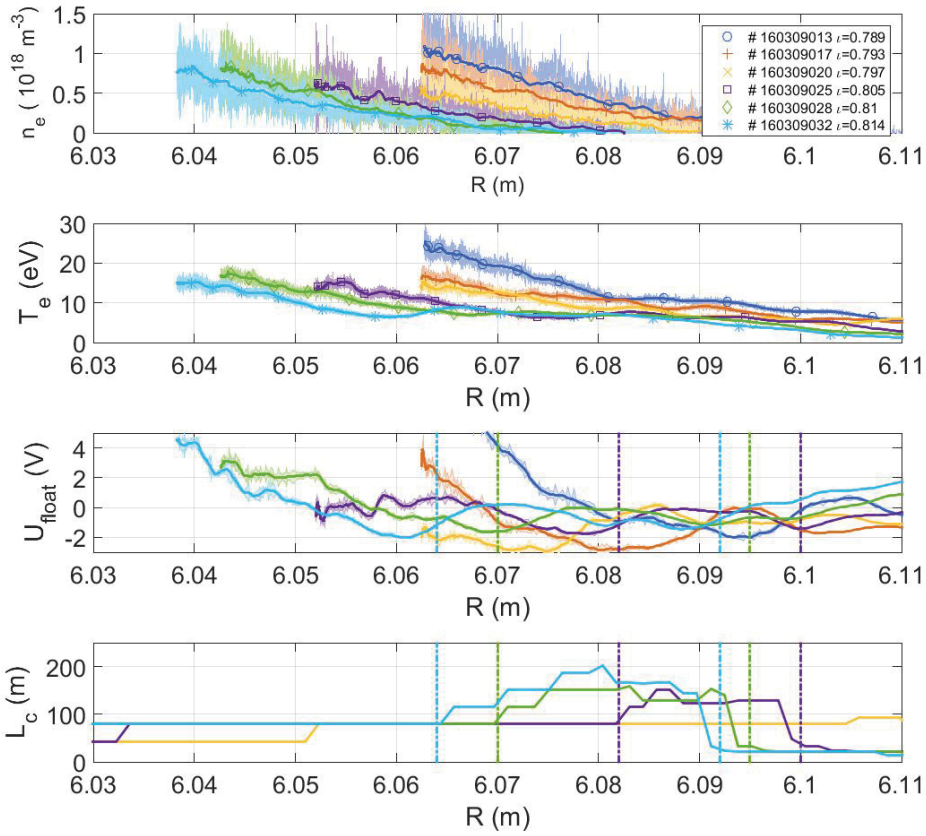

Figure 3.2: Density, temperature, plasma potential and connection length profiles of the iota scan. The vertical lines in the plasma potential and connection length plot profile indicate the location of the high connection length areas in front of the last closed flux surface (taken from [50]).

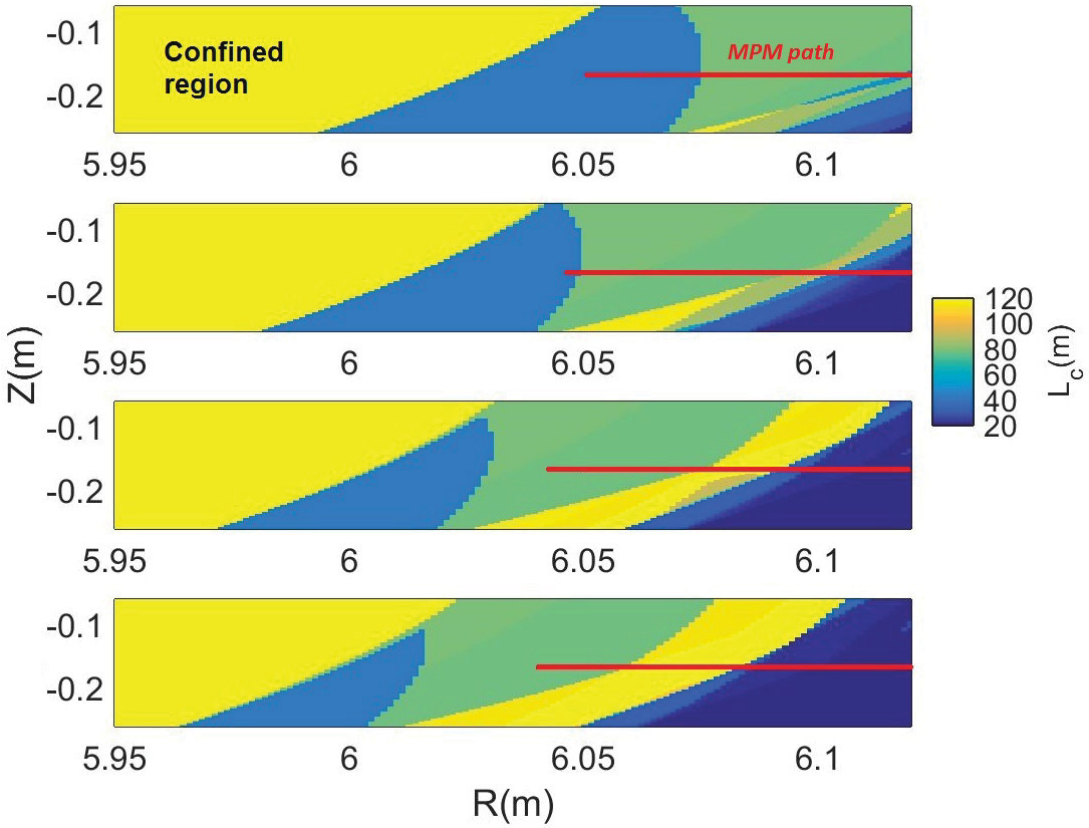

Figure 3.3: Connection length calculated from top to bottom for the iota scan, J configuration index 1, index 7 configuration, index 9 configuration, index 13 configuration, the red line indicates the path of the manipulator.

topology, as intended with the tuning of the coil currents.

Thus the measured profiles can be compared to the results of the field line tracing results, which calculated the connection length along the path of the combined probe. The connection lengths for four steps of the iota scan are shown in figure 3.3, they indicate a similar shift of the profiles. The 2D plots of the magnetic topology in a toroidal cross-section for the J-configuration index 1, index 7, index 9 and index 13 at the position of the manipulator show also a strong change of the connection length in the plasma edge. The connection length calculations show that with increasing with higher planar coil currents and iota, a region of high connection appears a few cm in front of the last closed flux surface. This area can be interpreted as a remnant of the 5/5 island, which was cut off by the limiter. In figure 3.3 one can see with each successive configuration, that the "island" or rather island remnant is increasing in size (indicated by the high connection length) in front of the actual last closed surface. This is due to the 5/5 islands moving away from limiters.

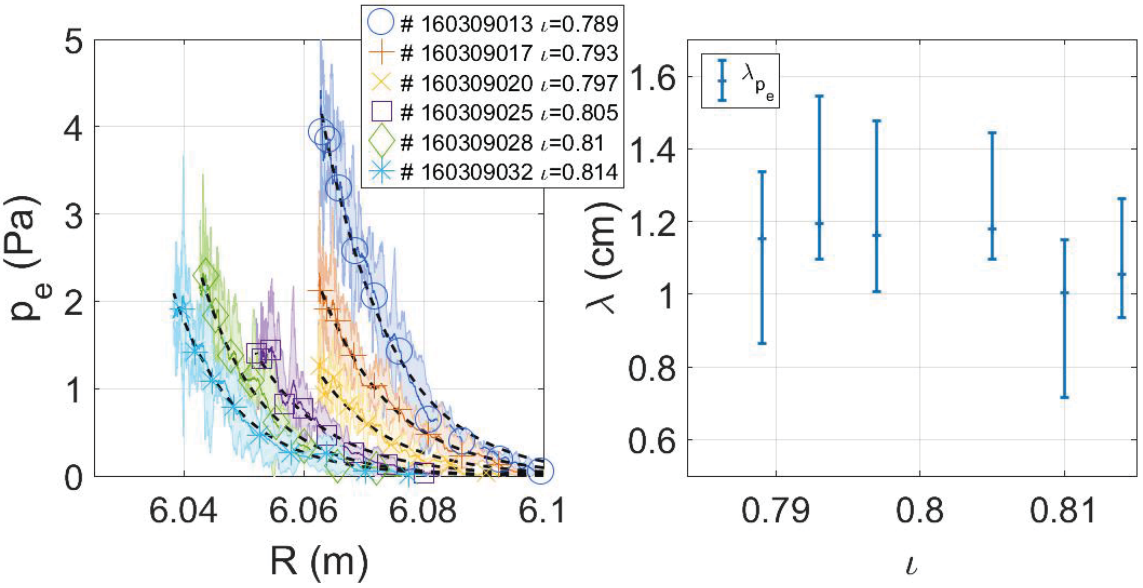

Figure 3.4: Left: Pressure profiles of the iota scan, right: Pressure decay lengths obtained from fit versus central iota (taken from [50]).

For the last configuration, the iota index 13 configuration, this effect is visible in the temperature profile (see figure 3.2), as a local peaking of the electron temperature, which is strongly correlated with the high connection length region in the plot **??**. For the lower configurations this effect is barely visible in the temperature and density profiles. For the plasma potential, one can observe that those regions cause a local peaking in the profile matching the position of the high connection length regions, this is also visible for the index 11 and 9 configurations.

These observations have been made at the helically symmetric experiment (HSX) [55] and at the Large Helical Device (LHD) [56], with the notable difference that the LHD contains a more complex structure of remnant magnetic islands, stochastic fields and edge surface layers.

Figure 3.4 shows the pressure profiles, calculated from the measured electron temperature and density, the fitted functions, the pressure decay length is recognized as an important quantity concerning peak heat loads [57]. On the right side the pressure decay length against the central iota value is plotted. The decay lengths were obtained from the fit of the data, using the product of the electron temperature and density for the electron pressure. The error is calculated by fitting the same exponential functions to the two most extreme cases of the upper and lower error bound. The measurements do not show that the pressure decay lengths change considerably with increasing iota. The density decay lengths obtained from these measurements are also about 1.5 cm. This broad decay length at W7-X is larger than the ones found for tokamaks of comparable size, indeed the pressure decay lengths reported for ASDEX Upgrade are at about 5 mm [58], for other tokamaks decay lengths of the same magnitude are found in [59]. It quite

well matches the prediction from the field line diffusion modelling with $\lambda_{n_e} \approx 1.5\,\mathrm{cm}$ [60]. The density decay lengths can be used to represent the decay lengths of the particle flux, since it is mostly a function of the density, found at W7-AS [61] and about 1 cm at LHD [62].

The comparisons were taken from machines with a divertor configuration though, however it should be noted that the islands, that can be measured by the MPM are in any case cut off by the limiter or the divertor and that the position of the measurement in the island can only be changed by tuning the magnetic field and thereby moving the island up or down. These findings have to be compared to the measured heat loads on the limiter (see reference [54], [63] and section 3.1.2 for the limiter plasma and section for the island divertor configuration 3.2.2).

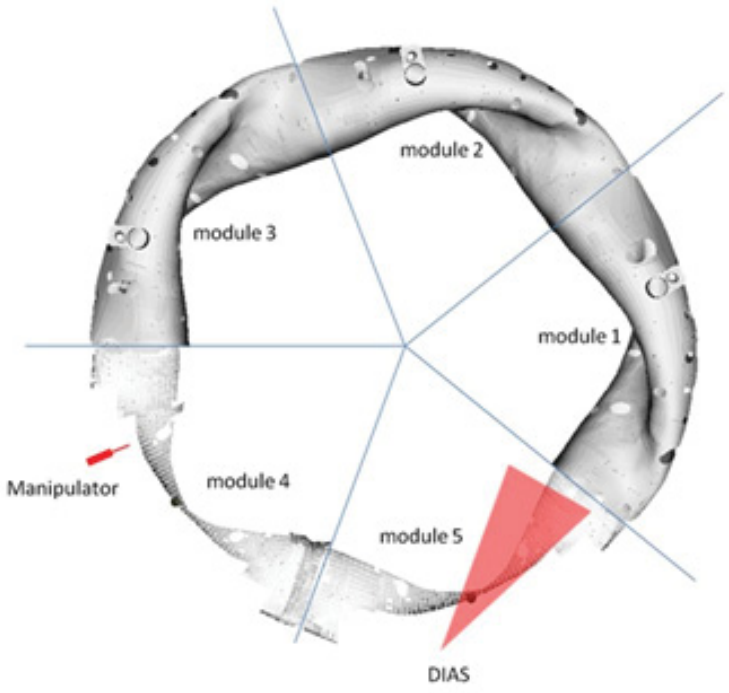

Figure 3.5: Position of the manipulator in module 4 and of DIAS camera in module 5 (taken from [51]).

3.1.2 Configuration dependence of the heat flux in limiter plasmas

The limiter configuration in the first operational campaign of W7-X featured a five-fold symmetric configuration. Those limiters would experience ideally the same heat loads, but the intrinsic error fields cause a considerable asymmetry between the modules [63] [64]. The electron temperature and density profiles measured by the combined probe can be used to calculate the radial heat flux profiles.

The influence of the magnetic topology on the heat loads can therefore be studied in respect to the modification of the magnetic topology of the iota scan. The probe measurements are labeled up-stream, the profiles of the measured temperature, density and the corresponding calculated heat and particle fluxes, can be compared to the measurements of the heat fluxes on the corresponding limiters measured with the DIAS camera [65], labelled downstream and the modelling from EMC3-EIRENE [66][14]. The comparison with the modelling in [14] does show a good agreement with the measurements. Therefore the ion temperature profiles from the modelling are used for the ion temperature contribution in the following calculations. This is necessary since the diagnostic coverage of the ion temperature in the plasma edge has a poor resolution in the first operational phase. A direct calculation of the heat fluxes on the limiter can be found in [67].

In figure 3.5 the position of the manipulator in the mid-plane of module 4 and the field of view of the DIAS camera in module 5 is shown. This presents the possibility to compare the two edge plasma diagnostics by assuming a fair degree of toroidal symmetry.

It is expected that the higher iota configurations experience an inwards shift of the 5/6 island chain located past the last closed flux surface, while the 5/5 island moves closer towards the last closed flux surface from the scrape off layer. In the case of the 5/5 island remnant measurements with the combined probe observed this shift. The two profiles of the electron temperature and density are shown in figure 3.6 for the standard or J and the iota 13 configuration. The shift of the magnetic axis, due to the tuning of the planar coils, is clearly visible in the inwards shift of the profiles. The 5/5 island is also visible for the higher iota case. The measurements were performed at the same ECRH heating of 2 MW. As previously stated the measurements can only be

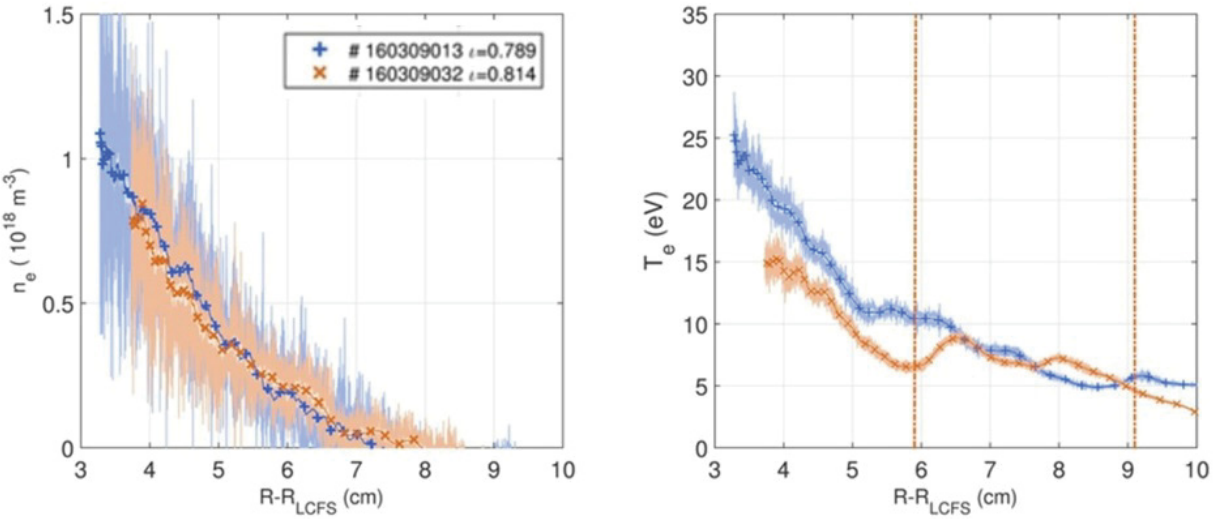

Figure 3.6: Shift of the electron temperature and density profiles for the J and iota index 13 configuration (taken from [51]), the vertical lines mark the extend of island remnant present for modified configuration.

compared by assuming a fair degree of toroidal symmetry, since the manipulator measurements were conducted in the mid-plane of module 4, while the DIAS camera is observing the left side of the limiter in module 5.

The thermo-couple measurements [63] show that the heat load distribution, observed with thermo-couples on the limiters, was highly asymmetric for certain limiters, due to error fields. For the down-stream measurements the DIAS camera was used. The DIAS camera is a micro-bolometer with a wave length range of $8 - 14\,\mu m$, 50 Hz time and a spatial resolution of about 5 mm. The THEODOR code [68] is used to calculate the heat flux on the limiters based on measured the temperatures, which are measured with the IR cameras. The resulting values have

an estimated error of about $0.2\frac{\mathrm{MW}}{\mathrm{m}^2}$, this error is relatively large due to the cameras sensitivity being set to measure the temperatures close to the strike line and not in the position of the field lines from the manipulator impinging on the surface. From [63] one can deduce that limiter 1 experienced the highest heat flux and limiter 3 the lowest. The limiters 2, 4 and 5 can be assumed to have similar heat fluxes. This is important, since this is the needed toroidal symmetry, necessary for the comparison. The field line tracing web tool was used to connect the field lines from the position of the combined probe to the corresponding wall elements. Using the results from the field line tracing one can relate the measurements of the combined probe to those on limiter 1 and 2. The DIAS camera only observed limiter 5, using the result from the thermo-couples, it can be assumed that limiter 2 and 5 experience similar heat loads, for the comparison of the up and downstream heat fluxes.

In this way the up-stream heat flux, calculated from the combined probe data, can be mapped on the existing down-stream limiter measurements, by assuming that limiter 2 and 5 have the same heat flux. In figure 3.7 the down-stream heat flux measured by the DIAS camera and the probe's footprint is shown. The footprint is quite far away from the strike line and therefore only moderate heat fluxes are in the mapped region. This is expected, since the plunge range of the manipulator was limited and the measured up-stream electron temperatures and densities were low. The down-stream heat fluxes on the limiter had to be converted, by taking the incidence angle of the field lines into account [67], turning it into the parallel heat flux:

$$q_{par} = \frac{q_{\mathrm{limiter}}}{\sin(\alpha)}, \tag{3.4}$$

with α as the incidence angle of the field lines on the limiter and $q_{limiter}$ as the heat flux measured with the DIAS camera.

The up-stream heat flux profile is calculated using the electron density and temperature profile and the resulting ion sound speed, which is itself a function of the electron temperature. In addition, the ion temperature from the EMC3-EIRENE modelling, shown in figure 3.8 is used for the ion temperature contribution in the following equation:

$$q_{probe} = n_{\mathrm{e}}\, c_{\mathrm{s}}(T_{\mathrm{e}} + T_{\mathrm{i}}), \tag{3.5}$$

with n_e as the electron density, while assuming quasi neutrality and c_s as the ion sound speed. This equation simplifies a lot by just using the ion saturation current and the collection area instead of the ion sound speed and the electron density:

$$q_{probe} = \frac{I_{\mathrm{sat}}\,(T_{\mathrm{e}} + T_{\mathrm{i}})}{A_{\mathrm{eff}}} \tag{3.6}$$

The measurements in the limiter configuration were conducted in the far scrape-off layer, where the errors of both measurements are quite large. Figure 3.9 shows the comparison of the up and down-stream heat fluxes. The use of the ion temperature from the EMC3-EIRENE modelling, which is twice as large as the measured electron temperature, yields up-stream heat fluxes that are within the errorbars of the down-stream measurements or larger. Also the comparison of the electron contribution to the up-stream heat flux with the total down-stream heat flux can

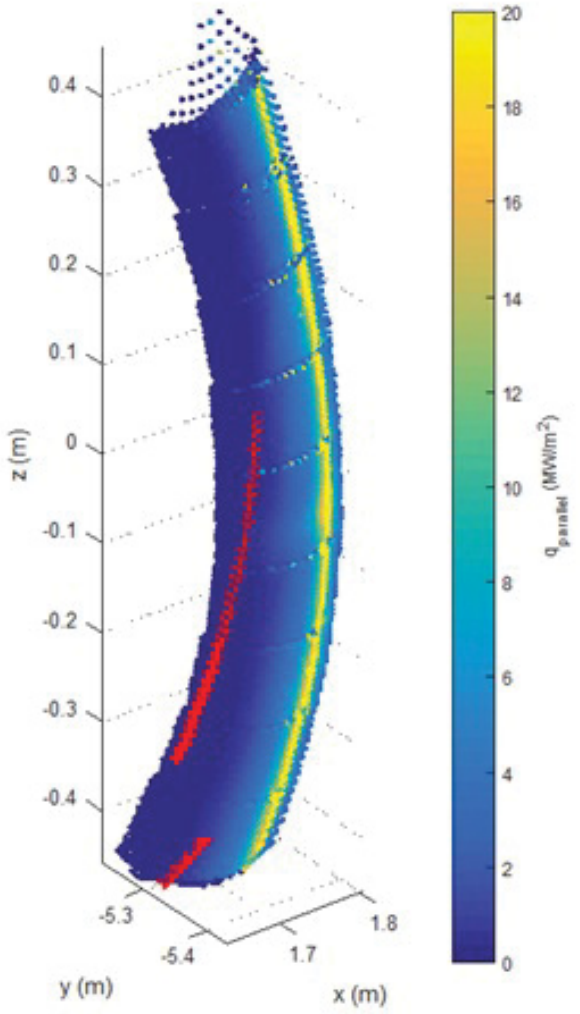

Figure 3.7: Heat flux on limiter 5 measured with the DIAS camera, with the footprint of the combined probe in red crosses (taken from [51]).

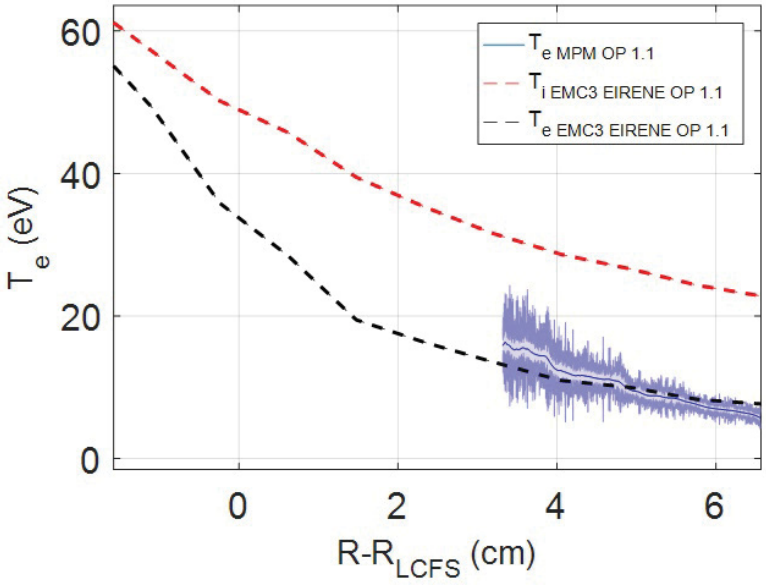

Figure 3.8: Electron temperature measured with the combined probe and ion temperature simulated with EMC3-EIRENE modelling.

actually provide a confirmation for the estimate of the up-stream ion temperature profiles. To achieve matching heat fluxes the high ion temperatures are necessary, $T_\mathrm{i} \approx 2\,T_\mathrm{e}$ is the lower bound for the ion temperature.

One can see in figure 3.9, that the down-stream measurements do not change considerably with the iota scan, the up-stream values on the other hand do. The iota scan shifted the magnetic axis inwards for higher iota configurations, as shown in figure 3.6 and 3.9. For the J-configuration the up-stream values are larger, than the downstream measurements. For the higher iota case both heat fluxes are comparable within the errors.

The footprint of the combined probe for limiter 1 is outside of the DIAS camera's field of view, therefore the comparison is done for the measurements of limiter 2 and 5. In the following, for the sake of better understanding the projection of limiter 2 on limiter 5 will be called the forward direction of the field line tracing and the projection of limiter 1 on limiter 5 the backward direction.

In figure 3.10 the footprint in the forward direction is shown for the limiter J-configuration and for the iota index 13 configuration. This is the footprint for the limiters 2 and 5 with the symmetric heat load.

The pattern of the footprint on the limiter drastically changes from a single line to two fingers, the distance to the area of the highest heat flux (or strike line), indicated by the yellow line, does not change significantly. This is the reason for the down-stream heat loads to not change considerably for the two different configurations.

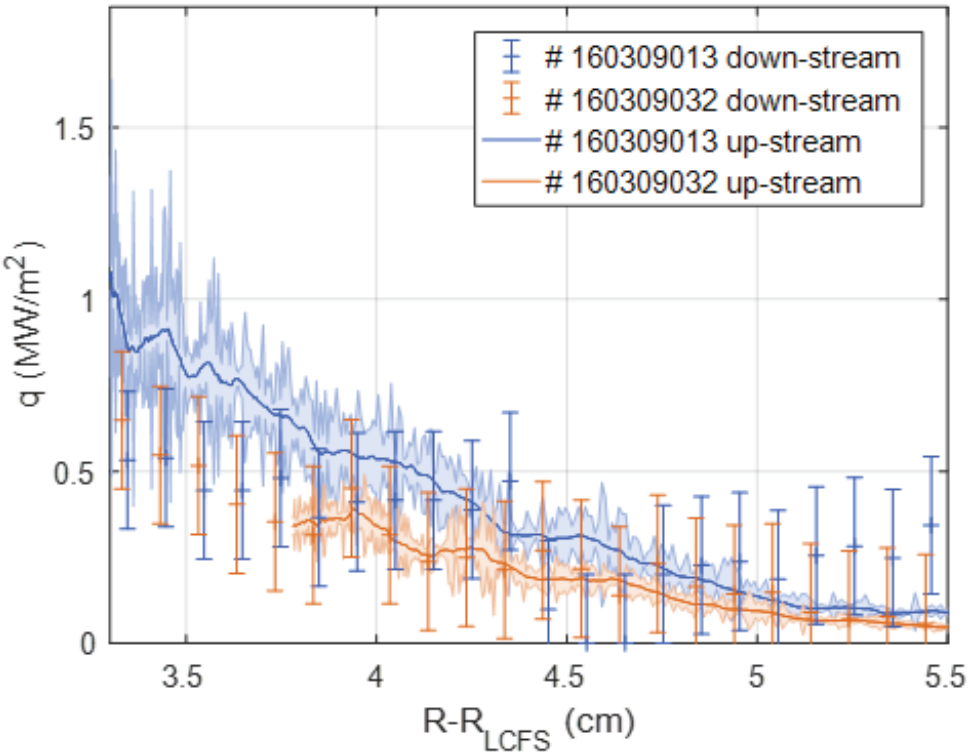

Figure 3.9: Comparison of the heat flux calculated from the combined probe data (up-stream) and the DIAS camera (down-stream) (taken from [51]).

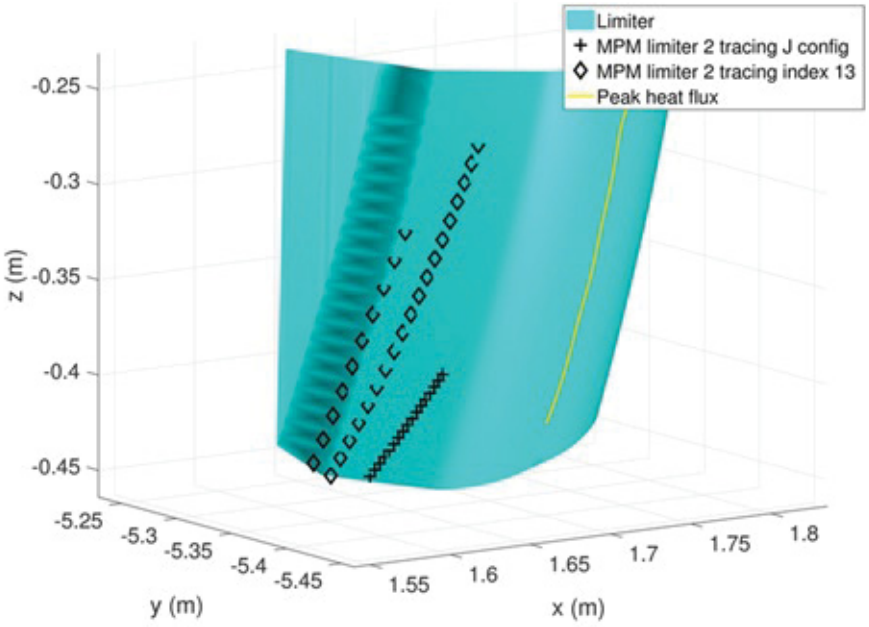

Figure 3.10: Shift of the footprint of the combined probe mapped on the limiter in forward direction, black crosses: limiter J-configuration, black diamonds: iota index 13 configuration (taken from [51]).

Figure 3.11 shows the footprint for the backward direction. The probe should mapped onto the limiter 1, which experience higher heat loads in the standard configuration. Again the single line branches off into two fingers, but here the distance to the strike line increases and thereby the up-stream heat flux in the range of the probes decreases. This can explain the changing of the heat flux due to changing the edge iota, since the footprint on the limiter is modified.

With the assumption of at least partial symmetry between the limiters it is possible to map the position of the combined probe to the limiters. This allows for a comparison of the up and down-stream heat fluxes. The measurements with the combined probe were conducted in the scrape off layer outside of the last closed flux surface only for technical reasons. More interesting results are expected in the next operational phase where the probe plunges deeper into the plasma. The up-stream heat fluxes are as expected similar to or higher than the down-stream measurements on the limiter (under the assumptions for the heat sheath transmission coefficient and the modelled ion temperature). This is found for both configurations, the J-configuration and within the error range for the iota index 13 configuration. A more complete analysis needs to take additional effects like radiative and frictional losses into account. It is also obvious that an additional measurement for the ion temperature is necessary to confirm the estimate for the

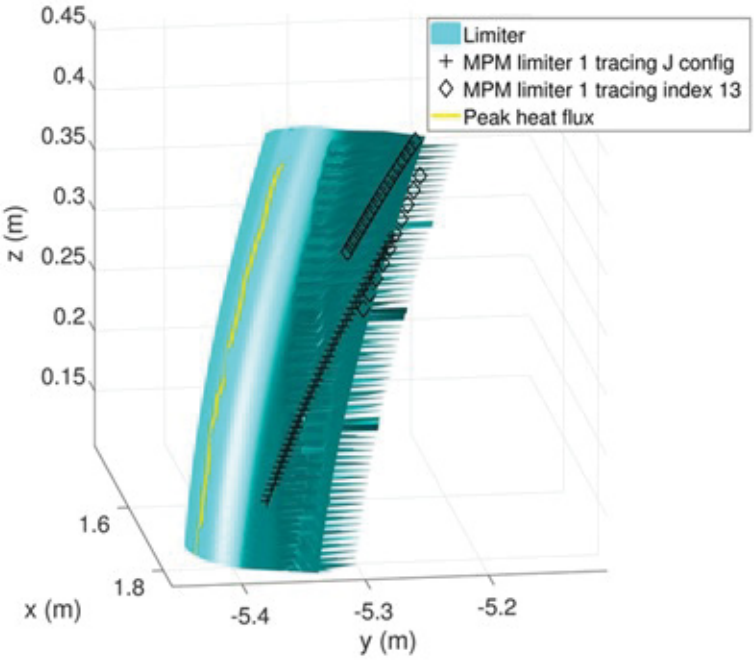

Figure 3.11: Shift of the footprint of the combined probe mapped on the limiter in forward direction, black crosses: limiter J-configuration, black diamonds: iota index 13 configuration (taken from [51]).

up-stream heat fluxes. The data from EMC3-EIRENE modelling, combined with the heat flux comparison, showed that the ion temperature in the edge is about a factor of two larger than the electron temperature.

The iota scan shows a reduction of the heat fluxes on limiter 1 while the corresponding heat flux on limiter 2 remains largely unchanged with increasing iota. This is also visible in the up-stream profiles and the change of the footprint on the limiter.

The modelling from EMC3-EIRENE, using the combined probe's measurements as input data, can supply also the heat fluxes at any given position in the device. When radiative and other effects are taken into account, the calculation is computationally costly. Using the mapping of the field lines to directly compare the two diagnostics in two different positions represents a fast, although incomplete alternative, as it does not take additional effects like radiative losses into account.

3.2 Topology effects in island divertor plasmas

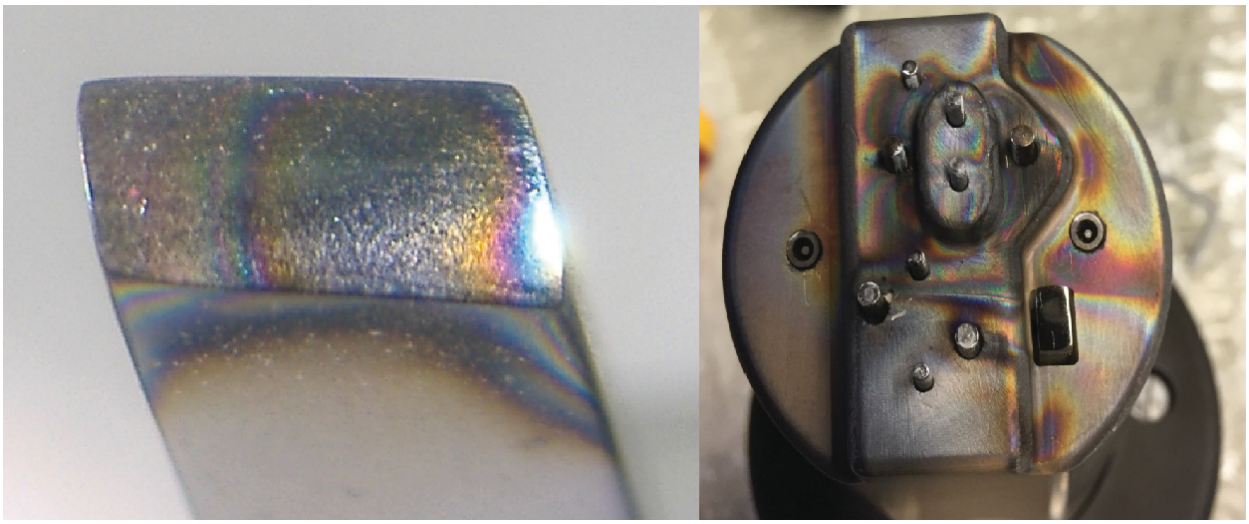

Figure 3.12: Right: Tungsten material sample after exposure. Left:Photograph of the front facing of the upgraded combined probe after OP 1.2a.

For the second operational campaign the combined probe was upgraded (shown in figure 3.12) with an ion sensitive probe, to simultaneously measure the ion temperature in addition to the Langmuir probes measurements for the electron temperature. A tungsten material sample and a gas puffing system were added. The second operational campaign OP. 1.2a started in summer 2017 and lasted until early December. The stellarator was upgraded with an inertially cooled set of divertors. Still ECRH heating was the only source of heating for the plasma. The results presented in the chapter will be published in [69].

It became apparent during the campaign, that the island divertors allowed for a considerably improved machine performance. The effective pumping made additional fueling (like the gas puffing from the probe) necessary to achieve higher densities. The discharges were due to these favorable conditions quite reproducible and the densities remained fairly constant throughout the day. At similar edge temperatures much higher densities were recorded with the combined probe and other diagnostics. The considerably higher densities supposedly led to a better coupling of ions and electrons, which resulted in similar temperatures for the two species. Also the precise knowledge of the offset of the position signal made it possible to probe deeper into the plasma edge and very close to the last closed flux surface.

The position of the manipulator was recalibrated:

$$x_0 = -6009\,\mathrm{mm}$$

$$y_0 = -2209\,\mathrm{mm}$$

$$z_0 = -172\,\mathrm{mm}$$

The position of the probe is then caculated using:

$$\vec{P} = \begin{pmatrix} x_0 \\ y_0 \\ z_0 \end{pmatrix} + (d + L) \begin{pmatrix} 0.9297 \\ 0.3683 \\ -0.0051 \end{pmatrix} \tag{3.7}$$

With d as the distance of the manipulator plunge and L the length of the individual probe tip. The probe actually slightly moves downwards as it moves into the plasma, this is caused by the weight of the probe. For the position of each individual pin on the angled surface figure 4.3 can be used. A small time shift between the position measurement and the recording of the measurement signals of 3 ms has to be taken into account.

A dedicated Mach probe, a retarding field analyzer and a fluctuation probe were used to measure also the plasma edge profiles. It should be noted here, that only the triple probes could fully measure the edge temperatures, due to unexpectably high floating potentials and a lack of sufficient biasing for the swept Langmuir probes. The limited data from the retarding field analyzer (RFA) probe and the Mach probe cannot yet be used for comparisons with the combined probe for the OP 1.2a, since analysis is still pending. For the second operational campaign a full set of infrared cameras was installed to observe all divertor modules. Therefore it is no longer necessary to assume module symmetry to study the up and down-stream heat fluxes. The combined probe was employed in four different configurations, the standard (EJM), the high iota (FTM), the high mirror and the reversed field configuration, shown in figure 4.4, 4.5 and 4.6. These configurations differ in the position size and width of the islands and it is possible to observe this with the profiles of the combined probe.

The probe was not used in discharges that had a configuration with a strong modification of the trim coils, due to large and unexpected shifts of the strike line on the divertor and the last closed flux surface, which made either safe or useful operation of manipulator mounted probes difficult. It was not possible to adjust the probe position, if the session included a fast variation of the currents from discharge to discharge.

The high iota configuration measurements were carried out on the 25.10.2017 in the OP. 1.2a. The high iota discharges were mostly helium plasmas due to the better recycling behavior, with normally a 20% hydrogen admixture of outgassing from the walls. The high iota configuration has a considerably thinner edge island, at the position of the manipulator path and the connection length is noticeably shorter in the edge region.

The measurements in the reversed field configuration are very similar to the standard configuration. This configuration was tested on the last day of the campaign 07.12.2017. The triple Langmuir probe was not fully operable and thus the temperature and density profile measurements solely relied on the swept guard ring of the ion sensitive probe. The field line tracing calculations were complicated by the loads that affected the magnetic coils. The magnetic field generated by the coils can suffer a considerable variation from the ideal case with no deforma-

tions of the coils. For further analysis the "real" case, with the deformed coils and currents to compensate this effect, is considered.

3.2.1 Edge profile measurements in divertor plasmas

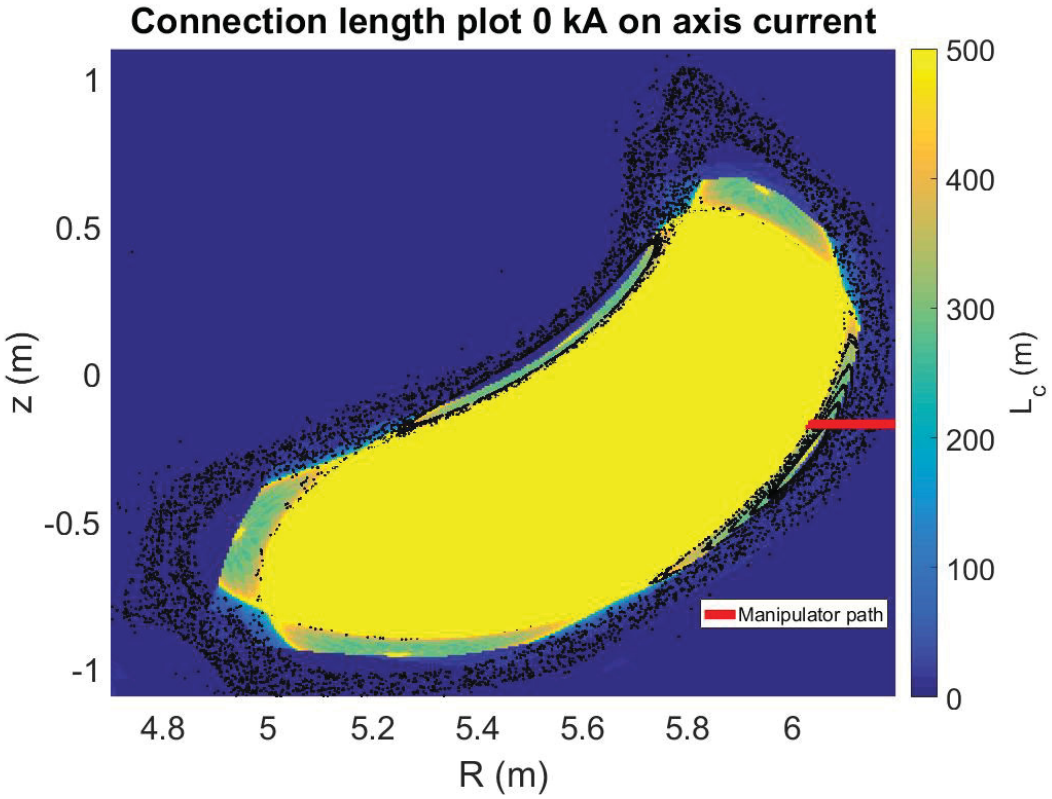

Figure 3.13: Connection length and Poincaré plot in the toroidal plane of the manipulator for the standard configuration.

The upgraded combined probe was operated again with a triple probe configuration and in addition an ion sensitive probe. The ion sensitive probe was only in the last week of the experiment fully operational, at the same time, due to damage on the manipulator, the triple probe was not functioning. The Mach probe was fully functioning for most of the campaign. The same error calculation as in the first campaign was used for temperatures and densities and all quantities that were deduced from them. The total level of noise is of similar magnitude as in the OP 1.1, but the absolute measured values are much higher, which provides a more favorable signal to noise ratio.

It was pointed out that for a better or more precise calculation of the electron density a good estimate of the effective charge of the plasma is necessary, the analysis from relevant diagnostics like HEXOS is still ongoing and modelling results from EMC3-EIRENE are expected to yield

lower values than the limiter campaign due to the reduced recycling from the carbon walls.

Figure 3.13 shows an overlay of the Poincaré plot and the connection length in the toroidal cross section of the manipulator. The Poincaré plot represents the magnetic topology without the divertor, while the connection length in the plot indicates how the island is cut in half. This is the "real" coil setup, taking coil loads and deformations into account, without additional error fields or beta effects. The model that compensated for the coil deformations is still being improved.

Measurements with combined probe in the standard configuration were carried out on the 26.10.2017. Figure 3.14 shows a set of temperature and density profiles recorded with the combined probe.

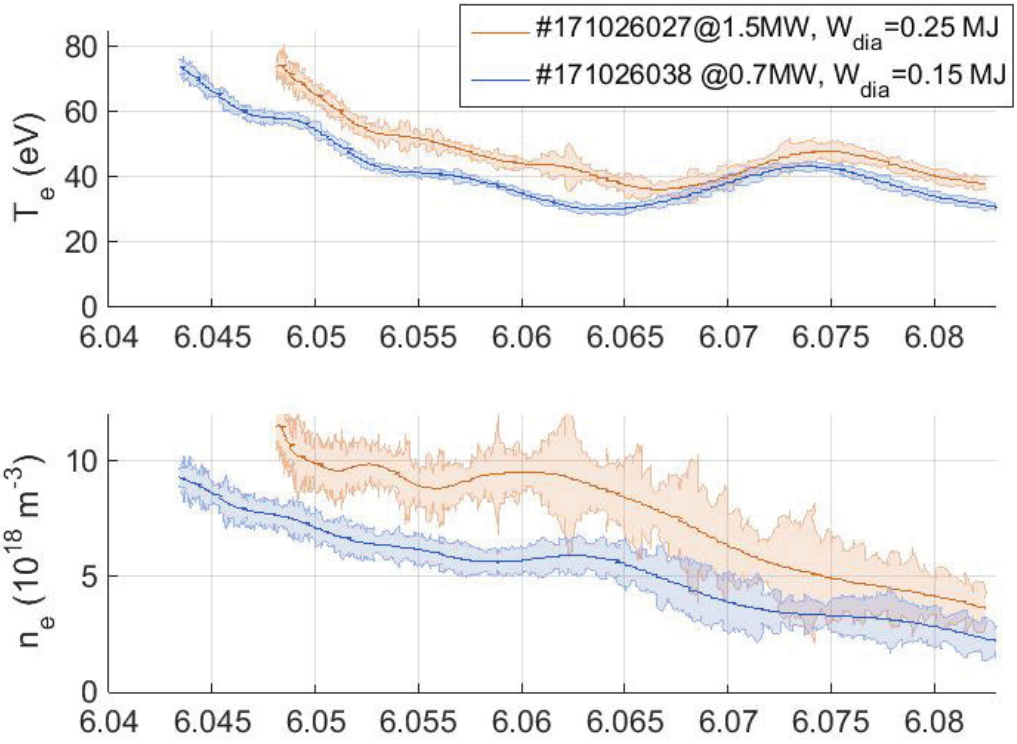

Figure 3.14: Electron temperature profile and electron density profile.

The two presented discharges were Helium cleaning discharges, with a mix of hydrogen and helium, at relatively low powers.
Discharge #38 has about half the diagmagnetic energy compared to discharge #27 and thus a lower plasma beta. The Poincaré plot predicts the edge island in the path of the manipulator to be centered at around $R \approx 6.072$. The island is cut off by the divertor and therefore one should refer to it as an island remnant.

The measurement of the magnetic field profile in figure 3.15 shows a local deviation between the measured values in vacuum and the field line tracing calculation in the viccinity of the previously mentioned island remnant. The temperature profile shows the typical bulging in the area

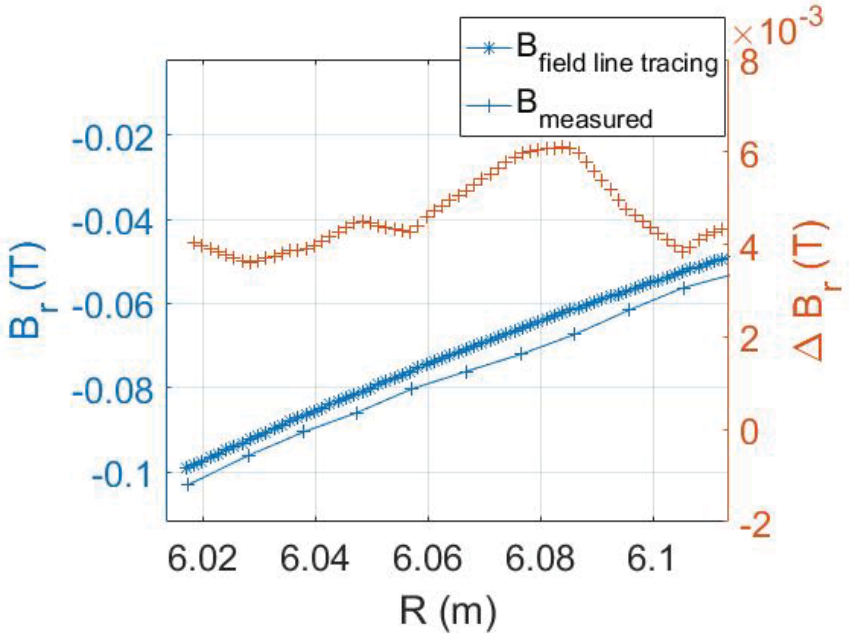

Figure 3.15: Measured radial magnetic field compared to the vacuum calculation from the field line tracing.

of the island in the standard configuration, attributed to the long field lines. In figure 3.16 the temperature and density of the electrons and the correlation spectrum for two floating potential pins (pin 4 and 7) are shown. The turbulence is suppressed in the cut off island structure but strongly present further inwards. The mode structure has been studied for Op. 1.1 [70], but the absence of an island for the most part had stifled a possible comparison between the limiter and the divertor setup.

The flow profiles, measured with the Mach probes, show a flow reversal in the edge island. This has also been observed in the reflectometry measurements [71]. The parallel plasma flow has been identified in the reflectometry measurements to be caused mostly by the $\vec{E} \times \vec{B}$ drift. The island structure is reflected in both the Langmuir and Mach probe measurements. The flow towards the divertor will change depending on the plasma being attached or detached to the divertor. It should be noted here that the local peaking of the electron temperature profile, which is associated with the long connection lengths in the island remnant, was already observed in the limiter standard configuration discharge with an additional planar coil current (see figure 3.2). The temperature peaking was observed in this discharge due to an inwards shift of the edge island that was normally cut off by the limiter. The connection length profile shows an island remnant similar to the standard divertor configuration (compare figure 3.3 and 3.13).

The discharges with a higher heating power, higher plasma beta and also higher toroidal

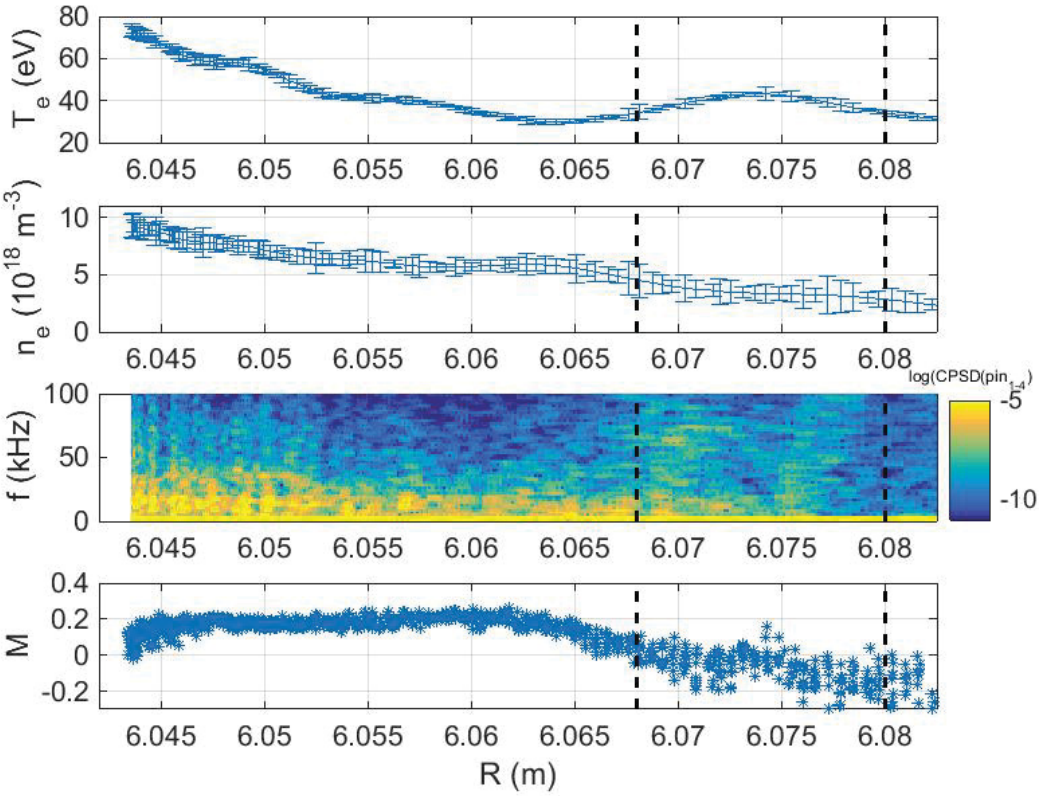

Figure 3.16: Comparison of the measured temperature and density profile, the cross power spectral density of the poloidally seperated floating potential pins pin 1 and pin 4 and the flow velocity given in Mach for discharge 171026038, the vertical dashed lines indicate the borders of the assumed island remnant position

current, in the standard configuration, yield a remarkable outwards shift and a thinner island as well. This is expected as the positive bootstrap current will push the islands further out and will partially heal them. The electron pressure profile can again be calculated from the product of the electron temperature and density. Figure 3.17 shows the electron pressure profiles for the standard configuration.

Since the probe measured outside of the last closed flux surface, only a single exponential function was used for the fit. The fit parameters resulted in an adjusted mean square value of more than 96% with the presented data. The fitting of an exponential function for the electron pressure profile for discharge #38 yielded a decay length of $\lambda_{p_e} = 1.89\,\mathrm{cm}$ and for discharge #27 a decay length of $\lambda_{p_e} = 2.48\,\mathrm{cm}$. Both values are considerably higher than the those of the limiter configuration from the first operational campaign 3.4. This again is favorable when compared to other machines such as Asdex with 5 mm [58] or LHD with 1 cm [62].

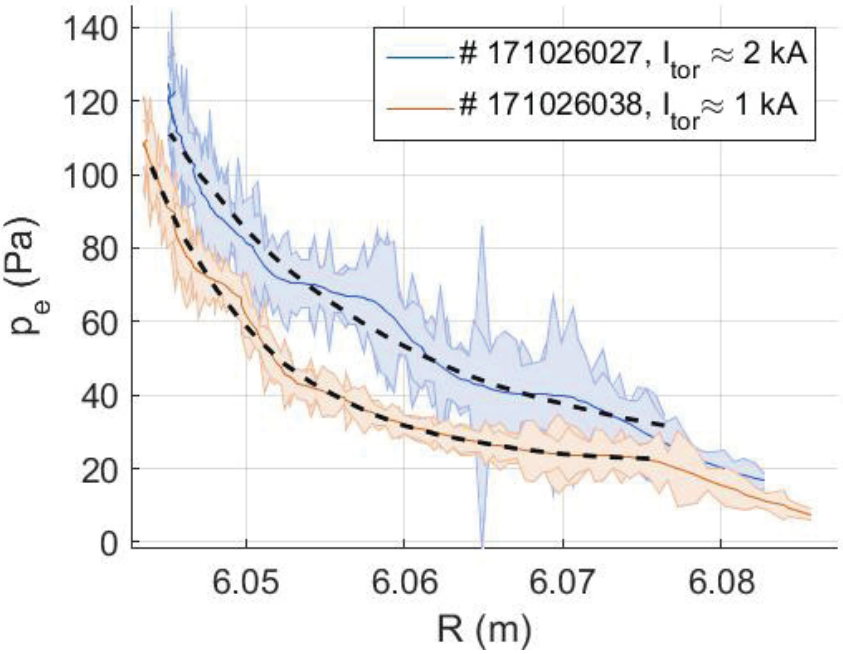

Figure 3.17: Electron pressure profile with fit for the standard configuration.

In figure 3.18 the electron temperature and density profiles were measured in the high iota configuration. The discharges experienced a plasma beta from 0.3% to more than 1%. Identifying an island structure was relatively difficult in the high iota case due to the connection lengths and the island width being very small. The high iota configuration has a very thin scrape off layer and also a very small edge island. A similar bulging of the electron temperature, like in the standard configuration, would be expected at about $R = 6.02$. But the islands feature a comparatively short connection lengths and are barely visible in the profiles. For analysis of the configuration effect the bare profiles cannot suffice in this case, since the beta effect on the island is not visible in the profiles. The decay length of the pressure profiles and the change of the field line pitch angle can give further insight into the interplay between the topology and the plasma parameters related beta.

The discharges $\#38, 39$ have a relatively small beta $\beta \approx 0.3\%$ and small positive toroidal current $I_\phi \approx 0.5\,\mathrm{kA}$, the discharge $\#36$ at an intermediate beta value of $\beta \approx 0.8\%$ has a rather small negative current $I_\phi \approx -0.3\,\mathrm{kA}$ and the high beta discharges $\#20, 42$ reach negative currents of $I_\phi \approx -0.5\,\mathrm{kA}$ and $I_\phi \approx -1\,\mathrm{kA}$ respectively. For the high iota configuration a negative current was measured and the islands were supposedly shifted inwards at higher beta values. This inwards shift is present for the discharges in figure 3.18. The calculation of the pressure decay lengths for the high iota configuration shown in figure 3.19 result in considerably smaller decay length for both high and low beta values. The high iota configuration featured a relatively small edge island with comparably low connection lengths in the edge, it is therefore not surprising that the decay length is also small.

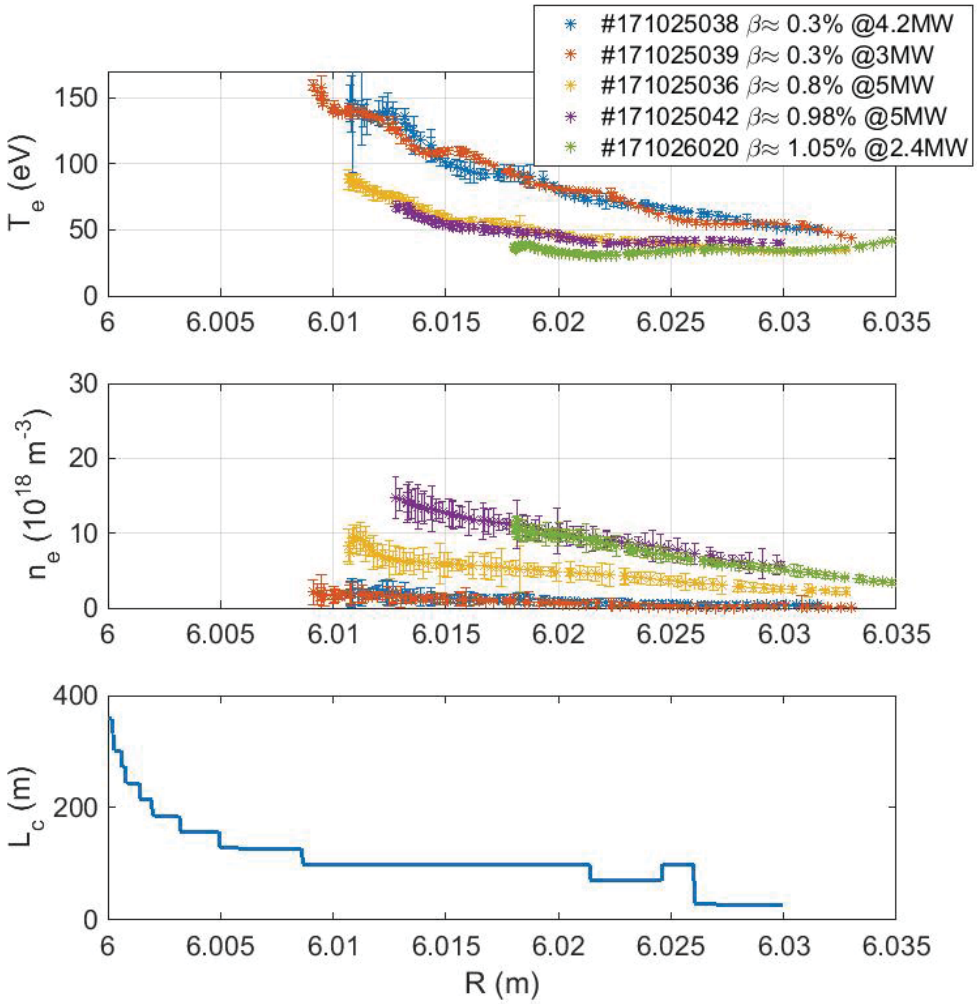

Figure 3.18: Electron temperature and density profiles obtained from a density and heating power scan and corresponding connection lengths calculated assuming vaccum condition in the high iota configuration.

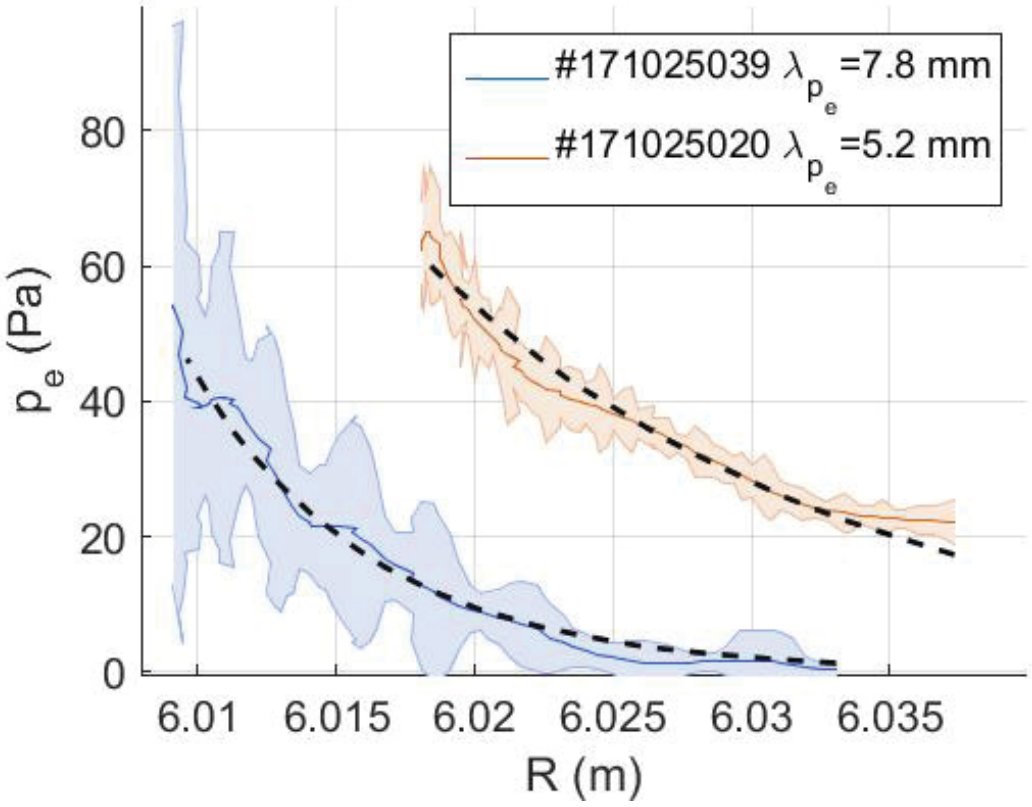

Figure 3.19: Electron pressure profile with fit for the high iota configuration.

The low beta discharge had a calculated decay length of 7.8 mm and the high beta discharge a decay length of 5.2 mm, which is still comparable to the aforementioned machines like ASDEX and LHD. It is obvious that the plasma beta can strongly modify the magnetic topology [10], which is visible in the shape and position of the profiles.

The effects of the high heating power, high plasma beta and the toroidal current, are slightly entangled. In the case of high heating powers normally a higher plasma beta and also stronger toroidal current is observed. For strong toroidal currents and high plasma beta the standard configuration showed an outward movement while the high iota configuration experiences an inward shift of the profile. This observation seems counterintuitive as the positive currents should shift the magnetic island inside and a negative current would move the island outside. For the study of the effect of the plasma modification the discharges # 171026027 and # 171026038 were considered. Figure 3.20 shows the overal plasma conditions during these two discharges.

The plasma conditions during these discharges differed concerning the heating power of 0.7 MW and 1.5 MW respectively. The central electron density, from the interferometer system [74] measurements, was relatively constant. The electron temperature from the second channel

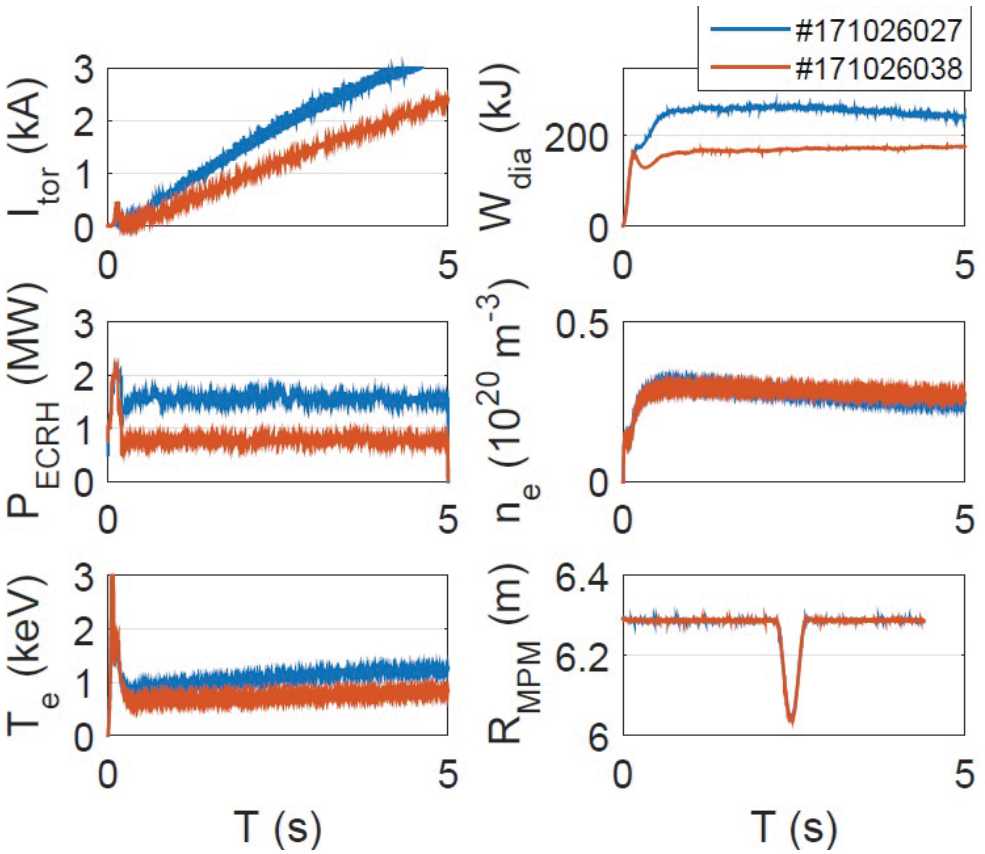

Figure 3.20: Overview of the conditions during the dischargs # 171026027 and # 171026038, left, toroidal current, injected heating power, central electron temperature, right: diamagnetic energy, electron density and manipulator position.

of the ECE system [75] increases slightly. The stored diamagnetic energy [76] and the toroidal current increase, due to higher heating, almost twofold. The manipulator plunges were done at the same time for the two discharges.

By assuming that the toroidal current is a coil located on the magnetic axis, one can try to modify the magnetic topology to reproduce the currents effects on the profiles and the position and width of the magnetic islands. Figure 3.21 shows the modification of the magnetic configuration by applying a current of 2 kA to the magnetic axis and the case without a net plasma current. One can see that the cut off island is moved inwards with higher currents and the confined region in the island is growing in size. The overall connection length increases as well in the edge region, which can be an explanation for the shift of the profiles. In addition, the pressure profile shows a change for the higher current in figure 3.17, this can be attributed to a change of the connection length in the edge region as observed in figure 3.21.

This increase of the island size was also identified as the reason for the shift and broadening of the heat flux profiles on the divertor [8][77][72]. Interestingly though the divertor measurements

show a continued increase in the shift and broadening with an increasing toroidal current, the reflectometry measurements observe the 5/5 island remnant for 1 kA and 2 kA, but for 5 kA no island remnant is to be seen [71]. The island remnant simply disappears for a sufficiently high toroidal current. This possibly has far reaching implications for the developing plasma current, which will not only increase in magnitude, but also experiences a change in its profile. This will make further analysis and an improvement of the connection length calculation with possibly HINT necessary [73]. The VMEC calculations for the standard configuration (see figure 4.7) and a case with an increased iota that corresponds to a plasma with a toroidal current (see figure4.8) show that this additional current shifts the island remnant inwards. The current needed to

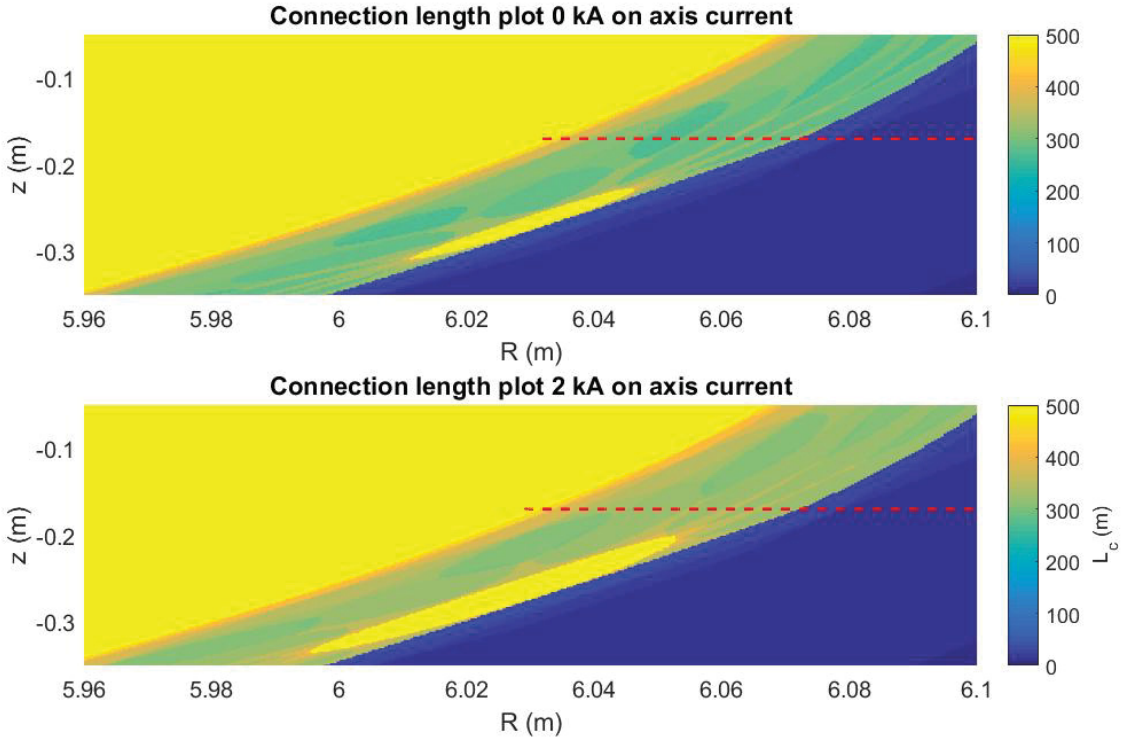

Figure 3.21: Connection length of the standard configuration in the plasma edge, with indication of the manipulator position in red, top: no on axis current, bottom 2 kA on axis current.

achieve the observed shifts is higher than the actual plasma current that is measured, but the current profile that was assumed is possibly too simple. In the case of current distributions that have currents more close to the island, the modification of the edge magnetic field can be stronger with lower net toroidal currents measured. These effects will need to be further studied with the use of HINT, but the underlying effect of the toroidal current at high betas can be understood with the simple model.

3.2.2 Scrape-off layer transport in divertor plasmas

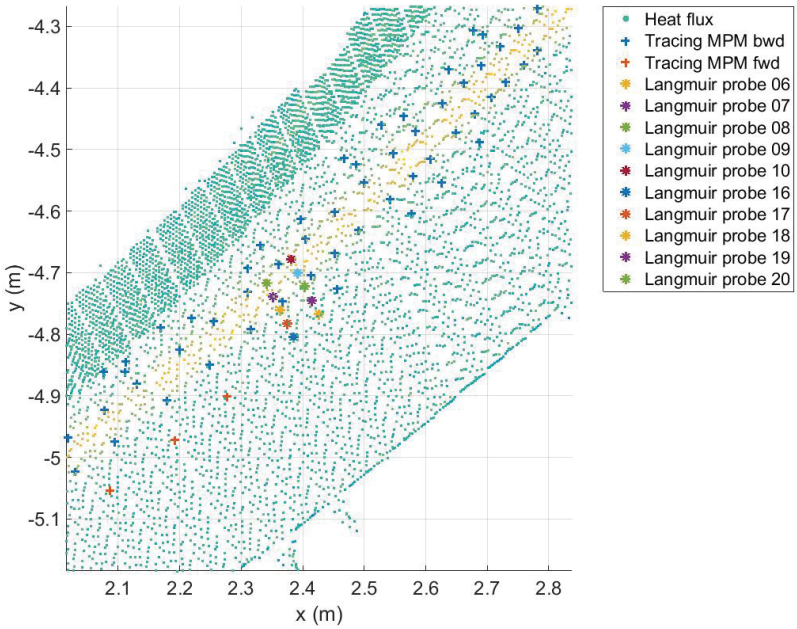

Figure 3.22: Field line tracing of the manipulator onto the divertor module 51 in the machine module 5 with the matching divertor Langmuir probes.

The heat flux was again calculated using the electron temperature and density from the manipulator and the ion temperature estimation from the EMC3-EIRENE modelling. The ion temperature measurements with the ion sensitive probe and the retarding field analyzer were not carried out in the same discharges as the measurements with the triple probe. The results from the direct ion temperature measurements show that the two species have depending on the discharge either a similar temperature or higher ion temperatures. The field line tracing tool was used to match the temperature and density measurements onto the divertor.

Figure 3.22 shows the field line tracing for the standard configuration on divertor module 51 where the divertor Langmuir probes and the manipulator probes coincide on the module surface. The manipulator has been plunged deep enough to actually reach the strike line. The divertor Langmuir probe results can be used to calculate the electron contribution to the divertor heat flux. This can serve as an indirect way for the calculation of the ion temperature up stream. Interestingly, there is no shadowing of the Langmuir probes on the divertor observed for the plunge of discharge #38 in the standard configuration.

The upstream heat flux was calculated using the assumption that the ion and electron temperature was equal. Figure 3.23 shows the calculated up stream heat flux, the calculated and the measured down stream heat flux. The heat fluxes are of the same order of magnitude but,

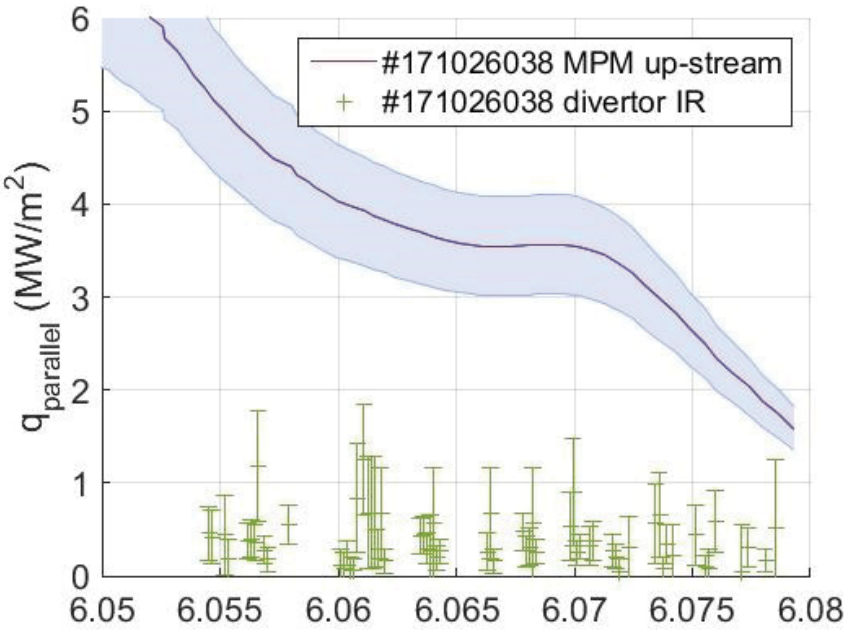

Figure 3.23: Comparison of the up stream heat flux measured with the combined probe on the MPM and the down stream heat flux measured on the divertors with the infrared cameras.

while the up stream profiles calculated with the Langmuir probes are indeed a profile, one can see that the down stream heat flux does not have a exponential decay over the traced ranged. It must be assumed, that due to the more complicated island structure and possible error fields and in addition strike line broadening, the heat flux pattern differs considerably from the up stream profile. The measurements with the infrared cameras might not have sufficient resolution to measure a possible branching of the strike into several finger as it was done with the H-alpha camera. For further studying the relation between the up and down stream heat fluxes, it is necessary to use measurements from the high iota configuration. The high iota configuration would have possible the lowest influence of the magnetic edge island and therefore might feature a similar behavior like the limiter configuration from OP. 1.1.

The edge region is very slim in the high iota configuration, the connections lengths are very short and the islands are not visible in the profiles. It is expected that due to the edge islands being cut off with a very narrow scrape off layer, a configuration similar to limiter plasmas in the OP. 1.1 would be observed. The data for this is also of low quality since the field of view of the divertor cameras was optimized for the standard configuration, therefore the resolution in high iota configuration in the current state does not allow a comparison.

One can use the EMC3-EIRENE output (with both the MPM and the divertor Langmuir probe data for the input) as an estimate for the ion temperature. Figure 3.24 shows the measured electron temperature and the modeled electron and ion temperatures. While the electron tem-

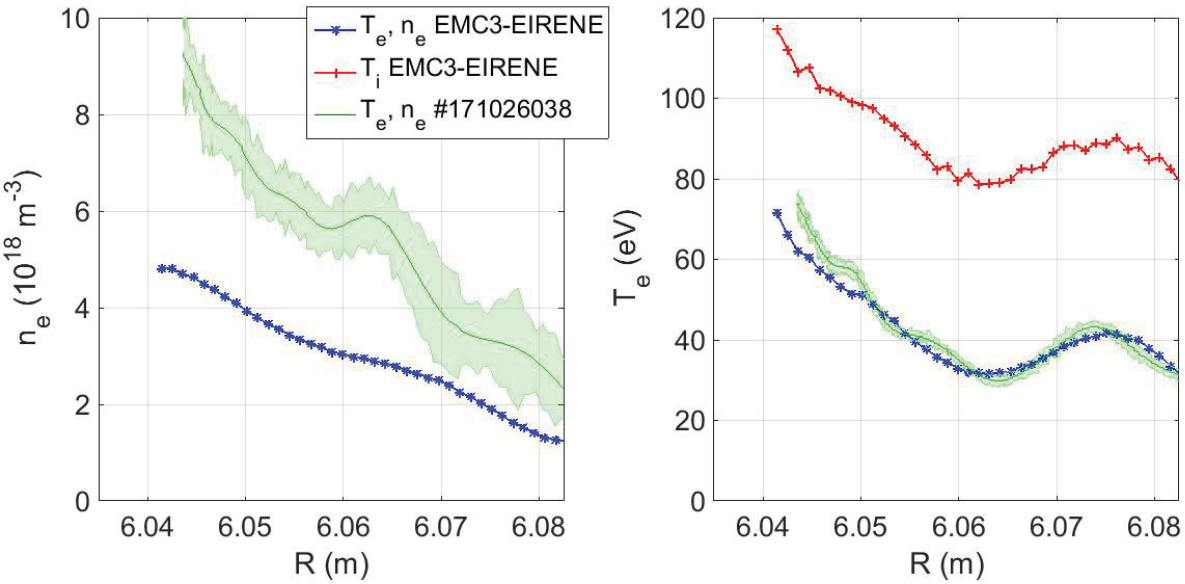

Figure 3.24: Comparison of the measured electron temperature and density and ion temperature with the results from the EMC3-EIRENE modelling.

perature matches quite well, the electron densities differs due to the the larger effective charge used in the EMC3-EIRENE model. The modelling is also able to reproduce the local peaking. The estimates for the effective charge and also 3D profiles along the field lines are useful for understand the transport in the edge. This will possibly be the venue to explain the local peaking of the electron temperature profiles close to the edge island remnant.

3.2.3 Island effect on the edge radial electric field

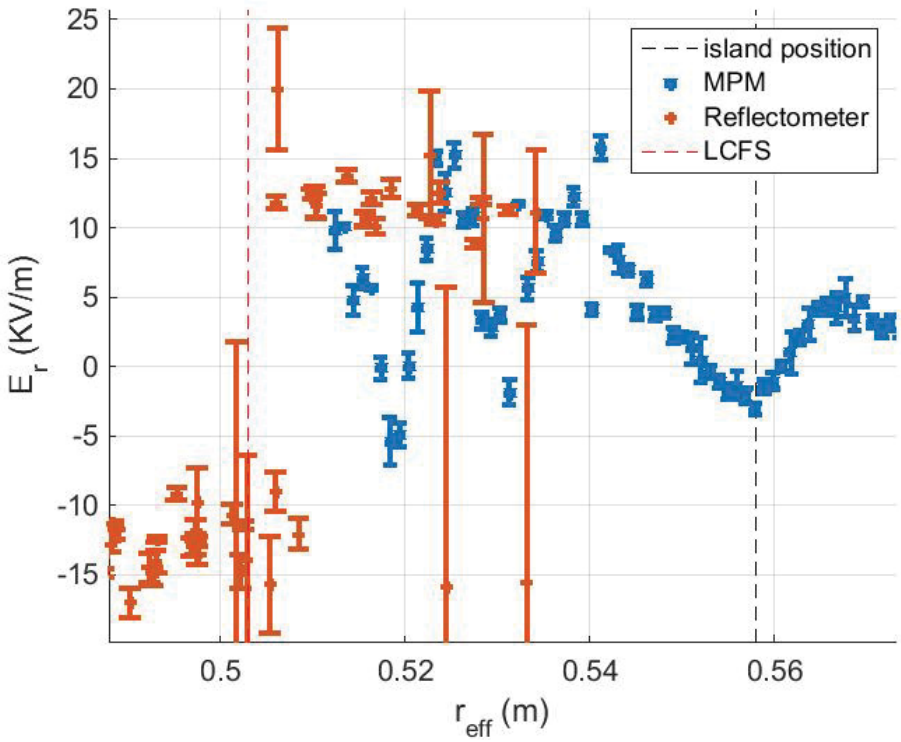

Figure 3.25: Comparison of the radial electric field from reflectometry (blue) and the Langmuir probes (red) of discharge # 171026038 (standard configuration).

The radial electric field was calculated for the island divertor plasmas in the same manner as before in the limiter case. The densities were considerably higher, which meant that the reflectometry was restricted mostly to the edge [71] and the manipulator plunged deeper close to the last closed flux surface. Figure 3.25 shows the measurement of the radial electric fields for the OP. 1.2a standard configuration of both the reflectometry and the probe.

As expected one can now compare the two measurements since the range of the two diagnostics is matching. The necessary density of $0.6 \cdot 10^{19}\,\mathrm{m}^{-3}$ was reached very close to the 5/5 island. The measurements overlap therefore close to the edge island. Interestingly one can see that the radial electric field jumps several times from a large positive value to large negative value in the area where the last closed flux surface is expected. It is suspected that this actually is tied to turbulent behavior (or the lack of it) in vicinity of the island shown in figure 3.16.

One can see in the edge region measured by both diagnostics, that the radial electric field is positive. The probe measurements being situated more outwards show a local negative electric field at the position of the island. The density directly at the island was not high enough to allow measurements with the reflectometer, but with additional puffing from the probe it is possible

to achieve plasma conditions that allow an overlap of both diagnostics in the island.
The measurements of both diagnostics combined confirm the prediction that the radial electric field jumps from positive to negative, while crossing the last closed flux surface or other better confined regions like the island, but it is also evident that the edge island structure complicates this picture. This behavior was also observed in the parallel flow measured with the Mach probe. Again, to guarantee a full comparison of the profiles a more bold operation of the manipulator is necessary, since the results suggest that the last closed flux surface was missed by a few millimeters. One reason for a possibly observed difference in the island width is the different toroidal cross section.

The plasma has a very unique shape, that varies from a so-called bean shape to the tear drop, with this also the island width changes. The manipulator naturally sees only a thinner island than the reflectometer. But irregardless of the plasma shape the scrape off layer and the outer edge of the island has the same relative position to the flux surfaces. The reflectometry measurements and the manipulator were able to observe the edge island remnants, as well as the modification in size and position. Again one point out the reflectometry due to less operation constraints and continuous operation was able to observe more discharges and did see the disappearance of the island for toroidal currents of about $2.5 - 3$kA [71].

Chapter 4

Conclusion

The aim of the thesis was the study of the connection between the magnetic topology and the edge equlibrium profiles that were measured with the manipulator mounted probes, this included:

- Commissioning of the manipulator
- Developement of probe heads for the manipulator
- Measurement of edge eqilibrium profiles like the electron temperature and density, the radial electric field, the local magnetic field profiles and the flow velocity
- Confirmation of the topology by comparison of the measured profiles with the field line tracing results
- Comparison of the heat fluxes measured with the infrared cameras on the divertor with the calculated profiles from the manipulator probe
- Calculation of the up-stream ion temperature profiles from the heat flux comparison

The multi-purpose manipulator was established as a prime tool for edge plasma measurements by the successful use of a variety of probes in the past two campaigns. The combined probe and its upgrade were developed and employed for the measurements of edge plasma parameters such as the electron density and temperature, the floating potential, the plasma flow and the radial electric field. The upgraded version also contained an ion sensitive probe for the measurement of the ion temperature profiles and a gaspuffing channel.

The temperature and density measurements were able to show the effects of changing the configuration. While the first trim coil experiment suffered from a bad machine condition, the so called iota scan-experiment allowed for observing the edge islands remnants, that appeared by tuning the planar coils and shifted the plasma inwards. The 5/5 island remnant that would have been normally cut off by the limiters was confirmed with the connection length calculation, using field line tracing. Beta effects were hardly possible to study in the limiter phase of the machine operation due to safetylimits imposed on the densities and discharge duration.

With these measurements other quantities like the radial electric field could be calculated and compared to the reflectometry measurements. For the limiter campaign OP. 1.1 it is obvious that the manipulator, due to an at the time unknown position off-set, did not plunge deep enough and together with the low densities could not reach a matching range. Still, the comparison confirms the prediction, that the electric field is positive on outside and negative inside the last closed flux surface.

The reliable measurement of the electron temperature and density profiles, allowed the calculation of the up-stream heat flux under certain assumptions for the ion temperature and flow velocity. This heat flux compared to limiter measurements showed that the ion temperature has to be two times larger than the electron temperature, in order to avoid having lower up- than down-stream heat fluxes. This finding is supported by EMC3-EIRENE modelling, using the measured profiles, that also yields ion temperature twice the electron temperature. The comparison of the up and down stream heat fluxes showed, that the original goal of the iota scan, to reduce the asymmetry of the heat loads and the limiters, was achieved.

The second operational campaign Op 1.2 with an edge island divertor featured several configurations in which the upgraded combined probe was utilized, here it again obtained electron temperature and density profiles, this time with a proper positioning of the manipulator ranging very close to the last closed flux surface. The island structure and both the effects of the configuration, heating and fueling could be observed. Further analysis will be done with the use of the HINT code, which can take plasma currents and therefore also beta related effects into account. Also more tests of the gas fueling with the probes are planned. This is especially interesting, since it improves the conditions for the measurement with both the probes and the poloidal correlation reflectometer at the 5/5 island remnant.

The probe plunged considerably deeper (with respect to the last closed flux surface) and the densities were one order of magnitude higher. These two changes combined, allowed a direct comparison of the electric field calculated with the probe data and the reflectometry. This comparison was very favorable and showed clearly a complicated and not yet fully understood edge island structure, that is possibly linked to areas of long connection length located in the edge island. The comparisons also showed that the edge island could be observed with both diagnostics, with the limitation that slightly higher densities would strongly improve the resolution and accuracy of the reflectometry measurements.

The measurements showed that the higher performance and longer discharges allowed for a considerable evolution of the toroidal current, that could shift the plasma inwards or outwards (depending on the current direction and configuration) and modify the island size. This effect was observed with both the reflectometry and the combined probe. The higher perfomance also allowed first observations of high beta plasmas, that were shown to impact the edge profiles. A higher beta of more than 1% still needs to be regurlarly achieved with a diagnostic probe installed on the manipulator. It was also shown that the magnetic field structure, can largely supress the turbulences in the standard configuration close to the island remnant.

The comparison of the heat fluxes in the divertor configuration was not directly possible since the 5/5 island remnant is complicating the transport. This issue is further compounded by the fact that the divertor cameras had a low resolution, especially for the high iota configuration, where the island remnants are small and a lower impact of the islands would be expected.

The results from the EMC3-EIRENE modelling showed for the measurements in the divertor configuration again a good agreement. The modelling can also provide an estimate for the ion temperature profiles. The data of the ion sensitive probe is not usable, as testing was limited due to experimental constraints in the campaign plan. Recent results from RFA have supplied ion temperature profiles. There is also considerable room for improvement concerning the measurements in regard to the electron density profiles, since most diagnostic and modelling results on the ion species in the plasma and the effective charge is still pending, but the modelling can provide an estimate.

Furthermore the reported local peaking of the electron temperature was found regurlarly in the divertor standard configuration and also in the modified limiter configuration. It is also observed with reflectometry measurements and with the helium beam diagnostic. Therefore it is safe to assume that this is a real physics feature. The origin has not been fully explained, apart from it's emergence being associated with long connection length in the island remnant, that is present for the standard divertor and specific limiter configurations. A possible explanation for the peaking is the transport of impurities and radiative losses that differently cool the edge. Analysis will continue to explain this feature. The effects of the plasma currents also deserves a closer look, so far only a total toroidal current centered on the magnetic axis was used to model the current effect on the magnetic topology. This might, in first order be sufficient, but it will not fully reflect the reality of edge currents in the proximity of the island remnants.

The probe diagnostic itself will also see considerable change in the future since the feature of the ion temperature measurements and possibly a poloidal Langmuir probe array will greatly help analyzing features in the edge.

4.1 Appendix

4.2 Publications

The following publications have been made in the context of this thesis, as the first author:

P. Drews et al.,
Measurement of the plasma edge profiles using the combined probe on W7-X
Details of the contribution: Design of the combined probe together with the design department, planning of the experiments, analysis of the data, calculation of the connection length and field topology, interpretation and writing of the paper (90%), (2017) Nucl. Fusion 101605.R3

P. Drews et al.,
Magnetic configuration effects on the edge heat flux in the limiter plasma on W7-X measured using the infrared camera
Details of the contribution: Design of the combined probe together with the design department, planning of the experiments, analysis of the data from the combined probe, calculation of the connection length and field topology, mapping of the probe data on the limiters, interpretation and writing of the paper (70%), 2018 PST `https://doi.org/10.1088/2058-6272/aaa968`

P. Drews et al.,
Edge plasma measurements on the OP 1.2a divertor plasmas at W7-X using the upgraded combined probe
Details of the contribution: Upgrade of the combined probe, measurements in the Op 1.2a with the upgraded combined probe at W7-X, analysis of the data, comparison with reflectometry and modified connection length profile (65%), submitted 2018 to Nuc. Mat.

P. Drews et al.,
Operation of probe heads on the Multi-Purpose-Manipulator at W7-X in OP 1.2a
Details of the contribution: Design and co-design of the probe heads, operation of the probes, analysis of the data (80%), submitted 2018 to Fusion Engineering and Design

Publications as a co-author include:

M. Krychowiak et al.,
Overview of diagnostic performance and results for the first operation phase in Wendelstein 7-X
Details of the contribution: Analysis of the data from the combined probe, interpretation and comparison with other edge diagnostics like the limiter Langmuir probes, contribution to the manuscript detailing the measurements of the combined probe (10%), Review of scientific instruments **87** (2016) 11D304

J. Cosfeld et al.,
Effective charge state modelling for Wendelstein 7-X edge plasmas
Details of the contribution: Analysis of the probe data (15%), submitted Nucl. Fusion

Y. Liang et al.,
Diagnostic setup and modelling for investigation of synergy between 3D edge physics and plasma wall interactions on W7-X
Details of the contribution: Analysis of the probe data, contribution to the manuscript detailing the measurements of the combined probe and the Multi-Purpose-Manipulator (15%), Nucl. Fusion **57** (2017) 066049

D. Nicolai et al.,
A Multi-Purpose Manipulator system for W7-X as user facility for plasma edge investigation
Details of the contribution: Measuring and analyzing the movement profile of the multi-purpose manipulator, addition of the acceleration sensor (10%), Fusion Eng. Des. (2017), `http://dx.doi.org/10.1016/j.fusengdes.2017.03.013`

G. Satheeswaran et al.,
A PCS7 -based control and safety system for operation of the W7-X Multi-Purpose Manipulator facility
Details of the contribution: Measuring and analyzing the movement profile of the multi-purpose manipulator, contribution to writing and correction of the manuscript (10%), Fusion Eng. Des. (2017), `https://doi.org/10.1016/j.fusengdes.2017.05.125`

S. Liu et al.,
Observations of the effects of magnetic topology on the SOL characteristics of an electromagnetic coherent mode in the first experimental campaign of W7-X
Details of the contribution: Measurement of the edge profiles, analysis of the data, contribution to writing and correction of the manuscript (20%), Nucl. Fusion **58** (2018) 046002

T. Barbu et al.,
Radiative edge cooling experiments in Wendelstein 7-X startup limiter campaign
Details of the contribution: Measurements with combined probe in stationary position to observe the edge cooling, analysis and interpretation of the data (10%), submitted to Nucl. Fusion

A. Langenberg et al.,
Prospects of X-ray Imaging Spectrometers for Impurity Transport: Recent Results from the Stellarator Wendelstein 7-X
Details of the contribution: Preparation and operation of the manipulator (5%), Review of Scientific Instruments 89, 10G101 (2018); `https://doi.org/10.1063/1.5036536`

A. Krämer-Flecken et al.,
Investigation of turbulence rotation in limiter plasmas at W7-X with a new

installed Poloidal Correlation Reflectometry
Measurement with the combined probe, connection length calculation in the toroidal plane of the manipulator and the reflectometry (10%), Submitted to PPFC (2018)

C. Killer et al.,
Characterization of the W7-X Scrape-Off Layer using the Multi-Purpose Manipulator
Measurement with the combined probe, connection length calculation in the toroidal plane of the manipulator and the reflectometry (10%), IAEA Ahmedabad (2018) `https://conferences.iaea.org/indico/event/151/papers/6247/files/4612-iaea_proceeding_killer.pdf`

J. Cai et al.,
Measurements of the radial ion flow velocity profile using the multi-channel Mach probe in the boundary plasma of the W7-X stellarator
Co-design of the probe head, Preparation and conduction of experiments, (20%), submitted to Review of scientific instruments (2018)

sectionAdditional graphs

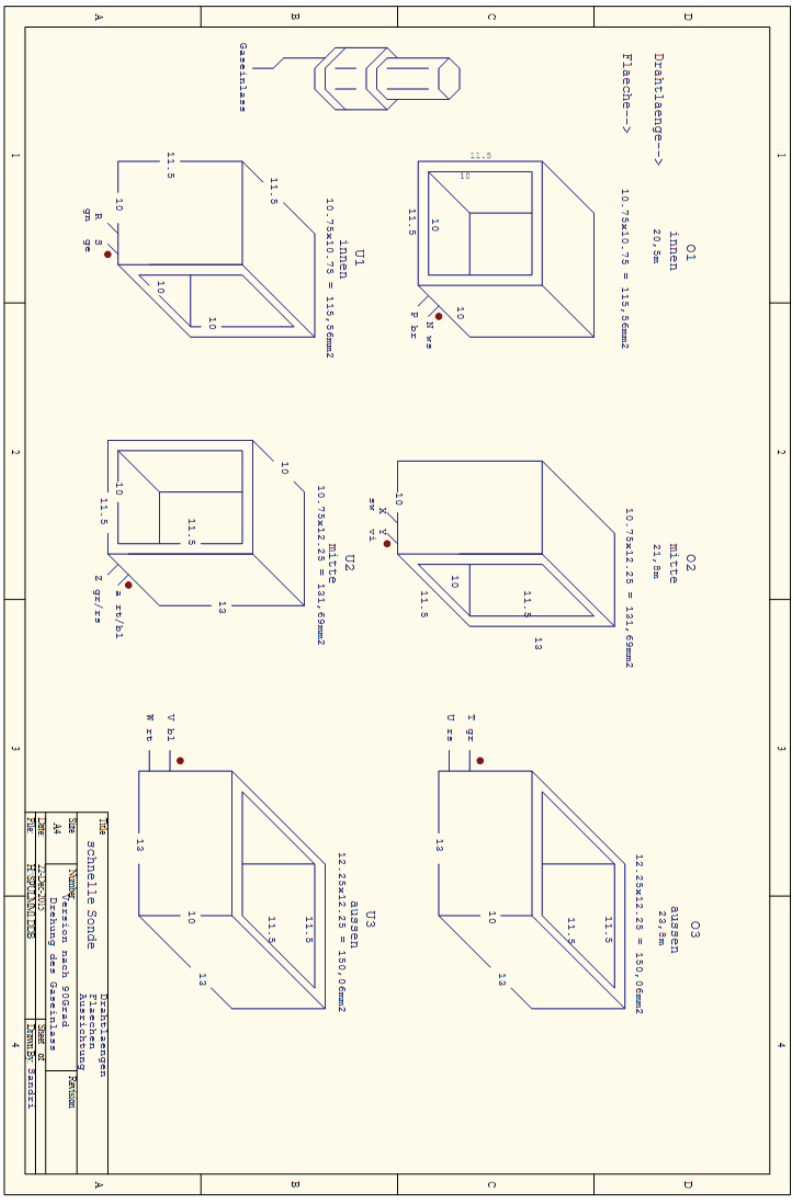

Figure 4.1: Coil configuration, with polarity, of the combined probe.

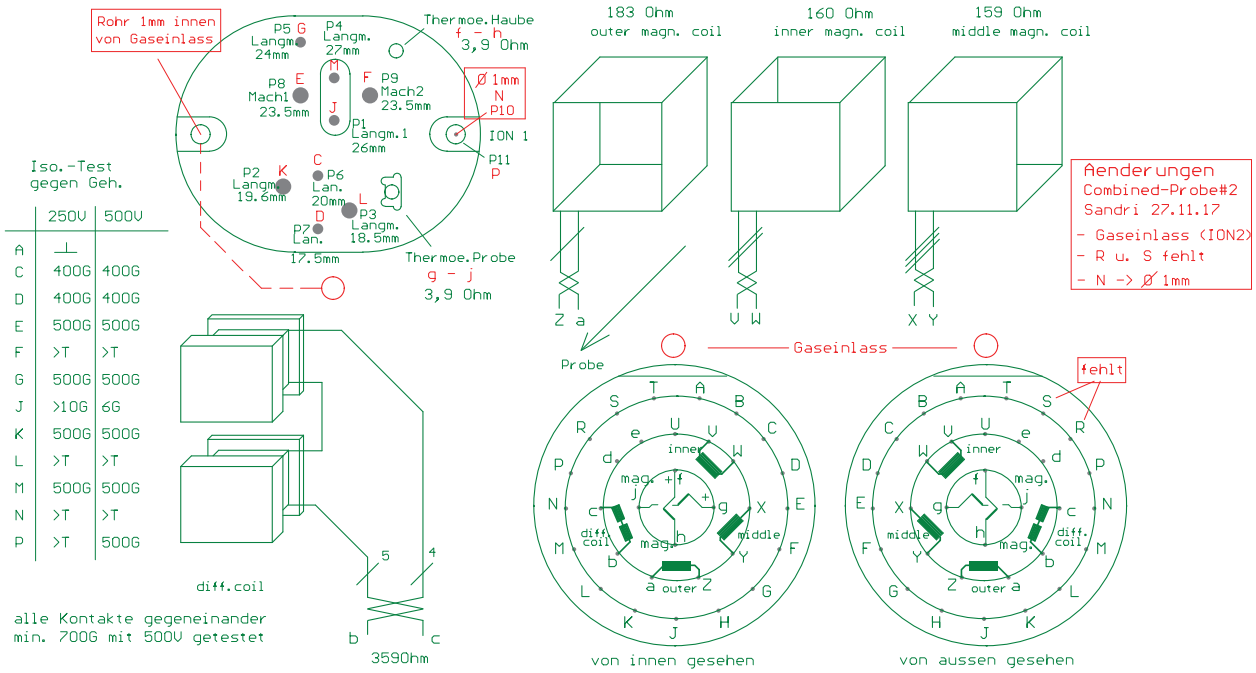

Figure 4.2: Plan and pin assignment for the upgraded combined probe, including the orientation of the pick-up coils.

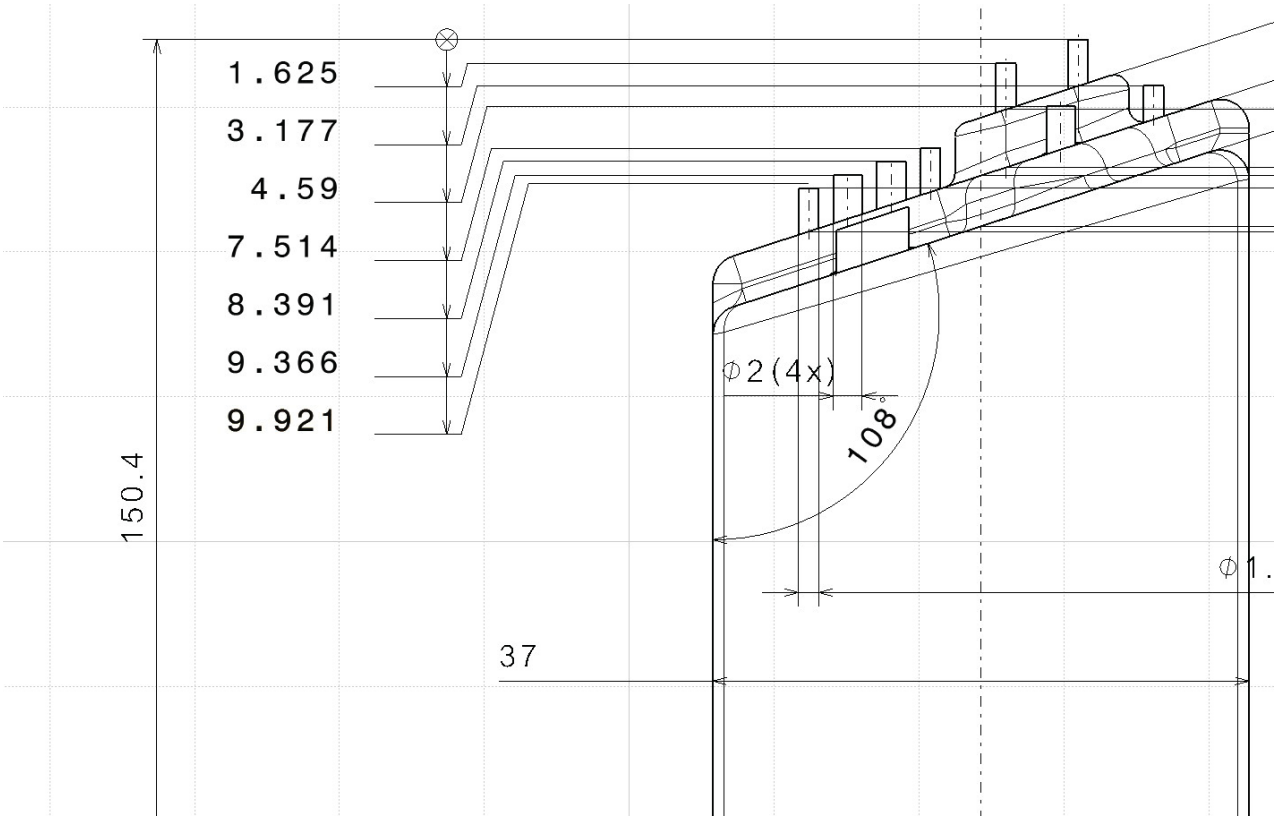

Figure 4.3: Position of the probe tips on the upgraded combined probe, with the angling of the probe cover.

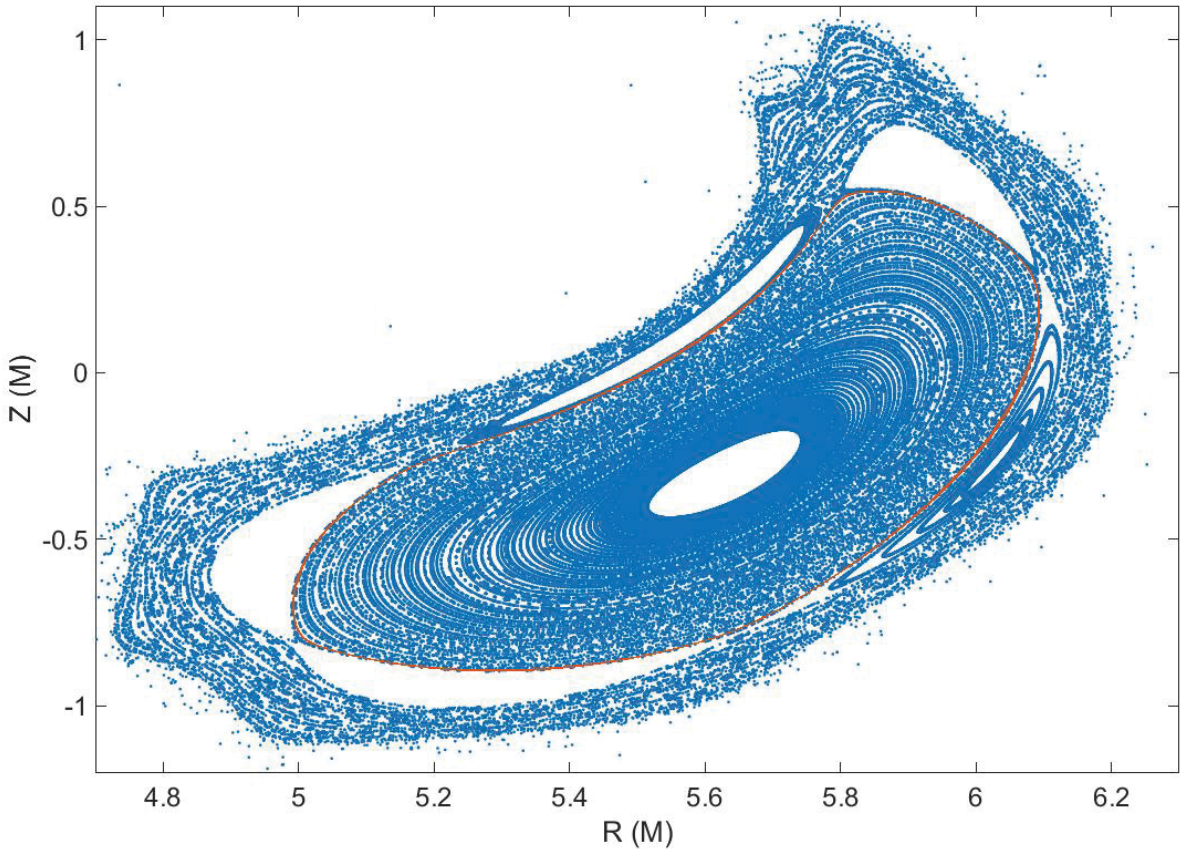

Figure 4.4: Poincaré plot at the crosssection of the MPM in the standard configuration.

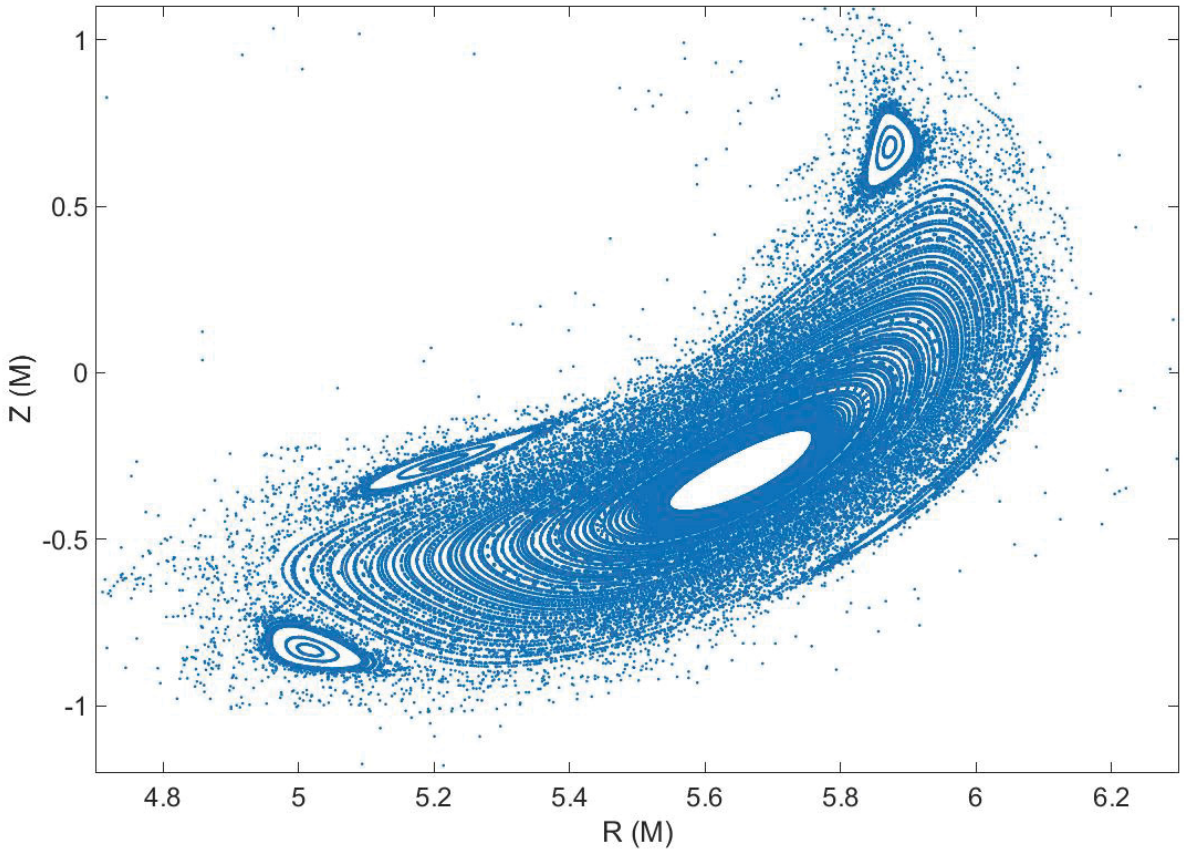

Figure 4.5: Poincaré plot at the cross section of the MPM in the high iota configuration.

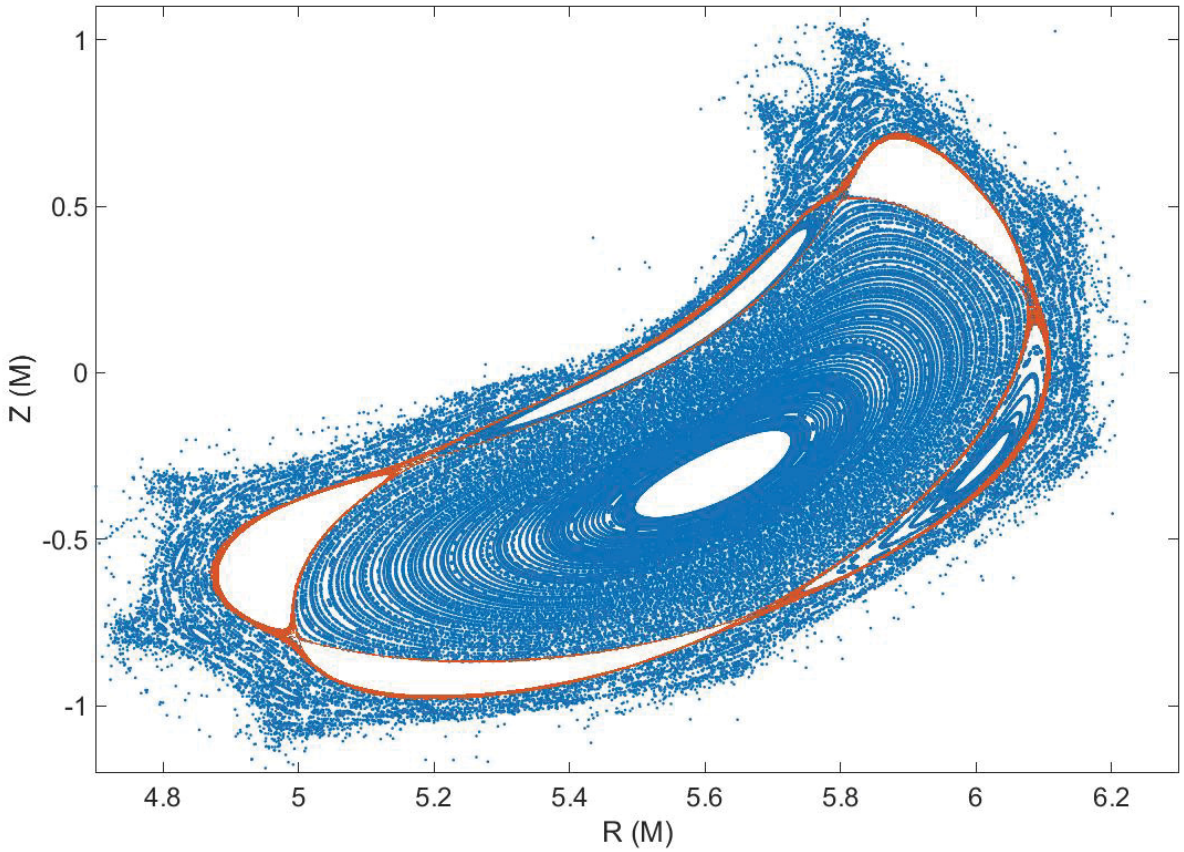

Figure 4.6: Poincaré plot at the cross section of the MPM in the reversed field configuration.

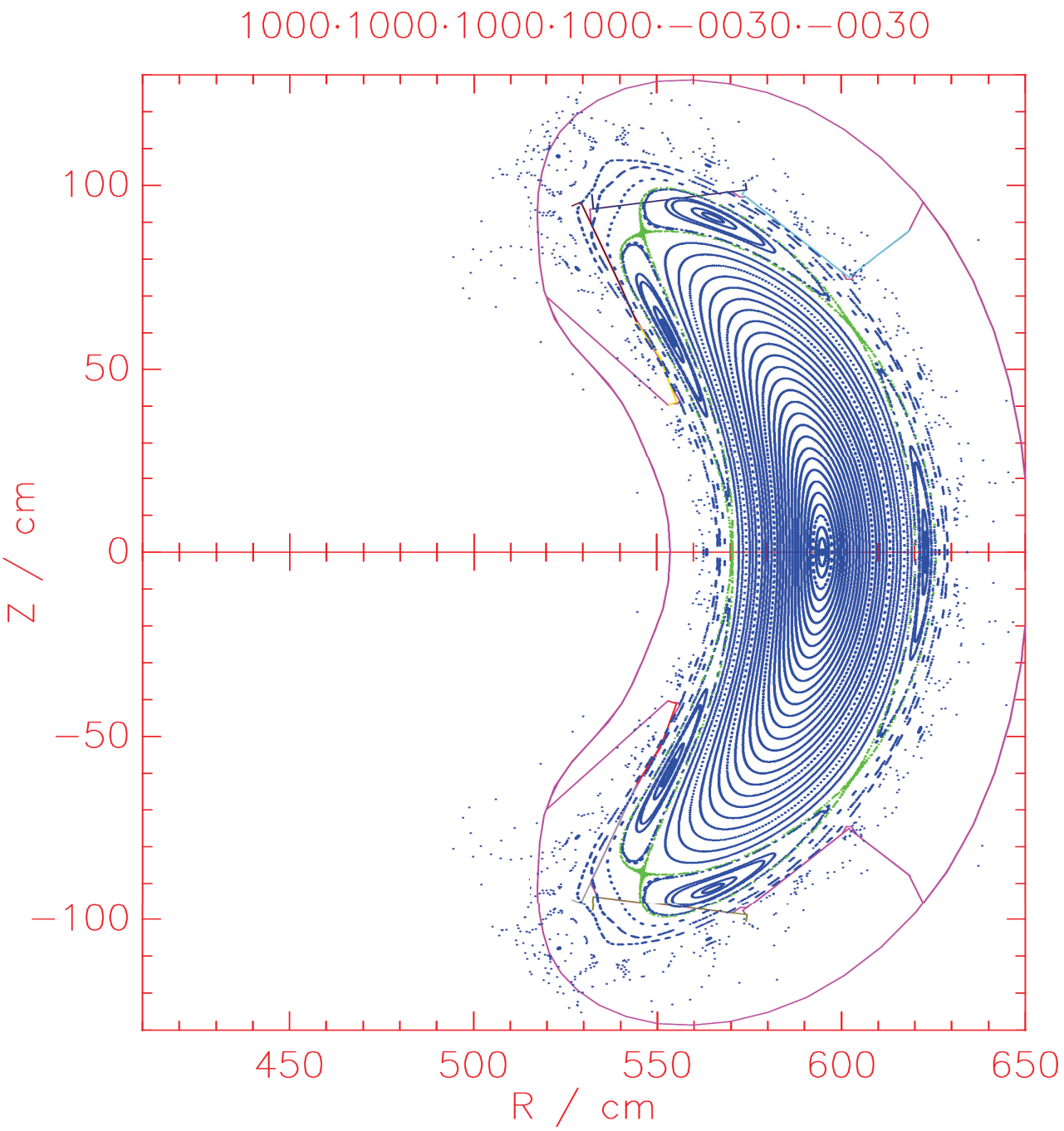

Figure 4.7: Poincaré plot at the cross section at $\phi = 0°$ in the standard field configuration with no toroidal current using VMEC.

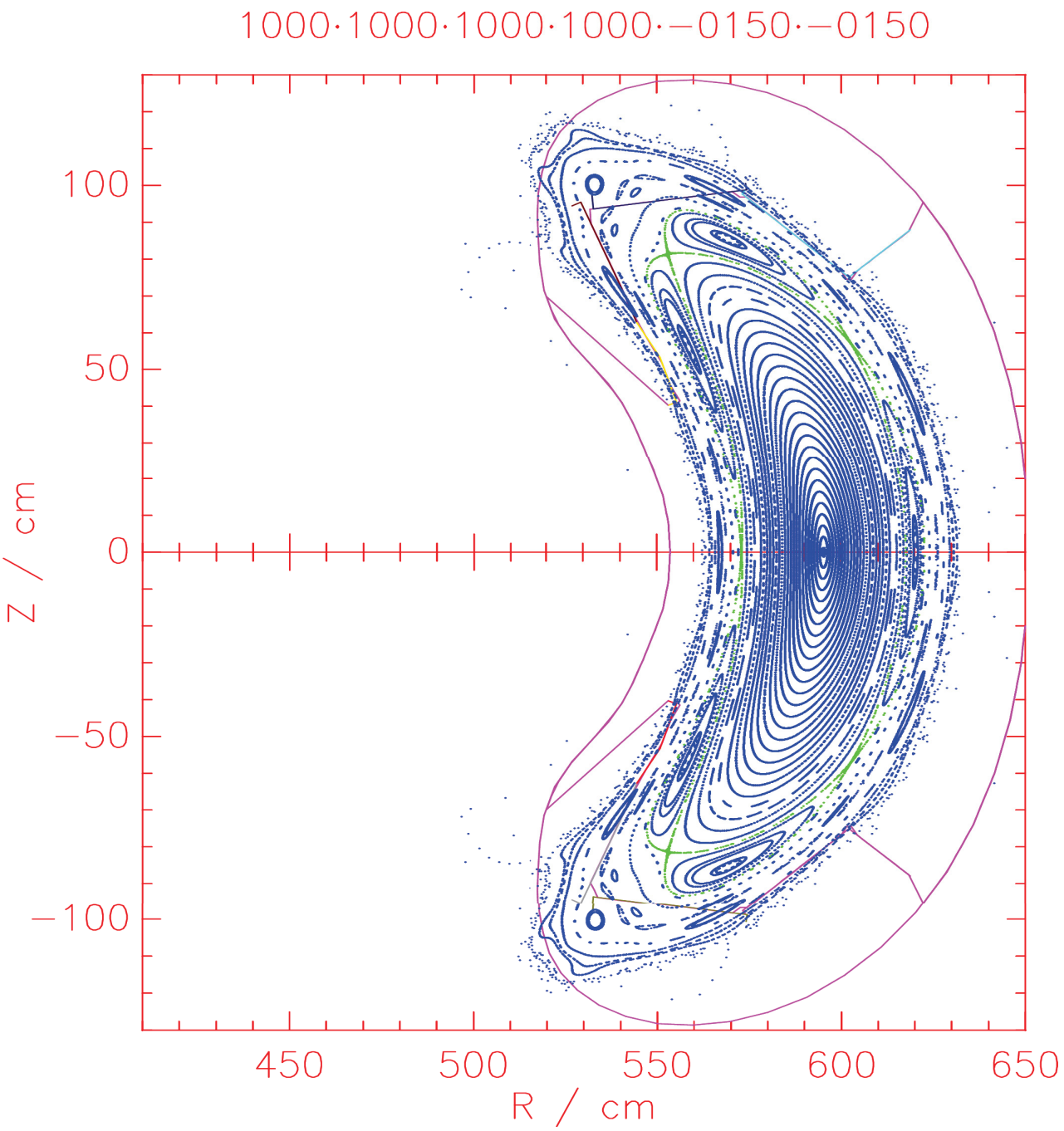

Figure 4.8: Poincaré plot at the cross section at $\phi = 0°$ in the standard field configuration with a higher iota simulating a toroidal current using VMEC.

Bibliography

[1] The theory of electrolytes. I. Lowering of freezing point and related phenomena, Physikalische Zeitschrift, Leipzip, 1923

[2] ENERGY, ELECTRICITY AND NUCLEAR POWER ESTIMATES FOR THE PERIOD UP TO 2050, INTERNATIONAL ATOMIC ENERGY AGENCY VIENNA, 2017

[3] L. Spitzer, The stellarator concept. Phys. Fluids **1**, 253–264, 1958

[4] K. Margaret Burbige et al., Synthesis of the elements in the Stars, Rev. of mod. Phys. **29**, 1957, http://adsabs.harvard.edu/abs/1920Obs....43..341E

[5] W. Nolting, Quantenmechanik-Grundlagen, Springer Verlag Berlin Heidelberg, 10.1007/978-3-540-68869-3, 2009

[6] U. Stroth, Plasmaphysik, Vieweg+Teubner Verlag, 10.1007/978-3-8348-8326-1, 2011

[7] A. G. Peters, The bootstrap current and its consequences, Plasma Phys. Control Fusion **43**, B231–B242, 2000

[8] P. Drewelow et al, Results of the first wendelstein 7-x island divertor experiments, submitted to Nuc. Mat, 2018

[9] R. J. Buttery et al, Neoclassical tearing modes, Plasma Phys. Control. Fusion, PII: S0741-3335(00)16997-0, 2000

[10] Y. Liang et al, Diagnostic setup and modelling for investigation of synergy between 3D edge physics and plasma wall interactions on W7-X, Nucl. Fusion **57**, 066049, 2017

[11] S. I. Braginskii. et al, ransport Processes in a Plasma, Reviews of Plasma Physics, 1:205, 1965

[12] D. Reiter et al, The EIRENE and B2-EIRENE Codes, Fusion Science and Technology, **47**,172–186, 2005

[13] Y. Feng et al, 3D Edge Modeling and Island Divertor Physics, Contrib. Plasma Phys **44**, DOI 10.1002/ctpp.200410009, 2004

[14] J. Cosfeld et al, 3D resolved effective charge state reconstruction with EMC3-EIRENE, submitted to Nucl. Fusion, 2018

[15] G. Grieger, Modular Stellarator reactors and plans for Wendelstein 7-X, Fusion Technology Volume 21, 1992 - Issue 3P2B: Proceedings of the Tenth Topical Meeting on The Technology Of Fusion Energy Boston, Massachusetts, June 7–12, 1992

[16] A. H. Boozer, Plasma equilibrium with rational magnetic surfaces. Phys. Fluids **24**, 1999–2003, 1981

[17] J. Nührenberg & R. Zille, Quasi-helically symmetric toroidal stellarators. Phys Lett A **129**, 113–117, 1988

[18] F. M. Canik et al. Experimental demonstration of improved neoclassical transport with quasihelical symmetry. Phys. Rev. Lett. **98**, 085002, 2007

[19] G. Satheeswaran et al, A PCS7 -based control and safety system for operation of the W7-X Multi-Purpose Manipulator facility, Fusion Eng. Des., 2017, https://doi.org/10.1016/j.fusengdes.2017.05.125

[20] D. Nicolai et al, A Multi-Purpose Manipulator system for W7-X as user facility for plasma edge investigation, Fusion Eng. Des., 2017, http://dx.doi.org/10.1016/j.fusengdes.2017.03.013

[21] M. Mitri, Real-time Digital Control of Plasma Position and Shape on the TEXTOR Tokamak, University Duisburg-Essen, May 2005

[22] M. Rack et al, A rotating directional probe for the measurements of fast ion losses and plasma rotation at Tokamak Experiment for Technology Oriented Research., Rev. Sci. Instrum. **84**, 083501, 2013

[23] M. Henkel et al, Multi-channel retarding field analyzer for EAST, 2018 Plasma Sci. Technol. **20**, 054001

[24] R. R. Weynants et al, S. Jachmich, and M. Van Schoor, Electrode biasing on TEXTOR: A tool for fundamental physics studies, Fusion sci. and tech. vol. **47**, 2005

[25] A. Cenk et al, A. M. Shkel, Experimental evaluation and comparative analysis of commercial variable-capacitance MEMS accelerometers, Journal of Micromechanics and Microengineering 2003

[26] Y. Yang et al, Experimental observations of plasma edge magnetic field response to resonant magnetic perturbation on the TEXTOR Tokamak, Nucl. Fusion **52**, 074014, 2012

[27] Tonks and Langmuir, A General Theory of the Plasma of an Arc, Phys Rev. **34**, 876-922, 1929

[28] Kyu-Sun Chung et al, Mach probes, Plasma Sources Sci. Technol. **21**, 063001, 2012

[29] C. Colin et all, Impact of a Langmuir Probe on Turbulence Measurements in the Scrape-Off-Layer of Tokamaks, Contrib. Plasma Phys. **54**, No. 4-6, 543 – 548, 2014, /10.1002/ctpp.201410087

[30] V. Erckmann et al, The 10 MW, CW ECRH System For W7-X: Status And First Integrated Tests, AIP Conference Proceedings 787, 371 (2005), https://doi.org/10.1063/1.2098260

[31] H. Greuner et al, Evaluation of vacuum plasma-sprayed boron carbide protection for the stainless steel first wall of Wendelstein 7-X, Journal of Nuclear Materials 329–333, 2004, 849–854

[32] P. Drews et al, Hodographs in the Analysis of Resonant Magnetic Perturbations, Rheinischen Friedrich-Wilhelms-Universität Bonn, February 2015

[33] A. Knieps et al, Investigations of the outer magnetic field of Wendelstein 7-X using the magnetic probe, 45th EPS, Prague, Czech Republic, 2018

[34] S. Chen and T. Sekiguchi, Instantaneous Direct Display System of Plasma Parameters by Means of Triple Probe J. Appl. Phys. **36**, 2363, 1965

[35] Kamitsuma et al, The theory of the instantenous triple-probe method for direct display of plasma parameters in low density collisionless plasmas J. Phys. D: Appl. Phys. **10**, 1977

[36] M. Krychowiak et al, Overview of diagnostic performance and results for the first operation phase in Wendelstein 7-X, Rev. Sci. Instrum. **87**, 11D304, 2016

[37] T. Barbui, Radiative edge cooling experiments in Wendelstein 7-X startup limiter campaign, submitted to Nucl. Fusion, 2018

[38] S. Chen et al, Studies of the Effect on Ion Current on Instantaneous Triple-Probe Measurements, J. Appl. Phys. **42**, 1971

[39] A. Kräemer-Flecken et al, Investigation of turbulence rotation in limiter plasmas at W7-X with a new installed Poloidal Correlation Recflectrometry, Nucl. Fusion **57** 066023, 2017

[40] S. P. Hirschman et al, Three-dimensional free boundary calculations using a spectral Green's function method, Computer Physics Communications **43**, 143—155, 1986

[41] B. Kardon, Measurement of Plasma Flows Using Mach ProbeArray , Department of Physics, MIT, 2008 `https://dspace.mit.edu/bitstream/handle/1721.1/54615/600142320-MIT.pdf?sequence=2`

[42] W. M. Stacey et al, Fusion plasma physics, Wiley-VCH, 10.1002/9783527618736, 2008

[43] I. Katsumata et al, Ion Sensitive Probe-A New Diagnostic Method for Plasma in Magnetic Fields, Japan J. Appl. Phys. **6**, 1967

[44] P. Ström et al, A combined segmented anode gas ionization chamber and time-of-flight detector for heavy ion elastic recoil detection analysis, Rev. Sci. Instrum. **87**, 103303, 2016, http://dx.doi.org/10.1063/1.4963709

[45] D. Brunner et al, Space-charge limits of ion sensitive probes, Plasma Physics and Controlled Fusio, **55**, 125004, 2013

[46] S. Bozhenkov et al., Service oriented architecture for scientific analysis at W7-X. An example of a field line tracer, Fusion Engineering and Design **88**, 2997– 3006, 2013

[47] Y. Gao et al, The simulation of thermal response on probe for W7-X, internal presentation

[48] A. Dinklage et al, Confinement in Wendelstein 7-X Limiter Plasmas, Proceedings of the 43nd EPS, Leuven, Belgium, 2016

[49] T. Klinger et al, Performance and properties of the first plasmas of Wendelstein 7-X, Plasma Phys. Control. Fusion **59**, 014018, 2017

[50] P. Drews, Measurement of the plasma edge profiles using the combined probe on W7-X, 2017 Nucl. Fusion **57**, 126020, 2017

[51] P. Drews et al, Magnetic configuration effects on the edge heat flux in the limiter plasma on W7-X measured using the infrared camera and the combined probe, PST **20**, 2018, https://doi.org/10.1088/2058-6272/aaa968

[52] L. Stephey et al, Spectroscopic imaging of limiter heat and particle fluxes and the resulting impurity sources during Wendelstein 7-X startup plasmas , Submitted to Rev. Sci. Instrum., 2016

[53] W.B. Thompson et al, Harrison-Thompson Generalization of Bohm's Sheath Condition Proc. Phys. Soc. **74** 145., 1959

[54] M. Jakubowski et al, Scrape-off layer physics in the initial campaign of Wendelstein 7-X, EPS Belfast 2017 I2.106

[55] A.R. Akerson et al, Three-dimensional scrape off layer transport in the helically symmetric experiment HSX, Plasma Phys. Control. Fusion **58**, 084002, 2016

[56] N. Ohyabu et al, Edge Thermal Transport Barrier In LHD Discharges, Phys. Rev. Lett. **84**, 103, 2000

[57] T. Eich et al, Inter-ELM Power Decay Length for JET and ASDEX Upgrade: Measurement and Comparison with Heuristic Drift-Based Model PRL. **107**, 215001, 2011

[58] H. J. Sun et al, Study of near scrape-off layer (SOL) temperature and density gradient lengths with Thomson scattering, Plasma Phys. Control. Fusion **57**125011, 2015

[59] A. Kallenbach et al, Multi-machine comparisons of H-mode separatrix densities and edge profile behaviour in the ITPA SOL and Divertor Physics Topical Group, Journal of Nuclear Materials 337-339, 381-385, 2005

[60] S. Bozenkov et al, Limiter for the early operation phase of W7-X, Proceedings of the 41nd EPS, 2014

[61] F. Gadelmeier et al, Conditions for island divertor operation in the W7-AS Stellarator, Proceedings of the 28nd EPS, 2001

[62] S. Masuzaki et al, The divertor plasma characteristics in the Large Helical Device, Nucl. Fusion **42**, 750–758, 2002

[63] G. A. Wurden et al, Limiter observations during W7-X first plasmas, Nucl. Fusion **57**, 056036, 2017

[64] S. Bozhenkov et al, The Thomson scattering diagnostic at Wendelstein 7-X and its performance in the first operation phase, 2017 accepted Nucl. Fusion

[65] H. Niemann et al, Power loads in the limiter phase of Wendelstein 7-X, Proceedings of the 43nd EPS, 2016, (http://ocs.ciemat.es/EPS2016PAP/pdf/P4.005.pdf)

[66] M. Rack et al, A fluid–kinetic approach for 3D plasma edge transport in He-plasma, Nucl. Fusion **57**, 056011, 2017

[67] F. Effenberg et al, Numerical investigation of plasma edge transport and limiter heat fluxes in Wendelstein 7-X startup plasmas with EMC3-EIRENE, 2017 Nucl. Fusion **57** 036021

[68] A. Hermann et al, Limitations for divertor heat flux calculations of fast events in tokamaks, EPS Vol **25A**, 2001, http://www.cfn.ist.utl.pt/EPS2001/CD/pdfs/P5.104.pdf

[69] P. Drews et al, Edge plasma measurements on the OP 1.2a divertor plasmas at W7-X using the upgraded combined probe, submitted to Nuc Mat, 2018

[70] S. Liu et al, Observations of the effects of magnetic topology on the SOL characteristics of an electromagnetic coherent mode in the first experimental campaign of W7-X
Nucl. Fusion **58**, 046002, 2018

[71] A. Krämer-Flecken et al, Investigation of turbulence rotation and radial electric field in the island divertor and plasma edge at W7-x, 19th International 195th Congress on Plasma Physics (ICPP), Vancouver, Canada, 2018

[72] Y. Gao et al, Effects of toroidal plasma currents on the strike-line movements on w7-x, talk 45th EPS, Prague, Czech Republic, 2018

[73] Y. Suzuki and J. Geiger, Impact of nonlinear 3d equilibrium response on edge topology and divertor heat load in wendelstein 7-X, Nuclear Fusion **58**, 2016, doi:http://dx.doi.org/10.1088/0741-3335/58/6/064004

[74] K. J. Brunner, Real-Time Dispersion Interferometry for Density Feedback in Fusion Devices, submitted to JINST, 2018, JINST 060P 0518

[75] S. Schmuck, Design of the ECE diagnostic at Wendelstein 7-X,Fusion Engineering and Design, 84, 2009,1739–1743, https://ac.els-cdn.com/S0920379608005024/dx.doi.org/10.1016/j.fusengdes.2008.12.094

[76] K. Rahbarnia et al, Diamagnetic energy measurement during the first operational phase at the Wendelstein 7-X stellarator, Nuclear Fusion 58 096010, 2018, https://doi.org/10.1088/1741-4326/aacab0

[77] H. Niemann et al, Power loads in the divertor phase of wendelstein 7-X, submitted to Nuc. Mat, 2018

[78] S. Marsen et al, Divertor Heat Load in JET - Comparing Langmuir Probe and IR Data, Proceedings of the 40nd EPS, Otaniemi, Finland, 2013 http://ocs.ciemat.es/EPS2013PAP/pdf/P1.127.pdf

List of Figures

List of Tables

Erklärung zur Dissertation

Ich versichere an Eides Statt, dass die Dissertation von mir selbständig und ohne unzulässige fremde Hilfe unter Beachtung der „Grundsätze zur Sicherung guter wissenschaftlicher Praxis an der Heinrich-Heine-Universität Düsseldorf“ erstellt worden ist.
Die Dissertation wurde in der vorgelegten oder in ähnlicher Form noch bei keiner anderen Institution eingereicht. Ich habe bisher keine erfolglosen Promotions- versuche unternommen.

Jülich den,

Philipp Drews